Quasi-Phase-Matching of High-Harmonic Generation

Thomas A. Robinson

Keble College, Oxford

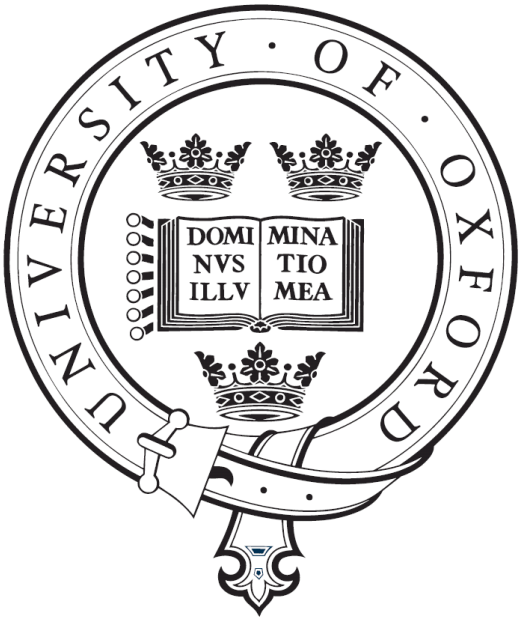

Submitted for the degree of Doctor of Philosophy

Trinity Term 2009

Supervised by

Professor Simon M. Hooker

Clarendon Laboratory

University of Oxford

United Kingdom

Quasi-Phase-Matching of High-Harmonic Generation

Thomas A. Robinson

Keble College, Oxford

Submitted for the degree of Doctor of Philosophy

Trinity Term 2009

Abstract

This thesis describes the use of counterpropagating pulse trains to quasi-phase-match high-harmonic generation (HHG).

Two novel techniques for generating trains of ultrafast pulses are described and demonstrated. The first method makes use of a birefringent crystal array to split a single pulse into a sequence of pulses. The second method makes use of the time-varying polarisation of a chirped pulse passed through a multiple-order wave plate to generate a train of pulses by the addition of a polariser. It is demonstrated that this second technique can be used to make pulse trains with non-uniform pulse separation by using an acousto-optic programmable dispersive filter to manipulate the higher-order dispersion encountered by the chirped pulse.

The crystal array method is used to demonstrate quasi-phase-matching of HHG in a gas-filled capillary, using one and two counterpropagating pulses. Enhancements of up to 60% of the intensity of the 27th harmonic of the 800 nm driving laser light are observed. Information on the spatial and dynamic properties of the HHG process is obtained from measurements of the coherence length in the capillary.

Simulations of HHG in a capillary waveguide have been performed. These agree well with the results of the quasi-phase-matching experiments. The effect of mode-beating on the generation process in a capillary and its use as a quasi-phase-matching mechanism are investigated.

Acknowledgements

This thesis would not exist, were it not for the invaluable help and guidance I have received over the past four years from Simon and Kevin.

Simon, thank you for your advice, insight and boundless optimism and enthusiasm, however things were going in the lab. I am lucky to have had you as a supervisor.

Kevin, thank you for showing me the ropes and for being a constant source of wisdom and encouragement.

Charlotte, it's been great to do my D.Phil alongside you and to be able to share our frustrations, problems and successes over endless cups of tea. Thank you for all your help. Thanks also to everyone else in the Hooker group: Matt, Claire, Tony, Tom R-R, Tom I, Nicolas, Svet, Andi and Luis, for your advice and assistance around the lab and for your company in the tea-room.

Just as important has been the support of my friends in Oxford, both in Keble MCR and my housemates in York Place and Walton Street. Particular thanks to Bob, Rich, Inga, James, Hugo, Kenny, Sarah, Yukie, Abi, Maria, Pete, Rick, Prince, Ross, MaryAnn, Ouldo, Kashmali, Sarah, Jon and Adam. You have made the past four years a very happy time for me.

T.R.
Oxford, March 2010

For my parents

Author's Publications

Journal Publications

1. B. Dromey, M. Zepf, M. Landreman, K. O'Keeffe, T. Robinson, and S. M. Hooker, **"Generation of a train of ultrashort pulses from a compact birefringent crystal array,"** *Applied Optics* 46, 5142-5146 (2007)

2. M. Landreman, K. O'Keeffe, T. Robinson, M. Zepf, B. Dromey, and S. M. Hooker, **"Comparison of parallel and perpendicular polarized counterpropagating light for suppressing high harmonic generation,"** *Journal of the Optical Society of America B* 24, 2421-2427 (2007)

3. T. Robinson, K. O'Keeffe, M. Landreman, S. M. Hooker, M. Zepf, and B. Dromey, **"Simple technique for generating trains of ultrashort pulses,"** *Optics Letters* 32, 2203-2205 (2007)

4. K. O'Keeffe, T. Robinson and S. M. Hooker, **"Generation and control of chirped, ultrafast pulse trains,"** *Journal of Optics* 12, 015201 (2010)

5. T. Robinson, K. O'Keeffe, B. Dromey, M. Zepf and S. M. Hooker, **"Generation and control of ultrafast pulse trains for quasi-phase-matching high-harmonic generation,"** *Journal of the Optical Society of America B* (Accepted)

Conferences

1. T. Robinson, K. O'Keeffe, M. Landreman, B. Dromey, M. Zepf and S. M. Hooker, **"Comparison of parallel and perpendicular polarized counterpropagating light for quasi-phase-matching high harmonic generation,"** *Ultrafast Phenomena*, June 2008

2. T. Robinson, K. O'Keeffe, and S. M. Hooker, **"Chirped Pulse Trains for Quasi-Phase-Matching High Harmonic Generation,"** *Nonlinear Optics*, July 2009

Contents

List of Figures

Chapter 1

Introduction

The development of the laser is one of the greatest technological achievements of the twentieth century. Since the first demonstration[1] of a ruby laser by Theodore Maiman in 1960, they have revolutionised both scientific research and aspects of our everyday lives. From laser surgery to spectroscopy, optical communications to laser cooling, lasers have played an integral role in scientific and technological progress over the past fifty years.

Laser sources are now available over a wide spectral range, however sources in the extreme ultraviolet (XUV, 120–10 nm) and soft x-ray (SXR, 10–0.1 nm) spectral regions have remained elusive. It is difficult to obtain lasing at frequencies above the near-ultraviolet, due to the well-known λ^{-4}[2] scaling of pump power with wavelength: for XUV lasers, pump powers in excess of $100\,\mathrm{MWcm^{-3}}$ are typically required to generate a threshold population inversion, which traditional pump mechanisms such as flashlamps and electrical discharges cannot supply[3]. It is also difficult to find materials which are suitable for cavity mirrors in this spectral region, so single-pass geometries are typically used. Progress has been made with lasing schemes based on collisional[4] and recombination[5] excitation as well as those driven by photoionisation pumping[6] and electrical discharges[7].

To date, collisional excitation schemes are the most robust approach for generating strongly amplified soft x-ray radiation[8]. The gain medium is a plasma column ablated from a slab target by a high-power laser pulse. Such a scheme, based on the 21 nm transition in Ne-like Zn has produced the most powerful XUV laser to date, with a peak intensity of $5 \times 10^{11}\,\mathrm{Wcm^{-2}}$[9]. However, the laser pump energy required ($\approx 500\,\mathrm{J}$) and the resulting low repetition rate makes it impractical. Efforts have been made to reduce the necessary pump energy, such as the use of a grazing-incidence pumping (GRIP) scheme to achieve lasing in Ni-like palladium with pump energies as low as 500 mJ[10]. However, no scheme has been engineered to the point of being commercially available and the narrow bandwidth and long pulse duration of x-ray lasers limit their applications.

A compact, affordable source of spectrally-bright, ultrashort and coherent XUV/SXR light would have widespread and important applications. Governments are investing billions of dollars in large-scale facilities such as synchrotrons and free-electron lasers, reflecting the demand within the scientific community for these sources.

1.1 XUV/SXR Light Sources

The spectral brightness of a radiation source is defined as:

$$B = \frac{N}{\tau \theta A \sigma} \tag{1.1}$$

where N is the number of photons per pulse, τ is the pulse duration, A is the cross-sectional area of the source, θ is the solid angle of emission and σ is the bandwidth. The spectral brightness is usually quoted in units of photons $\mathrm{s^{-1}}$ $\mathrm{mrad^{-2}}$ $\mathrm{mm^{-2}}$ per 0.1% bandwidth. The various XUV/SXR sources currently available are briefly outlined in this section. Figure 1.1

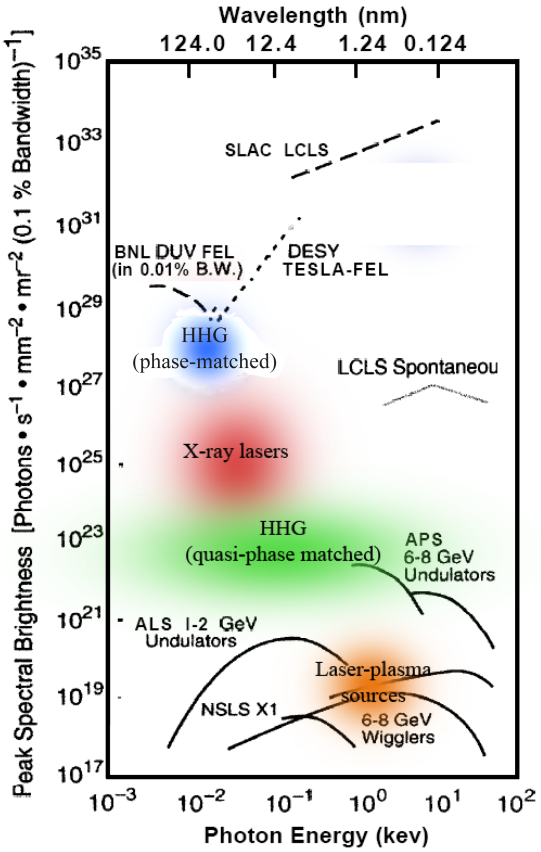

Figure 1.1: Approximate spectral brightness of existing and planned XUV/SXR sources as a function of photon energy (wavelength). Figure adapted from [11].

indicates the spectral brightness as a function of photon energy for these sources.

1.1.1 Synchrotrons

Synchrotrons are cyclic particle accelerators where magnetic and electric fields are synchronised to guide and accelerate a particle bunch respectively. The energy radiated by the accelerated particles was originally considered a nuisance in a particle physics context, but synchrotrons are now built specifically as radiation sources. Synchrotrons typically accelerate electrons to GeV energies, producing synchrotron radiation in the x-ray spectral region

with very high brightness ($> 10^{19}$ photons s^{-1} $mrad^{-2}$ mm^{-2} per 0.1% bandwidth).

In the latest generation of synchrotrons the electrons are accelerated to their maximum energy before being injected into a larger storage ring where they circulate, grouped in bunches, in a high vacuum for several hours with a relatively constant energy. Insertion devices called "wigglers" and "undulators" can be set up in straight sections of the storage ring, consisting of periodic structures of dipole magnets, to give a spatially alternating, static magnetic field. Electrons traversing the periodic magnet structure are forced to undergo oscillations and radiate: large oscillations are termed "wiggles" and smaller oscillations are known as "undulations".

Synchrotrons are high-brightness, collimated sources in the x-ray spectral region, but they are very expensive and experiments making use of them must be conducted at huge user facilities. Large-scale synchrotrons typically cost several hundred million US dollars to build; as a consequence only a small number of these facilities have been constructed and their beam-time is strictly rationed.

1.1.2 X-Ray Free-Electron Lasers

Free-electron lasers (FELs) also make use of synchrotron radiation, but have a brightness that can be up to one billion times higher than that of ordinary synchrotron light. An FEL consists of a linear accelerator followed by an undulator. The electrons in a synchrotron undulator are uniformly distributed longitudinally and radiate independently, leading to partial cancelation of emission. However in an FEL, interaction between the electrons and the radiation they have emitted causes the electrons to form "microbunches" which are separated by the wavelength of the emitted radiation. This means that they radiate approximately in-phase, leading to intense, coherent light comparable to that produced in conventional lasers.

Also, since the microbunches are so small, the pulses of radiation are correspondingly short, with durations on the order of 200 fs. The wavelength of the light emitted can be tuned by adjusting the energy of the electron beam or the magnetic field strength of the undulators.

Just as for conventional x-ray lasers, the lack of suitable cavity mirrors means that x-ray FELs employ a single-pass geometry, typically consisting of 1000 undulator periods. The first x-ray FEL was the FLASH facility at DESY in Hamburg. Electrons with 1 GeV energy from a linear accelerator are passed through a 30 m-long undulator to produce pulses of x-rays with wavelengths of approximately 6.5 nm. More recently, the Linac Coherent Light Source at Stanford has achieved emission further towards the hard x-ray region, at 0.15 nm.

Despite their high brightness, one drawback of FELs is the lack of temporal coherence, due to a noisy startup process. Techniques are being developed to overcome this by "seeding" the FEL with another x-ray source tuned to the resonant frequency of the undulator. However, as with synchrotrons, the major drawback is the cost and size of these facilities. There are currently only a handful of x-ray FELs planned or operational, each costing over a billion US dollars to build.

1.1.3 Laser-Produced Plasma Sources

A relatively simple technique for generating light in the hard- x-ray region is to focus a high-power laser into a solid target consisting of a high-Z material[12]. These compact, laser-driven plasma sources are an attractive alternative to accelerator-based radiation generation.

When a sub-100 fs laser pulse having a peak intensity of 10^{15}-10^{16} Wcm^{-2} is focussed onto a metal target, the atoms on the surface are ionized to produce a thin layer of plasma. Electrons may be accelerated away from the surface and then back into it, with a net gain of energy. These hot electrons, with average kinetic energies of several tens of keV, penetrate

into the target, exciting K-shell electrons from atoms in the bulk of the metal via inelastic collisions. The K-shell holes are filled by recombination of electrons from higher shells, leading to emission of the characteristic X-ray fluorescence lines. The X-ray burst that is generated in this way is short because electrons are accelerated only in the presence of the driving femtosecond laser pulse. In addition, the hot electrons emit a continuous background of Bremsstrahlung radiation. Unfortunately the x-ray radiation produced is not collimated, but is emitted in all directions and is incoherent.

1.1.4 High-Harmonic Generation

High-harmonic generation (HHG) is a means of producing bright, *coherent*, ultrafast pulses of XUV and soft x-ray radiation and is the source investigated in this thesis. The basic experimental arrangement for HHG is straightforward: an ultrashort, linearly-polarized laser pulse is focused to a peak intensity of order $10^{14}\,\mathrm{Wcm}^{-2}$ or greater into a gas, generating coherent beams of radiation with frequencies $\omega_q = q\omega_0$ where ω_0 is the frequency of the incident radiation and q is an odd integer. HHG is already used in many laboratories since it represents a relatively compact, affordable, coherent XUV source. However, as with any harmonic generation process, a significant drawback with HHG is that it is inefficient, due to phase-mismatch caused by the different phase velocities of the fundamental and harmonic radiation. Without implementing additional techniques, the conversion efficiency for generating photons with energies up to about 100 eV is of order 10^{-7}, and this decreases to as little as 10^{-15} for harmonic photon energies near 1 keV. Phase-matching techniques can increase the generation efficiency by two orders of magnitude for photon energies up to approximately 100 eV. Further techniques, such as those described in this thesis are required to increase generation efficiencies further.

1.2 Applications of High-Harmonic Light

One of the most pursued applications of HHG is the generation of attosecond (10^{-18} s) duration pulses. These pulses can be used to probe processes such as atomic electron dynamics, which occur on this time-scale. Farkas and Toth first proposed that the broad spectral range of the generated harmonics could be used to generate trains of attosecond pulses, as long as there was a fixed phase relationship between the harmonics[13]. In 2001, Paul et al. demonstrated phase locking between five consecutive harmonics from argon[14], producing a train of pulses of duration 250 as. Hentschel et al. also demonstrated that single isolated attosecond pulses could be produced by spectrally filtering the continuous cutoff region of the spectrum, generated using few-cycle laser pulses[15]. These attosecond pulses have been used to achieve time-resolved measurements of electron dynamics[16, 17, 18].

High harmonic light can also be used for imaging. The smallest structure size, δ that can be resolved by an optical system is given by $\delta = \kappa\lambda/NA$, where λ is the wavelength of the light source, NA is the numerical aperture of the optical system and κ is a numerical constant of order unity which depends on the degree of spatial coherence of the illumination of the object plane. The short wavelengths and high spatial coherence[19] which can be achieved with HHG therefore make it a good candidate for nm-resolution microscopy. Of particular importance in biological and materials imaging is the spectrum between the carbon K-absorption edge at 284 eV (4.4 nm) and the oxygen K-absorption edge at 539 eV (2.3 nm). In this energy range, water is transparent, whereas carbon and heavier elements in proteins and other molecules of living matter are absorbing. Biological samples can therefore be imaged in their *in vivo*, wet state and natural contrast is present between the water background and the biological structures within the cells.

Imaging with HHG light can be performed using multilayer mirrors and Fresnel zone plates[20], or with diffractive imaging[21], eliminating the need for imaging elements in the optical system. In the case of diffractive imaging, the diffraction pattern from the illuminated object is recorded and then a computerized phase retrieval algorithm is used to reconstruct an image of the object.

XUV radiation from HHG has also been used in ultrafast pump-probe investigations of molecular dynamics[22, 23] as well as static molecular structure[24]. Ultrafast holography with HHG light has been performed to study the femtosecond dynamics of the deformations of a surface[25].

1.3 Scope of this Thesis

This thesis describes the investigation of quasi-phase-matching techniques to enhance the efficiency of high-harmonic generation. In the next chapter, the theoretical background to high-harmonic generation is explored and simulations of the single-atom process are presented. In Chapter 2, the principles of phase and quasi-phase-matching of HHG are introduced and previous experiments using these techniques are discussed. In the experiments presented in this thesis, HHG is performed by guiding laser pulses through a gas-filled capillary, so in Chapter 4 the principles of grazing-incidence guiding in waveguides are described and simulations are performed to investigate the effect of mode beating on the generation process. The quasi-phase-matching scheme studied here makes use of counterpropagating trains of ultrafast pulses, so in Chapter 5 the theoretical basis and experimental demonstration of two novel techniques for generating pulse trains are presented. In Chapter 6 experiments are described which illustrate quasi-phase-matching of HHG using these trains

of pulses. Finally, a summary and discussion of future research possibilities are given in Chapter 7.

1.4 Role of the Author

The pulse train measurements presented in Chapter 5 were undertaken by the author with the help of Dr. Kevin O'Keeffe. The experiments were designed and built by the author and the control software was adapted from that written by Matt Landreman, a former student in the research group.

The experiments described in Chapter 6 were adapted from the designs of those performed by Matt Landreman. Construction and redesign of the experiment was performed by the author and Kevin O'Keeffe. The software used to run the experiment was written by the author. The data presented here was obtained and analysed by the author.

Other activities of the author included the design and machining of a new glass-capillary mounting setup and the development of new techniques for machining gas slots in glass capillaries.

All simulations presented in this thesis are the work of the author.

Chapter 2

High-Harmonic Generation

When an intense, ultrafast linearly-polarized laser pulse is focused into a gas or other matter, light at high harmonics of the fundamental field frequency $\omega_q = q\omega$ (q, an integer) are emitted, due to the highly non-linear response of an atom to a strong driving field. This process is known as high-harmonic generation (HHG).

HHG spectra have a distinctive shape, as shown schematically in Figure 2.1. For low q there is a sharp decline in harmonic output as a function of q, followed by a plateau region where there is little variation in harmonic intensity with order, followed by an abrupt cutoff. The first experimental observation of this plateau of harmonic frequencies was made in 1987 by McPherson et al.[26], who observed harmonics up to $q = 17$ of a 248 nm laser pulse in a neon gas jet. Much work was then concentrated on extending the cutoff frequency using shorter, more intense laser pulses. A theoretical understanding of the process was not developed until Corkum's "simple man's theory"[27] in 1993, which used a combination of quantum and classical mechanics to successfully explain the process and the observed cutoff frequencies. Shortly afterwards a semiclassical theory making use of the strong-field

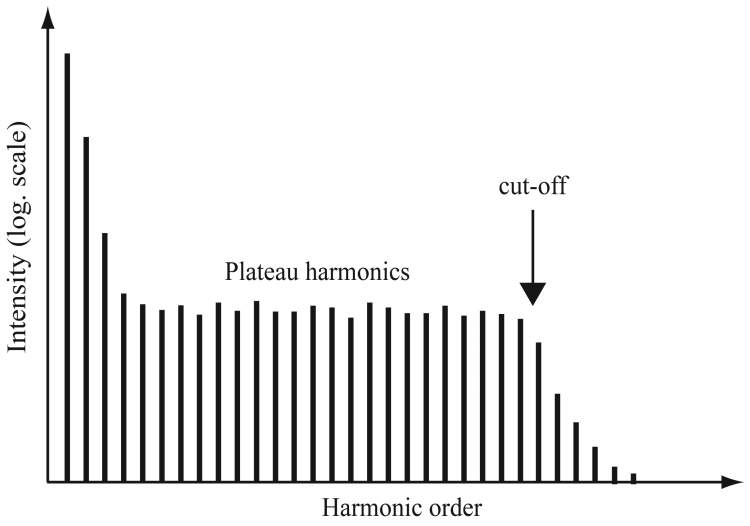

Figure 2.1: The general form of an HHG spectrum. The intensity falls off dramatically over the first few harmonics, before a region of approximately constant intensity, ending with an abrupt cut-off.

approximation was formulated by Lewenstein et al.[28] which recovered Corkum's theory.

2.1 Simple Man's Theory

In Corkum's model, the HHG process is described in terms of three distinct steps, as illustrated in Figure 2.2.

1. Ionization. An electron is in an unperturbed ground state until some moment in the laser pulse, at which time it is instantly ionised.

2. Propagation. The electron is released at rest and is now a free particle. It follows a classical trajectory under the oscillating electric force of the laser field.

3. Recombination. The electron recollides with the ion and a harmonic photon is released, with an energy equal to the kinetic energy of the electron on impact, plus its binding energy, I_{p}.

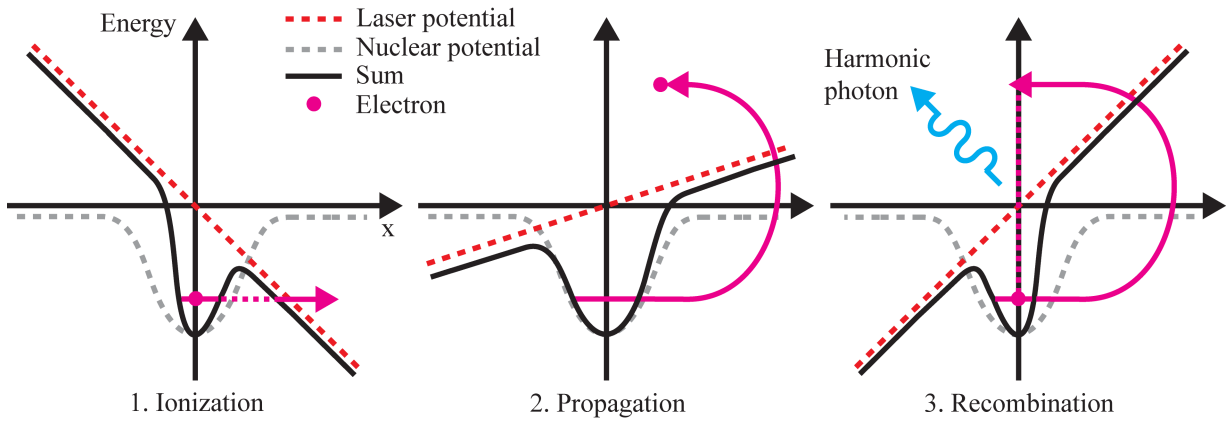

Figure 2.2: The 3-step model of HHG from an atom. 1. The atom is ionised. 2. The electron propagates in the continuum. 3. The electron recombines with the parent atom, with the release of a harmonic photon.

For a sinusoidal electric field $E(t) = E_0 \cos(\omega t)$, the classical equations of motion give, for the position of the electron at time t, after being ionised at time t_0:

$$x(t, t_0) = \frac{eE_0}{m\omega^2}[\cos(\omega t_0) - \cos(\omega t) - (\omega t - \omega t_0)\sin(\omega t_0)]. \tag{2.1}$$

The trajectory of the electron depends on the phase, $\phi_b = \omega t_0$, of the driving electric field at the time of ionization. Figure 2.3 plots the electron position as a function of time for various ϕ_b, where $\phi_b = 0$ corresponds to ionization at the peak of the driving pulse. For $0 \leq \phi_b \leq \pi/2$ the electron is accelerated away from the parent ion until the electric field changes sign, sending the electron back towards the ion where it can recombine. For $\pi/2 \leq \phi_b \leq \pi$ the electron trajectory does not return to the parent ion. This is repeated for the second half of the electric field cycle.

The velocity, and hence the kinetic energy of the electron when it recollides can be evaluated numerically as a function of ϕ_b and this is shown in Figure 2.4. The greatest kinetic energy on recollision is obtained when the electron is released 0.3 radians past the peak of

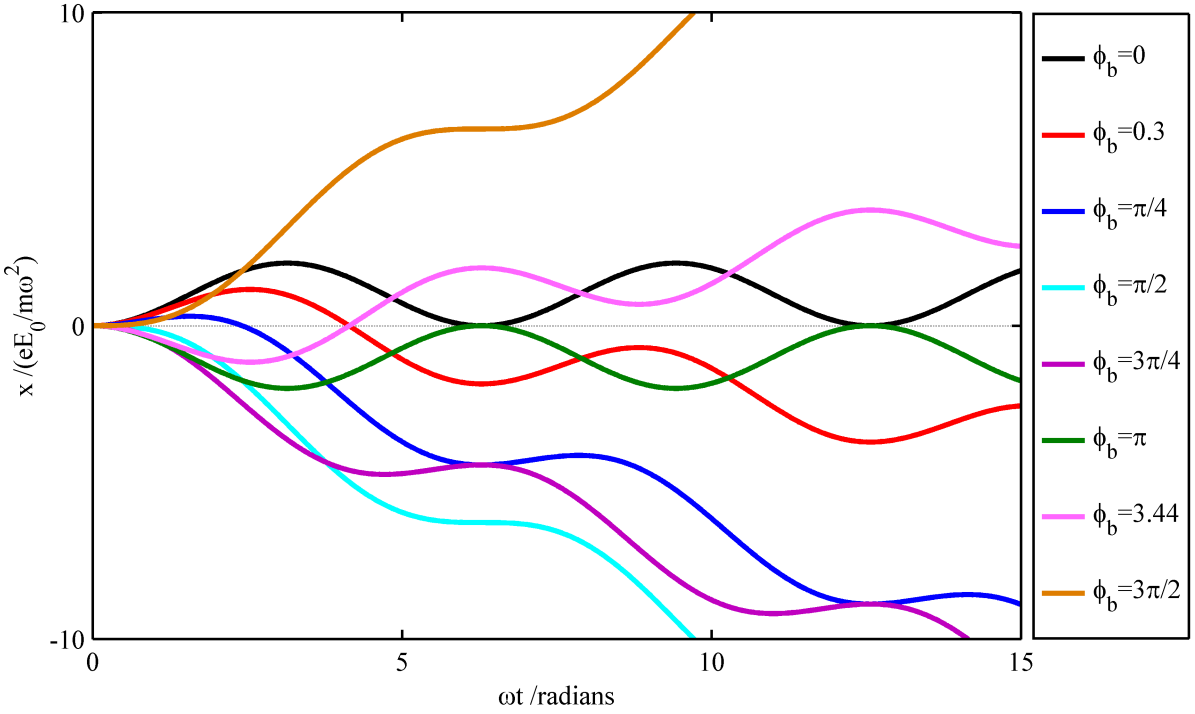

Figure 2.3: Electron trajectories for ionisation at times $t_0 = \phi_b/\omega$ in a linearly-polarised electric field $E(t) = E_0 \cos(\omega t)$. Electrons ionized at phases $0 \leq \phi_b \leq \pi/2$ of the driving electric field recombine, whereas those with $\pi/2 \leq \phi_b \leq \pi$ do not return to the parent ion.

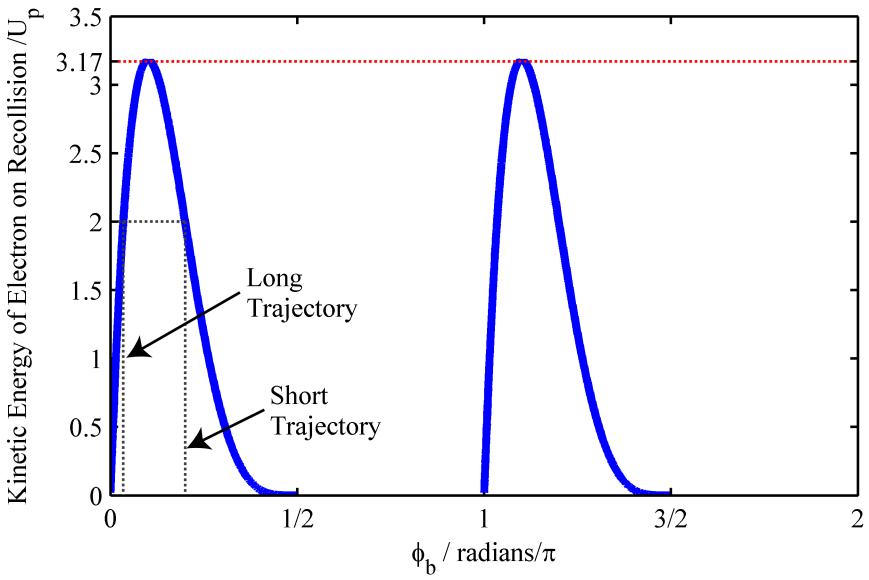

Figure 2.4: Kinetic energy of electrons on recollision, as calculated from Equation (2.1). The maximum energy is seen to be $3.17U_\mathrm{p}$. For other recollision energies, it can be seen that there are two possible trajectories every half-cycle of the driving electric field.

the electric field, giving a recollision energy of $3.17U_\mathrm{p}$, where $U_\mathrm{p} = e^2E_0^2/4m\omega_0^2$ is known as the ponderomotive energy. The maximum energy of the photon emitted on recollision, corresponding to the cut-off energy of the HHG spectrum, is then:

$$E_\mathrm{cutoff} = I_\mathrm{p} + 3.17U_\mathrm{p} \tag{2.2}$$

which agrees well with the cutoffs observed in experimental data[29]. We can also see from Figure 2.4 that for every half-cycle of the electric field, there are two possible values of ϕ_b which give any particular return energy $< 3.17U_p$. The path originating from the earlier ϕ_b is known as the long trajectory while the path originating from the later ϕ_b is known as the short trajectory, since it spends less time in the continuum before recombining. For the cut-off harmonic (corresponding to a return energy of $3.17U_\mathrm{p}$), there is only one trajectory.

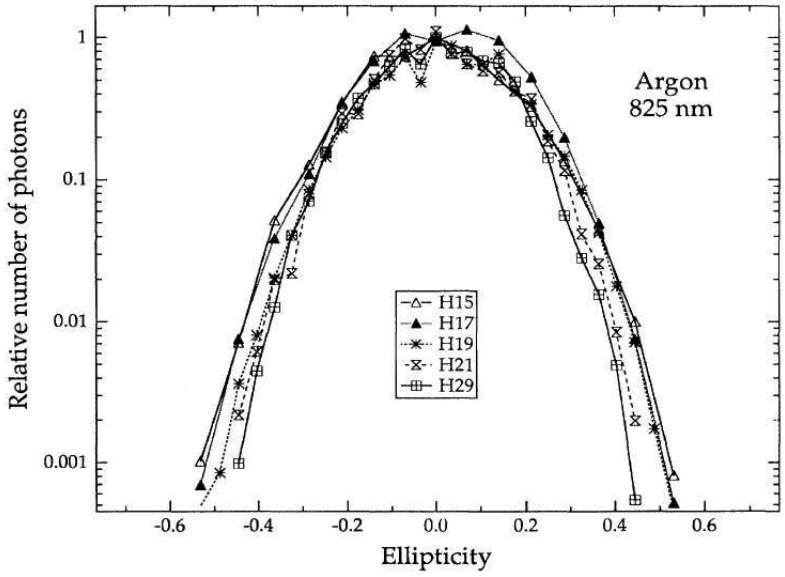

Figure 2.5: Intensity of the 15-29th harmonics of an 825 nm driving field with intensity $3.5 \times 10^{14}\,\mathrm{Wcm}^{-2}$ as a function of the ellipticity of the polarisation. Each harmonic intensity is normalised to its value at zero-ellipticity. Figure from [30]

This simple 3-step theory also suggests that HHG from atoms in elliptically-polarised electric fields should be suppressed, since in this case the trajectory will not pass through the parent ion after ionization and therefore cannot recombine. This was demonstrated experimentally by Budil et al[30]. Figure 2.5 shows the intensities of the 15–29th harmonics of an 825 nm driving field with intensity $3.5 \times 10^{14}\,\mathrm{Wcm}^{-2}$, for various ellipticities of the polarisation. For each harmonic, the intensity is normalised to the value at an ellipticity of zero. It can be seen that the harmonic yield is strongly dependent on the ellipticity of the polarisation of the driving laser field, supporting Corkum's simple model.

2.2 The Lewenstein Model

The Lewenstein model is a semi-classical formulation of the simple man's theory, based on the strong-field approximation. A full derivation of the theory can be found in the literature [28].

Presented here is a description of the theory in terms of the "physical" 3-step model described above. In this section, all quantities are expressed in atomic units ($\hbar = e = m_e = a_0 = 1$).

In the length gauge, the time-dependent Schrodinger equation (TDSE) for the interaction of an electron experiencing an atomic potential $V(\mathbf{r})$ and laser electric field $E(t)$ is given by:

$$i\frac{\partial}{\partial t} \mid \psi(\mathbf{r},t)\rangle = \left[-\frac{\mathbf{p}^2}{2} + V(\mathbf{r}) - \mathbf{E}(t).\mathbf{r}\right] \mid \psi(\mathbf{r},t)\rangle. \tag{2.3}$$

Numerical methods can be used to solve the TDSE without any further assumptions. This is a powerful and accurate method but computationally very intensive. It is also difficult to obtain a physical understanding of the process from a purely numerical treatment.

The Lewenstein model proceeds by making the following assumptions:

1. The influence of the atomic potential on the electron in the continuum can be ignored (the strong-field approximation).

2. All bound states other than the ground state may be neglected.

3. Depletion of the ground state is negligible.

   This is true if the driving intensity is less than the saturation intensity, I_{sat}, so that most of the electron population stays in the bound state. For argon, $I_{\text{sat}} \approx 5 \times 10^{14}\,\text{Wcm}^{-2}$.

With these assumptions, an exact analytical expression for the dipole moment can be derived.

We will consider a driving laser pulse of intensity-FWHM duration τ_p linearly-polarised along the x-direction ($\mathbf{E}(t) = E_x(t)$ and $\mathbf{d}(\mathbf{p}) = d_x(\mathbf{p})$), with electric field given by:

$$E(t) = E_0 \exp\left(-\frac{2\ln 2}{\tau_p^2}t^2\right)\cos(\omega t). \tag{2.4}$$

The time-dependent dipole moment in the x-direction is then found to be:

$$\begin{aligned}\langle x(t)\rangle &= i\int_0^\infty \mathrm{d}\tau \int_0^\infty \mathrm{d}^3p\, E(t-\tau)d(p-A(t-\tau)) \times \exp(-iS(p,t,\tau)) \times d^*(p-A(t)) + c.c. \\ &\approx i\int_0^\infty a_{\mathrm{ion}}(t,\tau) \times a_{\mathrm{prop}}(t,\tau,p_s) \times a_{\mathrm{recom}}(t,p_s)\,\mathrm{d}\tau + c.c. \end{aligned} \tag{2.5}$$

It can be seen that the dipole is expressed as the product of a complex probability amplitude from each of the 3-steps of Corkum's model, described above. The time interval between ionization and recombination is denoted by τ, $A(t)$ is the vector potential of the laser field, $E(t) = -\frac{\partial A(t)}{\partial t}$, p is the canonical momentum, $d(k)$ is the atomic dipole matrix element between the bound state and continuum state with momentum $k = p - A(t)$ and S is the quasi-classical action of the ionized electron. The integral over p has been eliminated by applying a saddle-point approximation, as we shall see below.

2.2.1 Ionisation

The first factor in Equation (2.5) is related to the probability amplitude for an electron to make the transition into the continuum at a time $t - \tau$ with a momentum p:

$$a_{\mathrm{ion}}(t,\tau) = E(t-\tau)d(p-A(t-\tau)). \tag{2.6}$$

The model used for the ionization depends on the parameter regime. From Figure 2.2 it can be seen that the net potential seen by a bound electron has a local maximum which depends on the peak laser field. If the laser intensity is such that this maximum is equal or lower than the energy of the bound electron, "over-the-barrier" ionization can occur. However, even at intensities lower than this critical value, ionisation can still occur by tunneling of the electron through the potential barrier. Ionisation by this distortion of the binding potential

by a strong laser field is known as "optical field ionisation" (OFI). This mechanism requires there to be sufficient time between cycles of the laser field for the electron wavepacket to move over or through the potential barrier. This condition is equivalent to:

$$\gamma = \frac{\omega_0}{E_0 e}\sqrt{2I_{\mathrm{p}} m_e} < 1, \tag{2.7}$$

where I_{p} is the ionization energy and γ is the Keldysh parameter[31]. In the regime typical for HHG experiments, the intensity is high enough and the laser frequency low enough for this condition to be satisfied.

We can therefore use the static ADK model for the tunnel-ionization rate in an intense, low-frequency laser field[32] to approximate the a_{ion} term. The ADK ionisation rate is given by[33]:

$$w_{\mathrm{ADK}}(t) = I_{\mathrm{p}}|C_{n^*}|^2 \left(\frac{2(2I_{\mathrm{p}})^{\frac{1}{2}}}{E(t)}\right)^{2n^*-1} \exp\left(-\frac{2(2I_{\mathrm{p}})^{\frac{3}{2}}}{3E(t)}\right). \tag{2.8}$$

Where Z is the degree of ionization and $n^* = Z(2I_p)^{-\frac{1}{2}}$ is the effective principle quantum number. The parameter $C_{n^*} \approx 2$ takes into account the atomic species and initial electronic configuration. This ionization rate can be used to calculate the free electron density $n(t)$ as a function of time for an intital gas density n_0:

$$n(t) = n_0\left(1 - \exp\left[-\int_{-\infty}^{t} \mathrm{d}t' w(t')\right]\right), \tag{2.9}$$

The ionisation factor, $a_{\mathrm{ion}}(t,\tau)$ is then given by:

$$a_{\mathrm{ion}}(t,\tau) = \sqrt{\frac{\mathrm{d}n(t-\tau)}{\mathrm{d}t}} \tag{2.10}$$

2.2.2 Propagation

The propagation amplitude, $a_{\rm prop}$ represents the electron wavefunction being propagated for a time τ, acquiring a phase factor equal to $\exp[-iS(p,t,\tau)]$, where $S(p,t,\tau)$ is the quasiclassical action. The effect of the atomic potential is assumed to be negligible during this process (the strong-field approximation), so that $S(p,t,\tau)$ actually describes the motion of an electron moving freely in the laser field, with a constant canonical momentum p:

$$S(p,t,\tau) = \int_{t-\tau}^{t} \mathrm{d}t'' \left[\frac{(p - A(t''))^2}{2} + I_p \right]. \tag{2.11}$$

Note, however that $S(p,t,\tau)$ does have some dependence on the atomic potential, through $I_{\rm p}$.

In equation (2.5) the integral over p is performed using a saddle-point approximation. The major contribution to the integral over p occurs at the stationary points of the action, given by:

$$\begin{aligned} \nabla_p S(p,t,\tau) &= \int_{t-\tau}^{t} \mathrm{d}t''[(p - A(t''))] \\ &= \int_{t-\tau}^{t} \mathrm{d}t'' v(t'') = x(t) - x(t-\tau) = 0. \end{aligned} \tag{2.12}$$

This equation expresses the fact that the dominant electron trajectories involve the electron returning to the starting point after a time τ. The saddle-point value of p is then given by:

$$p_s(t,\tau) = \frac{1}{\tau} \int_{t-\tau}^{t} \mathrm{d}t'' A(t'') \tag{2.13}$$

The propagation amplitude of equation (2.5) is then:

$$a_{\text{prop}}(t, \tau, p_s) = \left(\frac{2\pi}{i\tau}\right)^{\frac{3}{2}} \exp\left(-iS(p_s, t, \tau)\right). \tag{2.14}$$

This is a complex number with a constant amplitude, however the phase is equal to that which the electron accumulates during propagation in the continuum. Because the electron accumulates phase faster than the fundamental field, the propagation amplitude oscillates many times faster than the fundamental optical field, leading to high-harmonic frequencies.

The prefactor $(2\pi/i\tau)^{\frac{3}{2}}$ comes from the saddle-point integration and represents quantum diffusion of the electron wavefunction. The electronic wavepacket expands with time, which cuts off the contributions from large τ. In practice the integral over τ may therefore be extended over just one optical cycle.

2.2.3 Recombination

The final term represents the probability amplitude for the electron to recombine at time t:

$$a_{\text{recom}}(t, p_s) = d^*(p_s - A(t)). \tag{2.15}$$

The recombination amplitude is the expectation value of the dipole operator using the total electronic wave function: the part in the ground state plus the part returning from the continuum. Only the terms mixing the ground state and returning wave contribute to HHG. The returning electronic wave is approximated as a plane wave:

$$a_{\text{recom}}(t, p) \propto \int \psi_{\text{ground}} x \exp\left(ipx\right) \mathrm{d}x \tag{2.16}$$

It is well known[28] that the features of harmonic generation do not depend critically on the precise shape of the atomic potential. For Hydrogen-like atoms and transitions from s-states, the field-free dipole matrix elements can be approximated by[28]:

$$d^*(p_s - A(t)) = i\frac{2^{\frac{7}{2}}\alpha^{\frac{5}{4}}}{\pi}\frac{p_s}{(p_s^2+\alpha)^3} \tag{2.17}$$

with $\alpha = 2I_\mathrm{p}$.

2.2.4 The High-Harmonic Spectrum

The spectrum of the harmonic intensity is given by the square of the Fourier transform of the second derivative of the dipole moment with respect to time:

$$I(\omega) \propto \left| \int \frac{\partial^2 \langle x(t) \rangle}{\partial t^2} e^{i\omega t} \mathrm{d}t \right|^2 \tag{2.18}$$

However, in the literature the dipole moment $\langle x(t) \rangle$ is more commonly used than the dipole acceleration. Bandrauk et al.[34] have calculated the harmonic spectrum of Hydrogen using the dipole moment, velocity and acceleration. The spectra agreed well unless the peak intensity of the driving field was greater than the threshold intensity for over-barrier ionization, or the pulse duration was in the few-cycle regime. I will henceforth consider the spectrum based on the Fourier transform of the dipole moment rather than the acceleration, both to aid comparison with published results and because I will be considering intensity regimes where the two approaches give very similar results. The intensity spectrum is therefore given by:

$$I(\omega) \propto \left| \int \langle x(t) \rangle e^{i\omega t} dt \right|^2 \tag{2.19}$$

Figure 2.6 shows the single-atom harmonic spectrum in argon calculated by the author

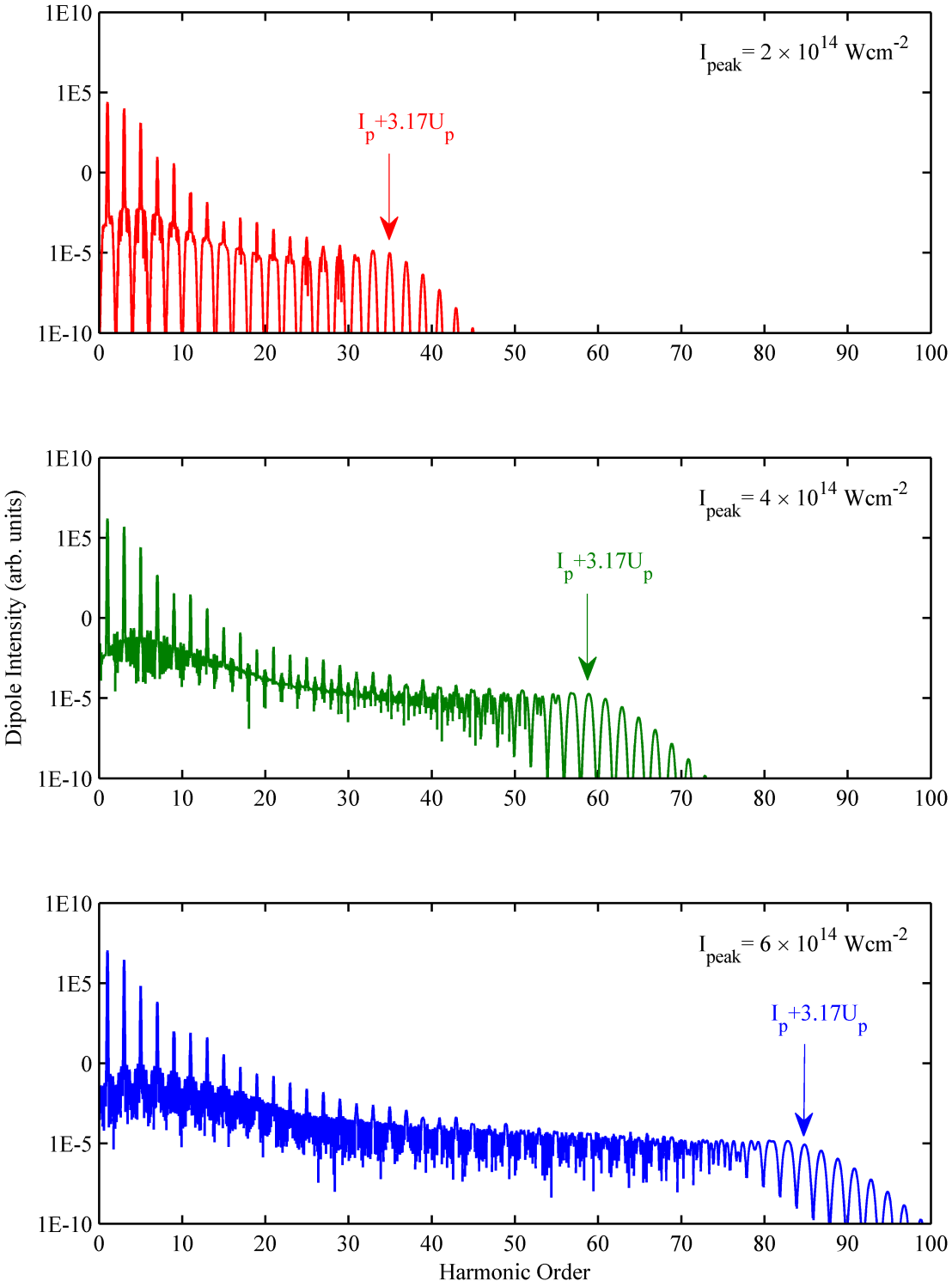

Figure 2.6: Calculated HHG spectra from a single atom of argon exposed to a driving laser pulse with $\lambda_0 = 800\,\text{nm}$ and $\tau_p = 50\,\text{fs}$, and peak intensities of $2 - 6 \times 10^{14}\,\text{Wcm}^{-2}$.

for $\lambda_0 = 800\,\text{nm}$ and $\tau_p = 50\,\text{fs}$, at various peak intensities. The typical shape of an HHG spectrum can be seen: there is a sharp fall-off in intensity for the first few well-resolved odd harmonics, before levelling off into the plateau region, followed by a sharp cut-off. The frequency of the cut-off is shown to agree well with the classical prediction of Equation (2.2). It is apparent that only odd harmonics of the driving frequency are present - this is because harmonics are generated at the two peaks of the driving electric field amplitude which occur every cycle. In the frequency domain this leads to harmonic frequencies spaced by twice the driver frequency. Also, from considerations of symmetry, the induced polarization of a centrosymmetric single atom or gas must be an odd function of the electric field, leading to odd harmonics.

The distinct harmonic peaks are seen to disappear in the plateau region. A plateau harmonic is largely formed from two relevant contributions, corresponding to the long and short electron trajectories in the continuum. As we shall see in Section 2.2.6, these trajectories experience different intensity-dependent phase contributions[35], since they spend different lengths of time in the continuum. As the laser intensity varies in time, these two contributions will be subject to different frequency shifts, leading to a splitting of the harmonic peaks[36]. The plateau structure is also explained by the fact that these harmonics are produced over many optical cycles and at different points during the driver pulse. For ultrashort pulses the second as well as first time derivatives can vary rapidly. Therefore electrons entering the continuum at different times can experience rapidly increasing or decreasing intensities and will accelerate and radiate with blueshift or redshift respectively on recombination.

Distinct peaks are seen in the cutoff region since these harmonics are only generated during a short time interval at the peak of the pulse and therefore at a small range of intensities. There is also only one relevant electron trajectory here and so splitting does not occur.

However, the structure in the plateau seen in Figure 2.6 is not observed in experimental HHG spectra, where well-defined harmonic peaks are generally observed throughout the spectrum. Simulated spectra are in much closer agreement with experimental results if propagation of the driving laser and harmonic pulse are included[37, 38]. It is found that phase-mismatch due to free electrons, as well as variations in phase due to longitudinal and radial variations of both intensity and phase of the driving pulse, selectively reduce the contribution of some trajectories, simplifying the spectrum considerably.

2.2.5 Time-Frequency Analysis

The Fourier transform of the dipole moment gives us the frequency spectrum integrated over the duration of the driving pulse. However, the instantaneous spectrum of the generated radiation will vary throughout the pulse. In order to retrieve this information, time-frequency analysis must be performed on the dipole moment $\langle x(t)\rangle$.

Time-resolved spectra can be obtained by performing a wavelet transform[39] of the dipole moment, given by:

$$A_w(t_0,\omega) = \int x(t) w_{t_0,\omega}(t)\mathrm{d}t \equiv x_\omega(t) \tag{2.20}$$

Where $w_{t_0,\omega}(t) = \sqrt{\omega}W(\omega(t-t_0))$ is a windowed, oscillating function of finite temporal extent, centred at $t = t_0$ and $W(\omega(t-t_0))$ is the "mother wavelet". The usual choice is the Morlet wavelet:

$$W(y) = \frac{1}{\sqrt{y_0}} \exp(iy) \exp(-y^2/2y_0^2). \tag{2.21}$$

The parameter y_0 determines the balance between the resolutions in the frequency and time domains, with the Fourier transform recovered for $y_0 \to \infty$. This wavelet is used in the calculations presented here, with $y_0 = 15$. As one can note from the expression of the Morlet wavelet, for a given y_0 and for the fixed frequency $\omega = q\omega_0$, one can achieve resolution of

the order of $y_0 T/2\pi q$ in the temporal domain (where T is the period of the driving field). The dependence of $x_\omega(t)$ on the parameter y_0 was tested by varying its value from 5 to 30. Although the absolute value of $x_\omega(t)$ changes a little, the general pattern does not change. Figure 2.7 shows a plot of the modulus-squared of the wavelet transform of the dipole moment for an 800 nm driving laser pulse of peak intensity $2 \times 10^{14}\,\mathrm{Wcm}^{-2}$ and $\tau_p = 50\,\mathrm{fs}$. Figure 2.8 shows the intensity as a function of time for the 3rd, 5th, 25th, 31st and 51st harmonics, obtained by taking cross-sections of Figure 2.7 at the appropriate frequencies.

Several features of interest can be seen in this time-frequency representation. Firstly, the time profiles of the first few harmonics are smooth and closely mirror the intensity of the driving laser pulse, as can be seen in Figure 2.8a. This indicates that the multiphoton mechanism dominates for these harmonics. In this regime, the probability of the atom absorbing n photons is approximately proportional to I^n, where I is the laser intensity, $I(t) \propto E(t)^2$.

In the plateau region ($q > 15$) the time profiles exhibit fast bursts of radiation, as shown in Figure 2.8b. These bursts occur twice every cycle of the driving laser field and form a continuous frequency profile in Figure 2.7. This corresponds to the electron wavepacket recolliding with the ionic core twice per laser cycle, as described in the 3-step model, leading to emission of harmonic radiation. In the intermediate frequency region ($q \approx 10$), where both multiphoton and tunneling mechanisms contribute, the time-frequency plot exhibits a grid-like structure.

Figure 2.8c plots the emission strength as a function of time for the 31st harmonic, which is just below the cutoff region. For this harmonic there are now two peaks per half-cycle of the driving electric field. These two peaks arise from the two electron trajectories which can contribute to emission of a particular harmonic in the plateau region. For a cutoff harmonic, such as the 51st, plotted in Figure 2.8d, there is only one contributing trajectory

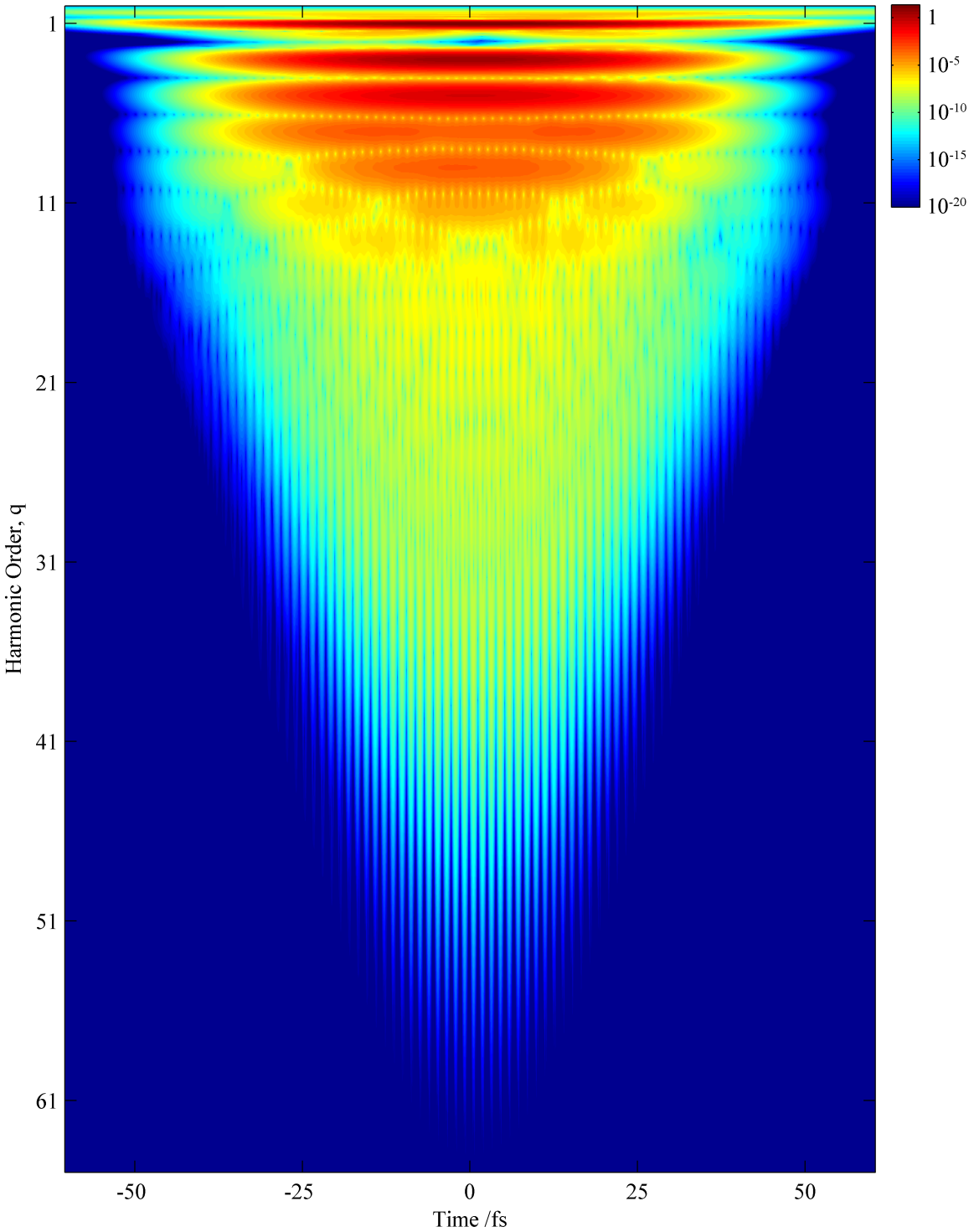

Figure 2.7: A wavelet transform of the single argon atom dipole moment (modulus squared) for an 800 nm driving pulse of intensity $2 \times 10^{14}\,\mathrm{Wcm}^{-2}$ and $\tau_p = 50\,\mathrm{fs}$.

and therefore only one burst of emission per half-cycle.

2.2.6 Intensity-Dependent Phase

The phase of the harmonic light is made up of two components: the phase of the driving field and the phase accumulated by the electron wavepacket while it propagates in the continuum, known as the dipole phase. In Section 2.2.2 we saw that this dipole phase is given by the quasiclassical action. The total phase of the qth harmonic is therefore given by:

$$\Phi = q\omega t - S(p, t, \tau) \tag{2.22}$$

One consequence of this is that since the long and short electron trajectories which contribute to a particular plateau harmonic propagate for different durations τ in the continuum, they will contribute different phases to that harmonic.

The dipole phase is also intensity-dependent, which becomes apparent from the following analysis[40]. From equation (2.1), the classical expression for the velocty of an electron ionised at time $t - \tau$ and recombining at time t, in atomic units is given by:

$$v(t, \tau) = \frac{E_0}{\omega}[\sin(\omega t) - \sin(\omega(t - \tau))] \tag{2.23}$$

and the quasiclassical action is, from Equation (2.11):

$$S(t, \tau) = \int_{t-\tau}^{t} \mathrm{d}t'' \left\{ \frac{[p_e(t, \tau)]^2}{2} + I_p \right\} \tag{2.24}$$

where $p_e(t, \tau)$ is the momentum of the electron ionised at time $t - \tau$.

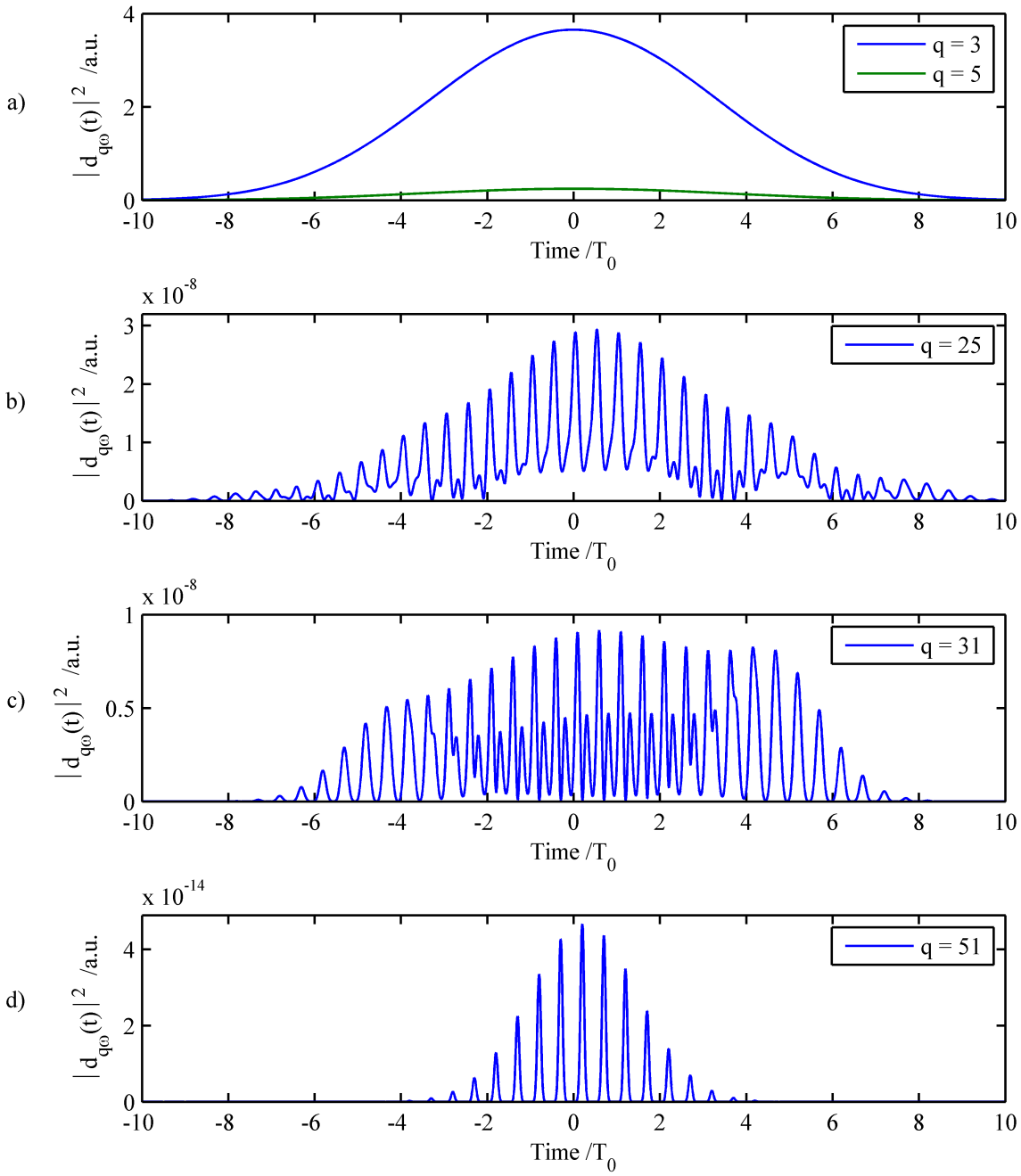

Figure 2.8: Cross-sections of the time-frequency plot shown in Figure 2.7. Plotted are: a) the 3rd and 5th harmonic, b) the 25th plateau harmonic, c) the 31st plateau harmonic and d) the 51st harmonic, in the cut-off region, all as a function of time, in units of the driving laser electric field period, $T_0 = 2\pi/\omega_0$.

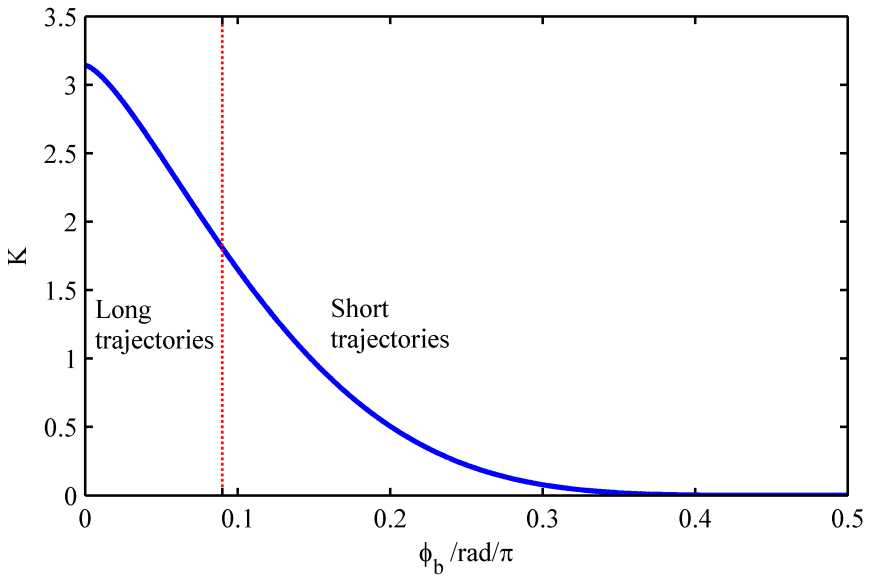

Figure 2.9: K as a function of ϕ_b, the laser phase at the moment of ionisation. Long trajectories correspond to $\phi_\mathrm{b} < 0.09$. It is seen that K is greater for the long trajectories than the short ones.

This gives, for the dipole phase:

$$\Phi_\mathrm{dipole} = -\frac{I_\mathrm{p}}{\omega}(\phi - \phi_\mathrm{b}) - \frac{2U_\mathrm{p}}{\omega}\int_{\phi_\mathrm{b}}^{\phi}(\sin\phi - \sin\phi_b)^2\mathrm{d}\phi \tag{2.25}$$

where $\phi = \omega t$ and $\phi_\mathrm{b} = \omega(t-\tau)$. The dependence on the driving intensity is then given by:

$$\frac{\partial\Phi_\mathrm{dipole}}{\partial I} = -\frac{2K}{\omega}\frac{\partial U_\mathrm{p}}{\partial I} = -\frac{K}{\omega^3\epsilon_0} \tag{2.26}$$

where $K = \int_{\phi_\mathrm{b}}^{\phi}(\sin\phi - \sin\phi_b)^2\mathrm{d}\phi$ is a dimensionless constant with a value which depends on the electron trajectory. This expression, together with equation (2.1) can be used to calculate K as a function of ϕ_b, the laser phase at the moment of ionisation. Figure 2.9 shows that K is greater for long trajectories than short ones: the phase of the long trajectories is therefore more sensitive to the intensity than the short.

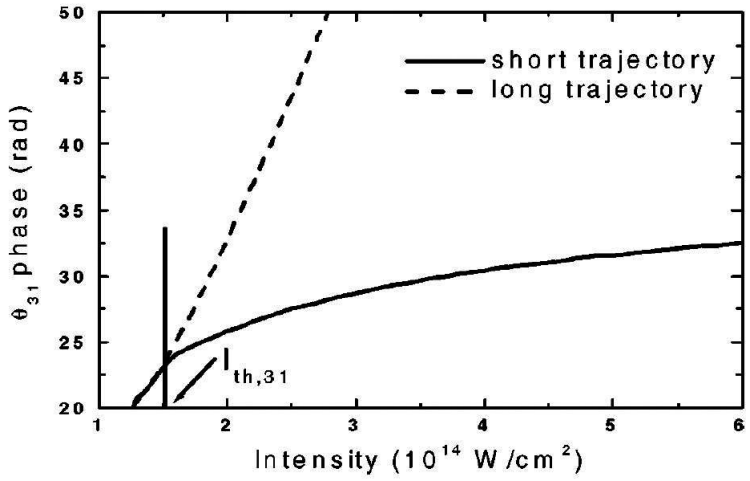

Figure 2.10: Dipole phase of the 31st harmonic from Ar driven by a 30 fs laser pulse, as a function of driving intensity. The solid line indicates the harmonic phase of the short trajectory and the dashed line indicates the phase of the long trajectory. From [41].

Figure 2.10 shows a full analytical calculation of the phase of the 31st harmonic generated in argon as a function of the intensity of an 800 nm driver[41]. The individual contributions of the long and short trajectories are shown, the slopes of which are determined by K. The value of $\partial\phi/\partial I$ is approximately 16, 22 and 3 radians/$(10^{14}\,\mathrm{Wcm}^{-2})$ for the cut-off, long-trajectory plateau and short-trajectory plateau harmonics respectively. It is found that these values are quite universal, i.e. independent of atomic number and harmonic order[35].

The intensity-dependent dipole phase has a significant effect on the spectral and temporal effects of harmonics, since in an ultrafast driving pulse the intensity varies significantly from cycle to cycle of the electric field. For example it leads to spectral broadening of the harmonics, since the intensity dependent phase leads to a blueshift of the harmonic radiation on the rising edge of the driving pulse and a redshift on the falling edge.

2.2.7 Conclusion

The HHG mechanism has been described and a model for the process, based on the strong field approximation, has been outlined. This model will be used in later chapters as a basis for simulations of HHG in a capillary waveguide and of the CPX experiment. Time-frequency analysis has been used to gain insights concerning the dynamics of the process and the intensity-dependence of the phase of the generated harmonic light has been investigated.

We have so far considered the high-harmonic process in terms of a single atom. We have already seen that the spectra obtained from modelling a single atom differ in some respects to those measured experimentally, due to propagation effects associated with generating harmonics in a macroscopic medium. The most significant of these effects is dephasing between the fundamental and harmonic fields, which will be discussed in the next chapter.

Chapter 3

Phase-Matching

In the previous chapter, the single-atom process of HHG was investigated, but in practice harmonic generation takes place in a macroscopic medium. The build-up of the harmonic field involves propagation of both the driver and harmonic pulses in an ionizing gas, where processes such as self-phase modulation, blue-shifting and defocusing can have a significant impact on the XUV yield. However, the most significant propagation effect is that of phase-mismatch due to the dispersion of the medium. In this chapter I will describe the major sources of dispersion when generating high-harmonics and introduce the concept of phase-matching, as well as the closely-related principle of quasi-phase-matching. I will present previous experimental demonstrations in which both of these principles have been used to increase HHG conversion efficiency.

3.1 Phase-Mismatch

A major source of inefficiency in HHG is due to phase-mismatch between the driving laser field and the harmonic field. This arises due to the dispersion of the medium in which the

harmonics are generated, leading to different phase velocities for the fundamental and harmonic frequencies. This means that harmonics generated at a particular point in the medium will not, in general, be in phase with the harmonic wave at that point, potentially leading to destructive interference. We here consider the generation of harmonics (not necessarily high-harmonics) within such a medium.

Consider a continuous-wave (CW) field of frequency ω and peak electric field E_0 propagating in the positive z-direction through a nonlinear dispersive medium which occupies $0 < z < L$. If x is the direction of the electric field and induced polarisation and the wavevector is assumed to be independent of z, the wave equation for the driving electric field is satisfied by:

$$E^{(\omega)}(z,t) \approx \frac{E_0^{(\omega)}}{2} e^{-i[\omega t - k(\omega) z]} + \text{c.c.} \tag{3.1}$$

The atoms at $z = 0$ therefore experience a driving field given by

$$E^{(\omega)}(0,t) = \frac{E_0^{(\omega)}}{2} e^{-i\omega t} + \text{c.c.} \tag{3.2}$$

Due to the nonlinear response of the atoms there will be an oscillating polarisation at harmonic frequencies $q\omega$:

$$P_{\text{NL}}^{(q\omega)}(0,t) = \frac{P_{\text{NL},0}^{(q\omega)}}{2} e^{-iq\omega t} + \text{c.c.} \tag{3.3}$$

also in the x-direction. The nonlinear coefficient $P_{\text{NL},0}^{(q\omega)}$ is a complex quantity and is a function of $E_0^{(\omega)}$ and the atomic species.

The electric field $E^{(\omega)}$ is known for all z and t. For any z, the electric field is identical to

the time-delayed electric field at $z = 0$, given by:

$$E^{(\omega)}(z,t) = E^{(\omega)}\left(0, t - \frac{k(\omega)z}{\omega}\right) \tag{3.4}$$

The polarization wave must obey this same time-delay relation for $z > 0$, since it does not depend on the polarization at other values of z and the system is invariant under time translation. This gives:

$$\begin{aligned} P_{\mathrm{NL}}^{(q\omega)}(z,t) &= P_{\mathrm{NL}}^{(q\omega)}\left(0, t - \frac{k(\omega)z}{\omega}\right) \\ &= \frac{1}{2}P_{\mathrm{NL},0}^{(q\omega)}e^{i[qk(\omega)z - q\omega t]} + \text{c.c.} \end{aligned} \tag{3.5}$$

This polarisation will drive an electric field oscillating at the same frequency. The harmonic wave, of frequency $q\omega$ then propagates according to Maxwell's wave equation:

$$\nabla^2 E^{(q\omega)} + k(q\omega)^2 E^{q\omega} = -\mu_0 q^2 \omega^2 P_{\mathrm{NL}}^{(q\omega)} \tag{3.6}$$

where $k(q\omega)^2 = (q\omega/c)^2\epsilon^{(1)}(q\omega)$, represents the linear part of the polarization. The solution to Equation (3.6) can be written in terms of an envelope function $\xi^{(q\omega)}(z)$:

$$E^{(q\omega)}(z,t) = \frac{1}{2}\xi^{(q\omega)}(z)e^{i[k(q\omega)z - q\omega t]} + \text{c.c.} \tag{3.7}$$

We can now substitute both Equation (3.7) and the polarisation expression (3.5) into Equation (3.6). Making the slowly-varying envelope approximation and neglecting the second spatial derivative of $\xi^{(q\omega)}(z)$ (since it is assumed to vary on a length scale much longer than

$1/k(q\omega)$), this gives:

$$\frac{d\xi^{(q\omega)}}{dz} ik(q\omega) e^{i[k(q\omega)z - q\omega t]} + \text{c.c.} = -\frac{1}{2}\mu_0 q^2 \omega^2 P_{\text{NL},0}^{(q\omega)} e^{i[qk(\omega)z - q\omega t]} + \text{c.c.} \tag{3.8}$$

Since Equation (3.8) is equally valid at $t = 0$ and $t = \pi/2q\omega$ we can neglect the complex conjugate parts, giving:

$$\begin{aligned} \frac{d\xi^{(q\omega)}}{dz} &= \frac{i\mu_0 q^2 \omega^2 P_{\text{NL},0}^{(q\omega)}}{2k(q\omega)} e^{i[qk(\omega)z - k(q\omega)z]} && (3.9) \\ &= A^{(q\omega)} e^{-i\Delta k(q,\omega)} && (3.10) \end{aligned}$$

where

$$\Delta k(q, \omega) = k(q\omega) - qk(\omega) \tag{3.11}$$

and $A^{(q\omega)} = i\mu_0 q^2 \omega^2 P_{\text{NL},0}^{(q\omega)}/2k(q\omega)$.

The solution to this is

$$\begin{aligned} \xi^{(q\omega)}(z) &= \int_0^z A^{(q\omega)} e^{-i\Delta k(q,\omega)z} dz && (3.12) \\ &= \frac{A^{(q\omega)}}{i\Delta k(q,\omega)} \left(1 - e^{-i\Delta k(q,\omega)z}\right) && (3.13) \end{aligned}$$

with the intensity of the corresponding harmonic wave given by

$$\begin{aligned} I^{(q\omega)}(z) &= \frac{\epsilon_0 c}{2} \left|E^{(q\omega)}(z,t)\right|^2 = \frac{\epsilon_0 c}{2} \left|\xi^{(q\omega)}(z)\right|^2 && (3.14) \\ &= \frac{B^{(q\omega)}}{(\Delta k)^2} \sin^2\left(\frac{\Delta k}{2} z\right) && (3.15) \end{aligned}$$

where $B^{(q\omega)} = [A^{(q\omega)}]^2 \epsilon_0 c$.

In the phase-matched limit $\Delta k \to 0$ the growth becomes quadratic with propagation distance,

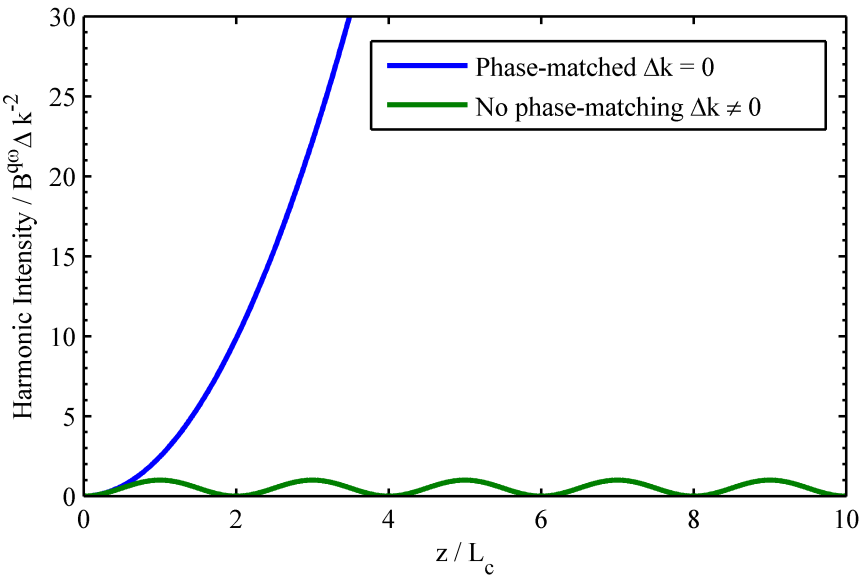

Figure 3.1: Harmonic intensity as a function of distance z into the generating medium, for the case of phase-matching and a phase-mismatch of Δk, as calculated from Equation (3.14).

z:

$$I^{(q\omega)}(z) = \frac{B^{(q\omega)}}{4} z^2 \tag{3.16}$$

The harmonic intensity as a function of distance within the nonlinear medium for both of these cases is shown in Figure 3.1. If harmonic generation is phase-matched ($\Delta k = 0$), then the harmonic intensity increases with distance monotonically. However, for the case $\Delta k \neq 0$, the harmonic intensity oscillates with a period $2L_{\mathrm{c}}$, where the coherence length, L_{c} is defined as the distance over which a π phase difference accumulates between the harmonic wave and the local phase of harmonic generation,

$$L_{\mathrm{c}} = \frac{\pi}{\Delta k}. \tag{3.17}$$

For $\Delta k \neq 0$, the maximum harmonic intensity is $B^{(q\omega)}/(\Delta k)^2$ and corresponds to that generated over one coherence length.

3.2 Phase-Matching of HHG in a Capillary

We now consider the specific case of HHG in a gas-filled hollow waveguide (capillary). The first experiments to investigate HHG typically used a free-focus geometry, with a gas jet as the generating medium. This geometry limits the generation region to the order of a Rayleigh length, due to defocusing and ionisation-induced refraction of the fundamental. However, as we shall see in the next chapter, if the focal spot size of the laser beam is matched to the lowest order mode of a capillary waveguide, the interaction region may be extended to many centimeters. Furthermore, since the interaction conditions vary less with longitudinal position, it becomes easier to phase-match over an extended distance. A capillary is also a useful "container", providing a well-defined region of the gas medium. It has also been shown that XUV light generated from a capillary waveguide has far greater spatial coherence than that produced in a gas jet, as measured by observing the visibility of a two-pinhole interference pattern[42]. This is because the lowest-order mode of the waveguide has a flat phase profile around the beam centre, as opposed to the free-focus geometry where the phase varies rapidly in the radial direction.

Despite these advantages, phase matching is still an issue in capillaries and dispersion still limits the intensity of the harmonic radiation which may be obtained.

3.2.1 Plasma Dispersion

High-harmonic generation involves ionisation and therefore the generated harmonic wave will propagate through a plasma. The index of refraction of a plasma is given by

$$n_{\text{plasma}} = \sqrt{1 - \left(\frac{\omega_p}{\omega}\right)^2} \quad \text{where} \quad \omega_p^2 = \frac{N_e e^2}{\epsilon_0 m_e}, \tag{3.18}$$

ω_p is the plasma frequency and N_e is the density of free electrons. For high-harmonics, the plasma frequency will in general be much less than the frequency of the IR or XUV light, therefore the wavenumber, k of the qth harmonic can be approximated as

$$k \approx \frac{\omega}{c}(1 - \frac{\omega_p^2}{2\omega^2}) = \frac{2\pi q}{\lambda_0} - \frac{N_e r_e \lambda_0}{q} \tag{3.19}$$

where $r_e = e^2/4\pi\epsilon_0 m_e c^2$ is the classical electron radius.

The phase mismatch between the fundamental and qth harmonic fields is therefore:

$$\Delta k = qk(\omega_0) - k(q\omega_0) = -N_e r_e \lambda_0 q + \frac{N_e r_e \lambda_0}{q^2}. \tag{3.20}$$

For high harmonics ($q \gg 1$) the second term can be discarded, giving

$$\Delta k_{\text{plasma}} \simeq -N_{\text{e}} r_{\text{e}} \lambda_0 q. \tag{3.21}$$

3.2.2 Neutral Gas Dispersion

Neutral atoms and ions also contribute to the dispersion of the medium. The ionic contribution is usually neglected, since for ionization fractions of over a few percent plasma dispersion dominates.

The refractive index $n(\lambda)$ of the neutral gas at STP (1 atm and 298 K) can be obtained from the relevant Sellmeier equation. Since the refractive index scales linearly with pressure, $n(\lambda)$ is then simply scaled by the gas pressure and the proportion of neutral, un-ionized atoms:

$$\Delta k_{\text{neutral}} = \frac{2\pi q}{\lambda_0}[n_{\text{gas}}(\lambda_0) - n_{\text{gas}}(\lambda_0/q)](1 - \eta)\frac{P}{P_{\text{atm}}} \tag{3.22}$$

where n is the refractive index of the gas at 1 atm, η is the ionization fraction and P is the gas pressure.

3.2.3 Waveguide Dispersion

As we will see in Chapter 4, waveguides also introduce dispersion. The correction to the wavenumber is given by (4.3):

$$\mathrm{Re}(k) = \frac{\omega}{c}\sqrt{1 - \left(\frac{u_{n,m}c}{\omega a}\right)^2} \approx \frac{2\pi q}{\lambda_0} - \frac{u_{n,m}^2 \lambda_0}{4\pi a^2} \tag{3.23}$$

where a is the inner radius of the capillary, and $u_{n,m}$ is the mth root of the $(n-1)$th Bessel function of the first kind, which specifies the coupled mode. The parameters of the input beam are usually chosen so that they are matched to the lowest-order mode, given by $n = 1$. The harmonic light is generally generated on-axis in the waveguide, where the intensity is peaked. The Rayleigh range is proportional to $1/\lambda$, so high harmonics can be assumed to not impinge on the capillary wall. The correction to the harmonic wavenumber can be neglected and the phase mismatch is simply:

$$\Delta k_{\mathrm{waveguide}} = -\frac{u_{n,m}^2 \lambda_0 q}{4\pi a^2}. \tag{3.24}$$

Equations 3.21 to 3.24 allow us to make an estimation of the phase-mismatch and therefore the coherence length, L_{c} in our generating medium. Of course, the discussion above is simplified by the assumption that the medium is uniform. In practice, the ionization fraction and hence L_{c} will vary with position in the medium and with time in the laser pulse.

3.2.4 Previous Demonstrations of Phase-Matching

The total phase mismatch for HHG in a gas-filled hollow waveguide, from the contributions discussed above is

$$\Delta k = \Delta k_{\text{plasma}} + \Delta k_{\text{neutral}} + \Delta k_{\text{waveguide}} \tag{3.25}$$

$$= -N_{\text{e}} r_{\text{e}} \lambda_0 q + \frac{2\pi q}{\lambda_0}[n(\lambda_0) - n(\lambda_0/q)](1-\eta)\frac{P}{P_{\text{atm}}} - \frac{u_{n,m}^2 \lambda_0 q}{4\pi a^2} \tag{3.26}$$

where the corrections may simply be added since they are all small compared with $k(\omega)$ and therefore $k(\omega)$ can be expressed as a first-order Taylor expansion. Since the different terms have different signs it is possible in principle to phase-match by balancing experimental parameters. This was accomplished by the group of Murnane and Kapteyn by tuning the gas pressure in capillary waveguides[43, 44]. Pulses from a Ti:sapphire multipass amplifier (4.5 mJ, 20 fs, 800 nm, 1 kHz) were focused into a capillary with $a = 75\,\mu$m, producing harmonics up to $q = 33$. Figure 3.2 shows the pressure tuning curves of the intensity of the 25th harmonic for a range of gases. It can be seen that the harmonic intensities exhibit clear maxima, corresponding to the pressures at which $\Delta k = 0$ is achieved.

3.2.5 Limits to Phase-Matching

Phase-matched high harmonics will grow quadratically with distance, assuming constant generation conditions. In this case the flux is only limited by absorption in the generating medium. Higher-order harmonics can be generated by increasing the intensity, however this will result in a greater free-electron density and unfortunately there is a limit to the level of ionization at which phase-matching is possible. Above a certain critical ionization fraction, η_{critical} the neutral gas dispersion is not great enough to compensate for the plasma

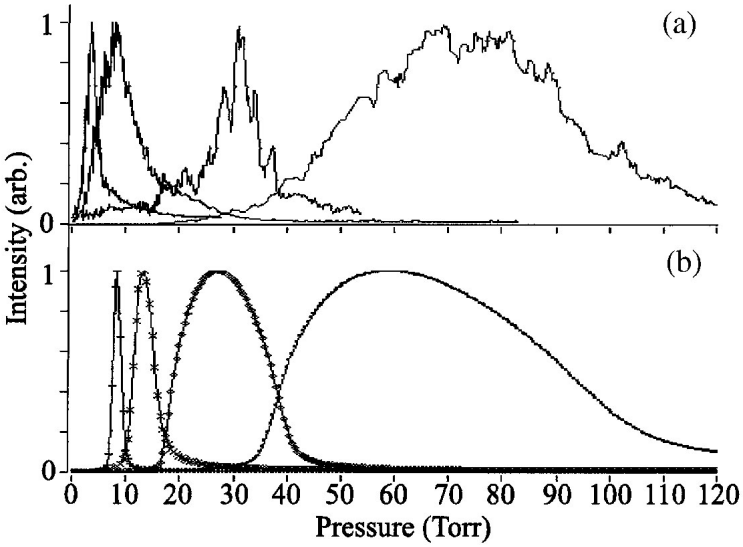

Figure 3.2: Measured (a) and calculated (b) pressure dependence of the harmonic intensity for several gases, exhibiting peaks which correspond to phase-matching. In order of increasing optimum pressure, the curves correspond to xenon, krypton, argon, and hydrogen. Figure from [43].

dispersion, whatever the pressure. This critical fraction is given by setting $\Delta k_{\text{plasma}} = \Delta k_{\text{neutral}}$, assuming that the waveguide dispersion is negligible in comparison, giving

$$\eta_{\text{critical}} = \left(1 + \frac{N_{\text{atm}} \lambda_0^2 r_e}{2\pi \left[n(\lambda_0) - n(\lambda_0/q)\right]}\right)^{-1} \tag{3.27}$$

For argon gas this gives $\eta_{\text{critical}} \approx 5\%$. The minimum cut-off wavelength this limit corresponds to can then be calculated using the ADK ionisation rates[32] to calculate the ionization fraction as a function of intensity and then using the cut-off rule (Equation 2.2). For a 50 fs, 800 nm driving pulse, this corresponds to a spectral limit to the phase-matched harmonic radiation of $\lambda > 26\,\text{nm}$.

In order to develop HHG as a useful source at higher photon energies, an alternative to pressure-tuned phase matching is therefore necessary.

3.3 Quasi-Phase-Matching

As we have seen, phase-mismatch limits the yield of harmonic generation and can only be eliminated by pressure-tuned phase-matching at low ionization levels. The related principle of quasi-phase-matching (QPM), circumvents this problem by periodically correcting the phase-mismatch.

In 1962, shortly after the birth of nonlinear optics, Armstrong et al. proposed "phase-corrective schemes", whereby the phase mismatch is corrected with a periodicity corresponding to twice the coherence length[45]. Within a few months of its proposal, QPM was applied to second-harmonic generation[46] in a stack of 250 μm quartz plates where the optical axis of adjacent plates alternated in direction by 180 degrees. This meant that the relative phase between the fundamental and the second harmonic radiation generated in the even plates differed by π to that generated in the odd plates. Since L_{c} was also 250 μm for the process, only constructive interference occurred. Periodically-poled ferromagnetic crystals have also been used to achieve QPM[47] and the poling pattern can be devised to match multiple frequencies[48]. Unfortunately, solid materials are not suitable for generating XUV light due to absorption and so these techniques cannot be used for HHG, where generation typically takes place in a gas.

A similar form of QPM involves suppressing the nonlinear process in alternate coherence lengths, eliminating regions of destructive interference and leaving only zones where the generated harmonics interfere constructively with the harmonic wave. Figure 3.3 shows the calculated intensity of the qth harmonic, plotted as a function of distance through a generating medium, for various QPM scenarios. It is seen that when the nonlinear coefficient $P^{q\omega}_{\mathrm{NL},0}$ is modulated every coherence length, the intensity of the harmonic radiation increases quadratically, as for perfect phase-matching. However the rate of growth is not

as fast as the phase-matched case since HHG is now effectively confined to only half of the generation medium. Also shown are the cases where the harmonic generation is modulated by less than 100% and where the periodicity of the modulations does not exactly match the coherence length.

Higher-order QPM is also possible, although it is not as efficient as the first-order process. QPM of nth-order corresponds to the non-linear process being modulated with a period given by $2nL_c$ where $n = 1, 3, 5, ...$ The harmonic intensity still grows with propagation distance, but more slowly than for first-order QPM.

Spatial modulation of the HHG process has been realized experimentally in a number of ways, by manipulating both the driving laser intensity and the density of the generation medium. These schemes are reviewed in the following section.

It is important to note that in the case of QPM, any measured "enhancement" in harmonic intensity is an ambiguous concept. Figure 3.3 shows that for certain lengths of medium, the harmonic intensity will be zero. If any kind of QPM is then applied, the apparent enhancement will be infinite. The enhancements quoted below should therefore be considered with this in mind. Indeed it could be argued that a better measure of enhancement would to compare the harmonic intensity obtained at a given wavelength, to the best that can be achieved in the absence of QPM with the *same* laser parameters, for example by using techniques such as pressure-tuned phase-matching.

3.3.1 Multiple Gas Jets

The use of a modulated gas density to apply QPM to HHG was first proposed by Shkolnikov[49] in 1994, but was not realized experimentally until 2007, when the group of Ferenc Krausz demonstrated QPM of HHG in two successive gas jets[50]. In this experiment, laser pulses

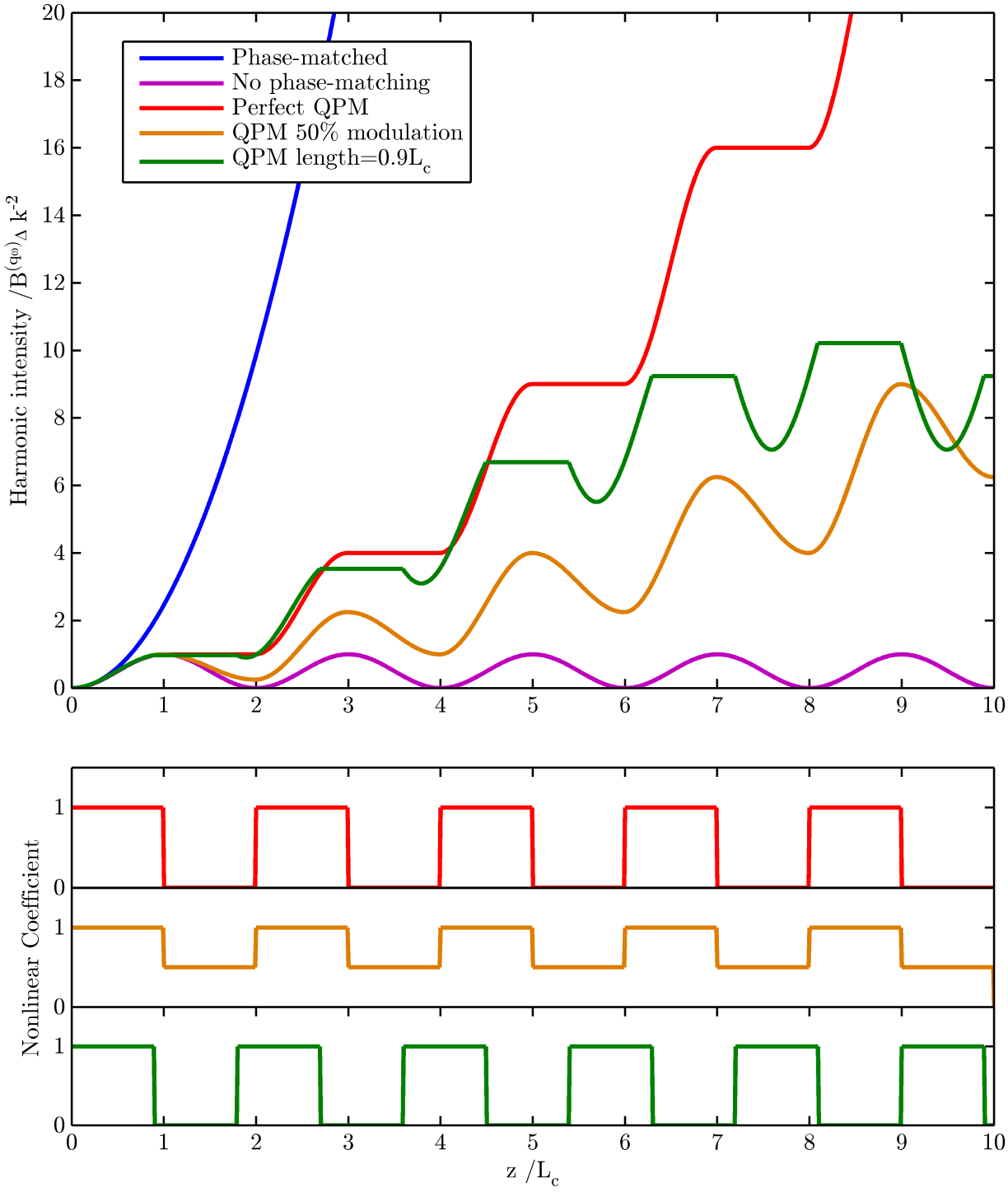

Figure 3.3: Harmonic intensity as a function of distance through the generating medium for the case of perfect phase-matching, constant phase-mismatch, perfect QPM, QPM with only a 50% modulation of HHG and QPM where the modulation period does not quite match the coherence length.

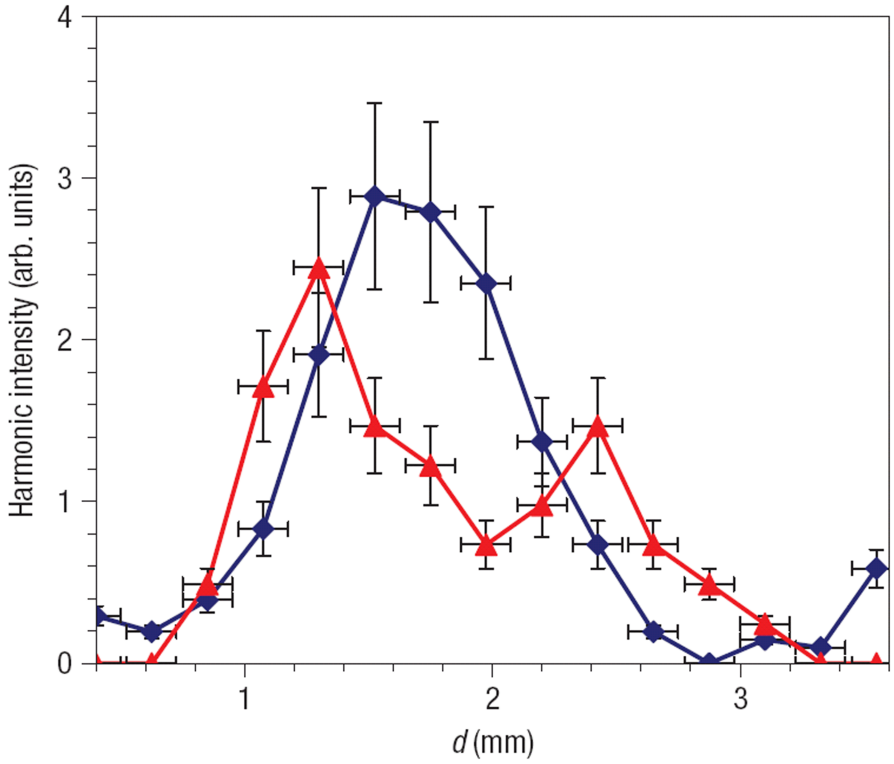

Figure 3.4: Variation of the harmonic yield with the separation d of two gas jets, at photon energies of 390 eV (diamonds) and 535 eV (triangles). Figure from [50].

with duration 15 fs and energy 2 mJ were focused with a confocal parameter of 18 mm onto two gas jets, each of width 0.4 mm. Figure 3.4 shows the measured harmonic intensity as the separation of the gas jets was varied, showing clearly that the harmonic light generated in the two sources interfered constructively and destructively depending on the gas jet separation. At an optimal separation of 1.7 mm the measured enhancement of the 235th harmonic was approximately a factor of two.

This technique is limited by the fact that an additional source is required for each coherent zone, making it difficult to scale-up to many coherence lengths. It would also be challenging to match shorter coherence lengths at higher harmonic orders, since this would require correspondingly narrow gas jets.

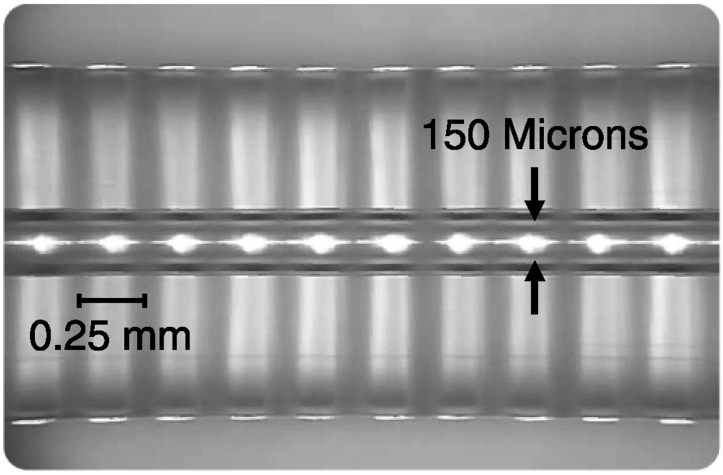

Figure 3.5: A glass capillary with a modulated inner diameter, made using precision glass-blowing techniques. Figure from [53].

3.3.2 Modulated Capillaries

Since HHG is so sensitive to the driving intensity, even small variations of this parameter can lead to significant changes in the XUV flux. This can be used to achieve QPM by inducing small modulations of the correct periodicity to the driving intensity. Christov et al. proposed[51] that this could be achieved by modulating the inner diameter of a hollow capillary. The gas pressure and laser intensity are then tuned to match the coherence length to the waveguide modulation period. This was experimentally realized a few years later[52, 53], by using precision gas-blowing techniques to create glass capillaries with sinusoidal modulations of the inner diameter.

Figure 3.5 shows a capillary with modulations of period 0.25 mm and a depth of approximately 10% of the capillary radius. Light from a 1 kHz Ti:sapphire laser system producing 22 fs pulses, with a pulse energy of 1 to 3 mJ, was focused into capillaries of length 25 mm, filled with argon gas. Figure 3.6 shows the measured harmonic spectrum for both a straight and modulated capillary. The modulated-diameter capillary is seen to increase the HHG

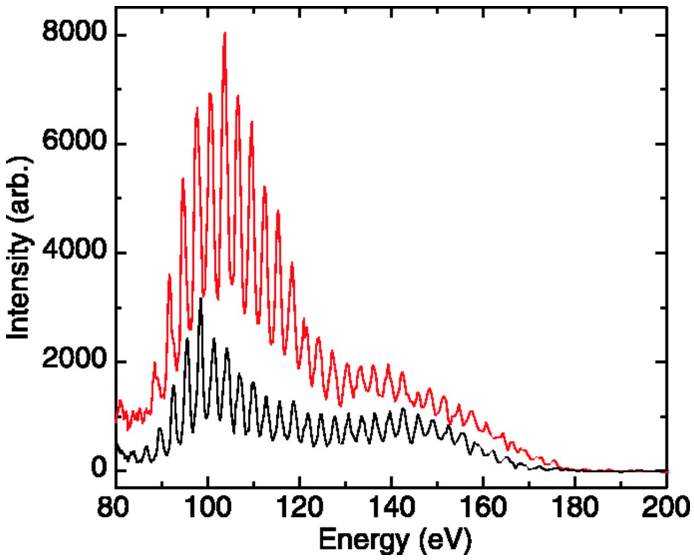

Figure 3.6: Measured harmonic spectra from a straight (black) and 0.25-mm-period modulated (red) waveguide filled with 7 torr Ar at a peak laser intensity of $9 \times 10^{14}\,\mathrm{Wcm}^{-2}$. Figure from [53].

flux over the recorded energy range, by up to a factor of three. Further, the measured cut-off frequency is seen to extend, suggesting that the highest observed harmonic orders are not limited by the $\lambda_{\mathrm{max}} = I_p + 3.17U_p$ relation in this case, but by ionization-induced phase-mismatch. For harmonics around 110 eV, where the enhancement is greatest, Equation (3.25) gives a phase-mismatch $\Delta k \approx 20000\,\mathrm{m}^{-1}$, which approximately matches the wavenumber of the oscillations in the waveguide, $k = 2\pi/\lambda_{\mathrm{mod}} = 25400\,\mathrm{m}^{-1}$. The authors attribute the enhancements seen at higher photon energies to higher-order QPM.

This technique is again limited by the minimum coherence lengths which can be matched, due to both the technical difficulties of creating modulated capillaries with periods less than a few hundred microns, as well as the fact that the period of the modulations must be long enough to allow the beam to diffract and reduce in intensity. A focused Gaussian beam with

spot size w_0 will diffract after propagating a distance z to a beam of radius w given by:

$$w(z) = w_0\sqrt{1+\left(\frac{z}{z_\mathrm{R}}\right)^2} \tag{3.28}$$

where $z_\mathrm{R} = \pi w_0^2/\lambda$ is the Rayleigh length. For the lowest-order mode in a capillary with $a = 75\,\mu$m, the spot-size will increase by only 0.01% over a distance of 0.125 mm, corresponding to the modulations in the capillary shown in Figure 3.5. If the modulation period is reduced further, the degree of diffraction may not be enough to reduce the intensity to a level where HHG is suppressed.

Another limitation is the driving intensity which may be used, since ablation can easily destroy the waveguide structure. Finally, guiding within these structured capillaries will not be as favourable as with straight capillaries, limiting the effective generation length.

3.3.3 Mode Beating

A similar mechanism for QPM of HHG is the use of mode beating within a capillary. In this approach the transverse profile of the input driving beam is modified such that it excites certain modes of a capillary waveguide. Beating between the modes causes the axial intensity of the guided laser pulses to be modulated strongly, with a period L_b set by the difference in wave-vectors of the modes. In practice, values of L_b as small as $100\,\mu$m may be achieved straightforwardly. The strong modulation of the driving intensity offers a further benefit: the degree of ionization in the regions between those of high intensity is low. This increases L_c significantly, making it possible to achieve QPM of higher-order harmonics than in modulated capillaries (where the intensity modulation is small). In the first experimental demonstration of this scheme[54], multimode QPM was found to increase the intensity of 300 eV-harmonics by three orders of magnitude. At these wavelengths approximately

10^9 photons per pulse per harmonic were generated, corresponding to a peak brightness of 10^{21} photons s^{-1} mm^{-2} $mrad^{-2}$ in 0.1% bandwidth, the brightest source of water-window harmonics observed to date.

3.4 Quasi-Phase-Matching with Counterpropagating Light

The final and possibly the most powerful method for achieving QPM of HHG is the use of relatively weak counterpropagating light, as proposed[55] by the group of Justin Peatross in 1997. It was found that this light could impose a microscopic standing amplitude and phase modulation on the driving field, where the fields overlap. Due to the extreme nonlinearity of the HHG process, any small modulation of the phase of the driving laser field induces a strong longitudinal phase variation in the individual high harmonics. This can lead to phase "scrambling" of the high harmonics over wavelength-scales, leading to much-reduced harmonic output. These phase variations can be generated with a counterpropagating light intensity as little as two orders of magnitude less than that of the driving pulse. QPM can then be achieved with a counterpropagating train of pulses, since harmonics will only be generated at points in the medium where the driving pulse does not overlap with one of the pulses in the train.

Let us develop these ideas more quantitatively. Consider driving and counterpropagating (CP) fields, both linearly polarised along the same axis and with the same frequency. Where the pulses overlap, the total electric field is given by:

$$E(z,t) = \mathrm{Re}[E_{\mathrm{driver}} e^{i(kz-\omega t)} + E_{\mathrm{CP}} e^{i(-kz-\omega t)}] = \mathrm{Re}[E_t(z) e^{i(kz-\omega t+\phi(z))}] \qquad (3.29)$$

where E_{driver} and E_{CP} are the amplitudes of the driver and counterpropagating electric fields respectively and

$$E_t(z) = E_{\text{driver}}\sqrt{1+\left(\frac{E_{\text{CP}}}{E_{\text{driver}}}\right)^2+2\frac{E_{\text{CP}}}{E_{\text{driver}}}\cos(2kz)} \tag{3.30}$$

$$\phi(z) = -\arctan\left(\frac{\frac{E_{\text{CP}}}{E_{\text{driver}}}\sin(2kz)}{1+\frac{E_{\text{CP}}}{E_{\text{driver}}}\cos(2kz)}\right) \tag{3.31}$$

A variation ϕ in the phase of the driver will induce a change $q\phi$ in the phase of the qth harmonic.

According to Equation (3.31), the peak-to-peak phase variation is

$$\Delta\phi = 2\arctan\frac{E_{\text{CP}}/E_{\text{driver}}}{\sqrt{1-(E_{\text{CP}}/E_{\text{driver}})^2}} \approx 2\frac{E_{\text{CP}}}{E_{\text{driver}}} \tag{3.32}$$

where the approximation is made that $E_{\text{CP}} \ll E_{\text{driver}}$. Harmonics of order q will be extinguished when this phase variation is of order π/q. This is achieved when:

$$\Delta\phi = \frac{\pi}{q} = 2\frac{E_{\text{CPP}}}{E_{\text{driver}}} \tag{3.33}$$

$$q = \frac{\pi}{2}\frac{E_{\text{driver}}}{E_{\text{CPP}}} = \frac{\pi}{2}\sqrt{\frac{I_{\text{driver}}}{I_{\text{CPP}}}} \tag{3.34}$$

For an intensity ratio $I_{\text{CPP}}/I_{\text{driver}} = 10^{-2}$, Equation (3.33) suggests that harmonics $q > 15$ will be suppressed by the counterpropagating field.

Equation (3.30) shows that there will also be a direct modulation of the intensity due to the counterpropagating light. This effect will generally be much less than the direct

phase effect, although it may still be significant for cut-off harmonics, which are particularly sensitive to the peak driving intensity. The intensity modulation will also induce a phase variation due to the intensity-dependence of the phase of high harmonics, as discussed in Section 2.2.6. This effect is also relatively small compared to the the direct phase modulation due to the counterpropagating field.

Up to now, a CW plane-wave has been assumed; the estimates presented here may well differ for the case of ultrafast driver pulses, where the intensity will vary considerably with space and time. The calculations above should be accurate for the cut-off harmonics, since these are only produced at the laser focus and at the peak of the pulse. The conditions under which the cut-off harmonics are produced will therefore not vary significantly, and if the overlap with the counterpropagating pulse (CPP) is at the focus, all such harmonics should be generated in a region and time where the CPP is present. However, the plateau harmonics will be generated over a range of intensities and therefore might be produced at locations and times where the overlap with the counterpropagating pulse is not optimal. In this case, the calculations above for the required counter-propagating intensity may be under-estimates.

Suppression of HHG is also possible by using a counterpropagating field which is linearly polarized in a plane perpendicular to that of the driving electric field. This produces an elliptical polarization in the overlap region, with the degree of ellipticity dependent on the ratio of the two fields. HHG is strongly dependent on the ellipticity of the driving field[30], which may be understood in terms of the quasiclassical three-step model. For an elliptically polarized electric field the trajectories of the electrons after ionization will in general not return to the parent ion. Recombination and harmonic generation is therefore suppressed.

In 2006 we performed an experiment to quantify and compare the suppression effect on

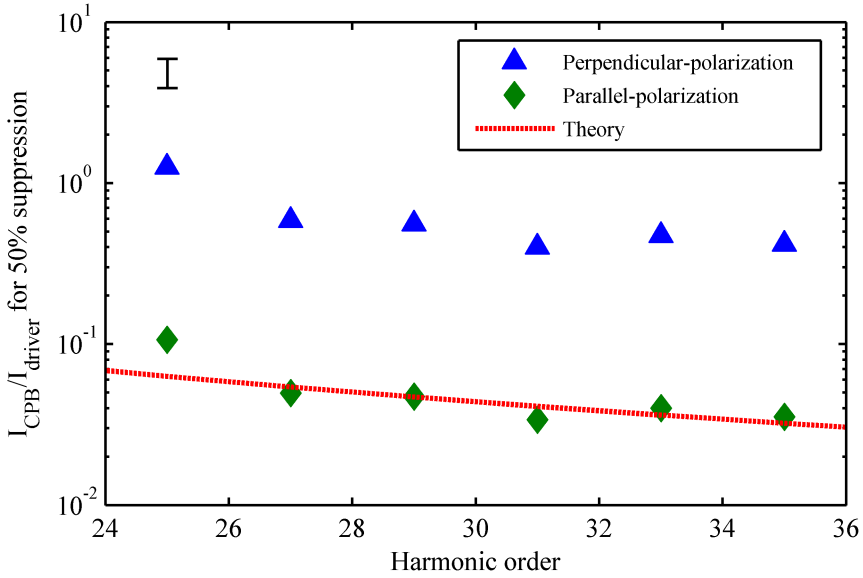

Figure 3.7: Measured intensity ratios in the driver and CP beams for 50% suppression of each harmonic order, for the case of parallel and perpendicular polarisation of the beams. A typical error bar for the data is shown. Theory for the direct-phase effect with parallel polarisations, calculated from Equation (3.33), is also plotted.

HHG by counterpropagating pulses with polarisations parallel and perpendicular to that of the driving pulse[56]. Harmonics were generated in a gas cell containing 80 mbar argon, using 280 fs, 8 mJ pulses (peak intensity $2.5 \times 10^{15}\,\mathrm{Wcm^{-2}}$) from a Ti:Sapphire CPA system. The driving pulses were overlapped with individual 4 ps counterpropagating pulses which had intensities of up to $4 \times 10^{13}\,\mathrm{Wcm^{-2}}$. The HHG spectrum was recorded as a function of the point of overlap of the driving laser pulse and the CPP (henceforth known as a "scan"), for a range of CPP energies and both parallel and perpendicular-polarisations. The scans exhibited one extinction region, corresponding to HHG occurring over two coherence lengths in the medium. Figure 3.7 shows the measured value of $I_{\mathrm{CPP}}/I_{\mathrm{driver}}$ needed to reduce the harmonic signal by 50%, for a range of harmonic orders. It can be seen that the CPP intensity required to suppress harmonic generation with a perpendicularly-polarized beam is approximately ten times greater than that with a parallel-polarized beam. The intensity

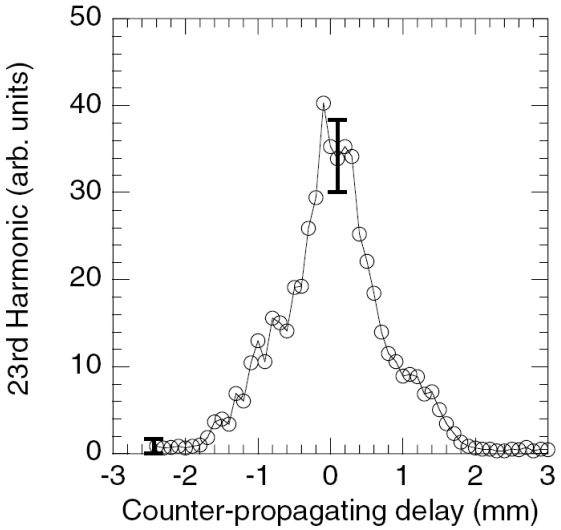

Figure 3.8: Measured intensity of the 23rd harmonic as a function of overlap position with a counterpropagating pulse of effective length 0.3 mm. Figure from [57].

ratio calculated from Equation (3.33) is also plotted, showing good agreement with the experimental data, suggesting that it was indeed the direct phase modulation effect which caused the suppression.

3.4.1 Previous Demonstrations of QPM with Counterpropagating Light

The Peatross group at Brigham Young University have used parallel-polarised counterpropagating light to control and enhance HHG[57]. High harmonics were generated in a free-focus geometry from a gas jet. The counterpropagating pulse, of length 0.3 mm was scanned through the generation region, of length 1 mm. Figure 3.8 shows the intensity of the 23rd harmonic as a function of the delay between the driver and counter-propagating pulses. A delay of zero corresponds to overlap in the centre of the gas jet. An enhancement of the 23rd harmonic was seen when the overlap was at the centre of the generation region. Peatross

attributed this enhancement to suppression of HHG in the centre coherence length, allowing constructive interference of HHG in the first and third coherence lengths.

The next logical step was to employ multiple counterpropgating pulses in order to quasi-phase-match over multiple coherence lengths within a medium. This has been achieved with some success by the group led by Maragret Murnane and Henry Kapteyn at JILA, University of Colorado at Boulder[58, 59, 60, 61, 62], who undertook experiments in gas-filled capillary waveguides. Pulse trains of up to three counterpropagating pulses were generated by placing pieces of glass in the pulse compressor, thereby delaying different frequency components of the laser spectrum and generating a sequence of pulses.

Initially, Lytle et al. used single pulses to characterise HHG in their capillary[60]. The point of collision of a single counterpropagating pulse with the driver pulse was scanned through the medium by adjusting a delay line, leading to oscillations in the harmonic intensity as zones contributing constructively and destructively to the harmonic wave were consecutively suppressed. This is shown in Figure 3.9, where harmonic light was generated in a 3.5 cm-long waveguide filled with 5 torr argon. The driving pulse had an energy of 0.52 mJ and duration 25 fs, while the single counterpropagating pulse had an energy and duration of 0.2 mJ and 1.6 ps, respectively. The periodicity of these modulations was expected to be $2L_c$, allowing the local coherence length of the process to be measured directly. It can be seen that coherence is maintained over more than 20 coherence lengths (≈ 10 mm) and that L_c is approximately constant through the waveguide, although it increases towards the exit of the capillary where the gas pressure decreases and the driving pulse energy is depleted.

Once L_c was known, suitable pulse trains were used to achieve QPM. "Enhancement factors" for harmonics around 70 eV of up to 300 were observed when using a train of three

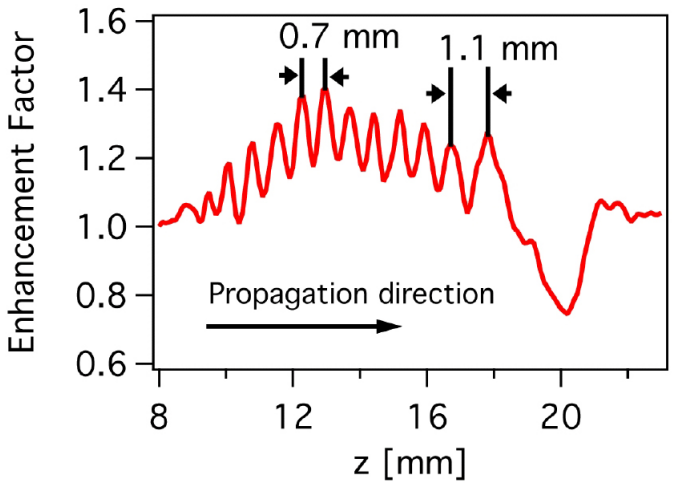

Figure 3.9: Coherent oscillations of harmonic intensity as a counter-propagating pulse is scanned through a waveguide. Figure from [59].

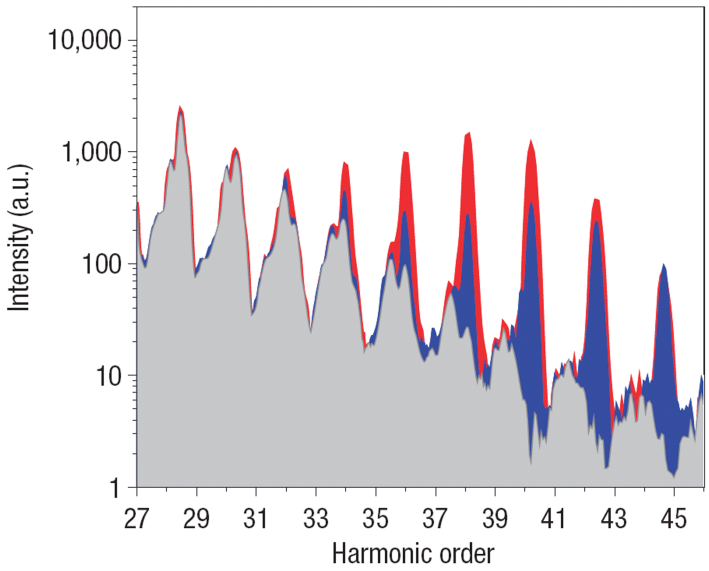

Figure 3.10: Observed HHG emission for zero, one and two counterpropagating pulses. Figure from [59]

pulses in a 6 cm-long capillary filled with 7 torr Ar[59]. Figure 3.10 shows the harmonic spectrum for the case of one, two and three counterpropagating pulses, measured by Zhang et al. The enhancement beyond the expected factor of nine was explained by suggesting that the phase of the harmonics in the out-of-phase regions was shifted by more than π, transforming them into constructive zones, or by the fact that the harmonics in the last coherence length may have been weaker than those generated further into the capillary. However, despite applying all-optical QPM over multiple coherence lengths for the first time, these results did not extend harmonic intensities beyond those which could be achieved with conventional phase-matching.

More recently the Boulder group has demonstrated QPM at ionization levels and harmonic energies where pressure-tuned phase-matching would *not* otherwise be possible. Selective enhancement, by factors of up to 150 in the flux of harmonics at photon energies around 140 eV were achieved[62] using a train of two counterpropagating pulses in 110 Torr He, which required the matching of coherence lengths as small as 0.2 mm.

Figure 3.11 shows the spectrum obtained with up to two counterpropagating pulses present, as well as that obtained under similar driving laser parameters, but at a pressure of 500 Torr, which is optimal for conventional phase matching of harmonics up to $q = 77$. It can be seen that the intensity of harmonics $q > 87$ is two orders of magnitude greater than that which can be achieved with conventional phase matching.

In summary, significant progress has been made with all-optical QPM using counterpropagating pulse trains, although only three counterpropagating pulses have been employed to date. Figure 3.9 suggests that QPM over many more coherence lengths should be possible. To achieve this, new techniques for pulse train generation are required which allow more pulses to be generated. These techniques should also be more flexible and allow shorter

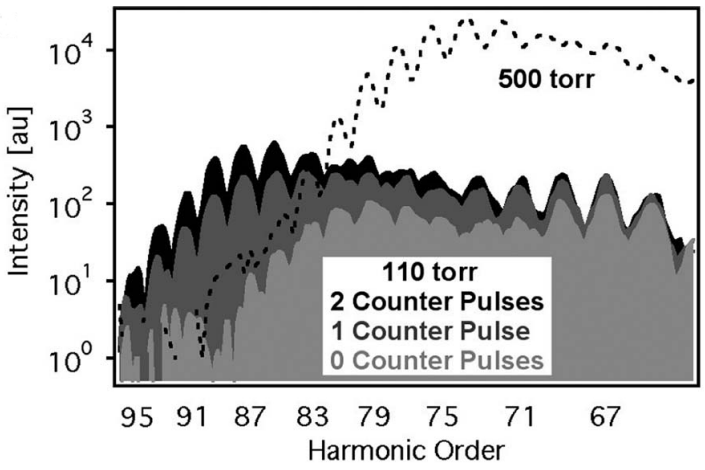

Figure 3.11: Observed harmonic emission from 110 torr helium for zero, one and two counterpropagating pulses. The dotted curve shows harmonic emission under similar laser conditions, but at a pressure of 500 torr, which is optimal for conventionally phase-matching lower harmonic orders, below q = 77. Figure from [62].

coherence lengths to be matched.

3.5 Conclusion

In this chapter I have introduced the concept of phase-mismatch as a major limiting factor to the efficiency of HHG. The various sources of dispersion when generating high-harmonics in a gas-filled capillary waveguide have been explained and quantified and the concept of pressure-tuned phase-matching has been described. Finally, quasi-phase-matching has been introduced and its previous experimental realizations have been outlined, including the method with which this thesis is concerned: all-optical QPM with a counter-propagating train of pulses. The experimental implementation of this technique is described in Chapter 6.

Chapter 4

High-Harmonic Generation in Capillary Waveguides

The telecommunications revolution has been driven by the development of waveguides which allow the transmission of high-frequency electromagnetic radiation over large distances. In the optical domain, fiber optics have allowed high-bandwidth communication over thousands of kilometers. In these cylindrical waveguides there are two distinct regions; the "core" of refractive index η_{i} and the "cladding" of refractive index η_{o}. For $\eta_{\mathrm{i}} > \eta_{\mathrm{o}}$, total internal reflection occurs at the core-cladding boundary, leading to lossless mode propagation.

For the case of HHG, guiding of the high-intensity driving radiation over extended distances can lead to enhanced emission, due to the greater interaction length. The "core" of the waveguide is then the low-density gas medium and the cladding is generally glass, giving $\eta_{\mathrm{i}} < \eta_{\mathrm{o}}$, so the guided light cannot be totally internally reflected. However, if the wavelength of the guided light is much smaller than the diameter of the inner bore, it will be guided through glancing-incidence reflection from the core-cladding boundary, although the modes will now be lossy.

For all of the HHG data presented in this thesis, hollow glass waveguides were used. This geometry has a number of advantages over a free-focus gas jet or gas cell setup:

1. Extension of generation length. Although the guided modes of a hollow waveguide are lossy, they can still maintain a high intensity over several Rayleigh lengths. The guiding process counteracts the effect of ionization defocusing and diffraction.

2. Phase-matching. As seen in Section 3.1, the dispersion of the waveguide can be balanced against that of the partially-ionised plasma, allowing pressure-tuned phase-matching.

3. Quasi-phase-matching. QPM techniques are possible using either a waveguide with a modulated inner diameter or by manipulating the excited modes of the waveguide in order to match the longitudinal intensity distribution to the local coherence length, as will be described below.

4. Gas Management. XUV light is strongly absorbed by a gas medium, so it is important to confine the gas to the region of high driver intensity and have low density elsewhere to allow propagation of the harmonic light. This can be achieved in a capillary waveguide by filling the inner bore with the gas medium.

A waveguide will support certain discrete modes, which depend on the properties of the capillary and the wavelength of the light. The modes that are excited and their relative amplitudes depend on the spatial distribution of the incident radiation. Since HHG is so sensitive to the driving intensity, the propagation of these modes is an important aspect of the generation process.

4.1 Waveguide Modes

The modes of a step-index waveguide can be found by solving Maxwell's wave equation with the appropriate boundary conditions at the core-cladding interface. The waveguide's inner bore radius, a is assumed to be much larger than the wavelength of the light and the capillary cladding is assumed to be infinitely thick. This analysis may be found in a number of sources[63, 64] but the main results are summarised below.

In general, there are three main types of mode which are supported by a hollow, step-index waveguide. These are:

- Circular Electric Modes, $TE_{j,m}$. The electric field is purely azimuthal. The magnetic field has radial and longitudinal components, although the amplitude of the longitudinal component is smaller by a factor of order λ_0/a.
- Circular Magnetic Modes, $TM_{j,m}$. The magnetic field is purely azimuthal. The electric field has radial and longitudinal components, although the longitudinal component is smaller by a factor of order λ_0/a.
- Hybrid Modes, $EH_{j,m}$. All field components are present. The radial magnetic and electric fields are larger by a factor $1/\lambda_0$ than the corresponding longitudinal fields.

A linearly polarised, TEM_{00} Gaussian beam is most closely matched to the linearly-polarised $EH_{1,m}$ modes of a hollow waveguide, hence these are the ones which are excited. Other combinations of modes which produce linearly-polarised fields are possible, although they attenuate more rapidly with propagation through the waveguide.

Inside the waveguide, the radial amplitude of the field is given by:

$$E_{1,m}(r) = \sqrt{\frac{\mu_0}{\epsilon_0}} H_{1,m} = J_0\left(u_{1,m}\frac{r}{a}\right) \tag{4.1}$$

where J_0 is the Bessel function of the 0th kind and $u_{1,m}$ is the mth root of the equation $J_0(x) = 0$ and r is the radial coordinate. The propagation constant for these modes is given by

$$k_{1,m} = \beta_{1,m} + i\alpha_{1,m} \tag{4.2}$$

where

$$\beta_{1,m} = \frac{2\pi}{\lambda}\left[1 - \frac{1}{2}\left(\frac{u_{1,m}\lambda}{2\pi a}\right)^2\right] \tag{4.3}$$

is the phase constant expressing the dispersion of the modes, and

$$\alpha_{1,m} = \left(\frac{u_{1,m}}{2\pi}\right)^2 \frac{\lambda^2}{a^3}\left(\frac{n_o^2 + 1}{2\sqrt{n_o^2 - 1}}\right) \tag{4.4}$$

is the attenuation constant, giving the inverse scale length of the attenuation due to reflection losses. The loss-length (the distance over which the amplitude of the mode is reduced by a factor $1/e$) becomes shorter for higher orders, so the waveguide acts as a "spatial filter", suppressing the higher order modes relative to $EH_{1,1}$.

4.2 Waveguide Coupling

The coupling of the incident laser beam into a hollow waveguide can be described by the projection of the incident beam profile onto the waveguide modes described above, since these form a basis of orthogonal functions over the space of possible fields at the waveguide entrance.

For a linearly-polarised beam, the incident field distribution E_{input} can be expressed as a sum over the $EH_{1,m}$ modes:

$$E_{\text{input}}(r) = \sum_{m=1}^{\infty} C_m E_{1,m}(r) \tag{4.5}$$

where C_m is the coupling coefficient for the mth mode. The coupling coefficient gives the amplitude by which a normalised mode, $\tilde{E}_{1,m}(r)$ is excited:

$$C_m = \int \tilde{E}_{1,m}(r) \cdot E^*_{\text{input}}(r)\, 2\pi\, r\, \mathrm{d}r \tag{4.6}$$

where cylindrical symmetry is assumed. For an incident beam with a Gaussian intensity profile, $E_{\text{input}}(r) = E_0 \exp\left[-r^2/w_0^2\right]$, in which case

$$C_m = \frac{2\sqrt{\pi}}{aJ_1(u_{1,m})} \int_0^a J_m\left(u_{1,m}\frac{r}{a}\right) E_0 \exp\left[-r^2/w_0^2\right] r\, \mathrm{d}r \tag{4.7}$$

The fraction of the input power coupled into the mth mode is given by C_m^2/P, where $P = \int |E_{\text{input}}(r,\theta)|^2\, 2\pi\, r\, dr$.

Figure 4.1 shows C_m^2/P as a function of the ratio of the radii of the incident spot and waveguide, w_0/a. It can be seen that optimum coupling into the $EH_{1,1}$ mode is achieved when

$$w_0 = 0.6435a \tag{4.8}$$

which results in 98% of the incident power being coupled into the lowest-order EH mode. As the spot-size deviates from this condition, more power is coupled into the lossier, higher-order modes.

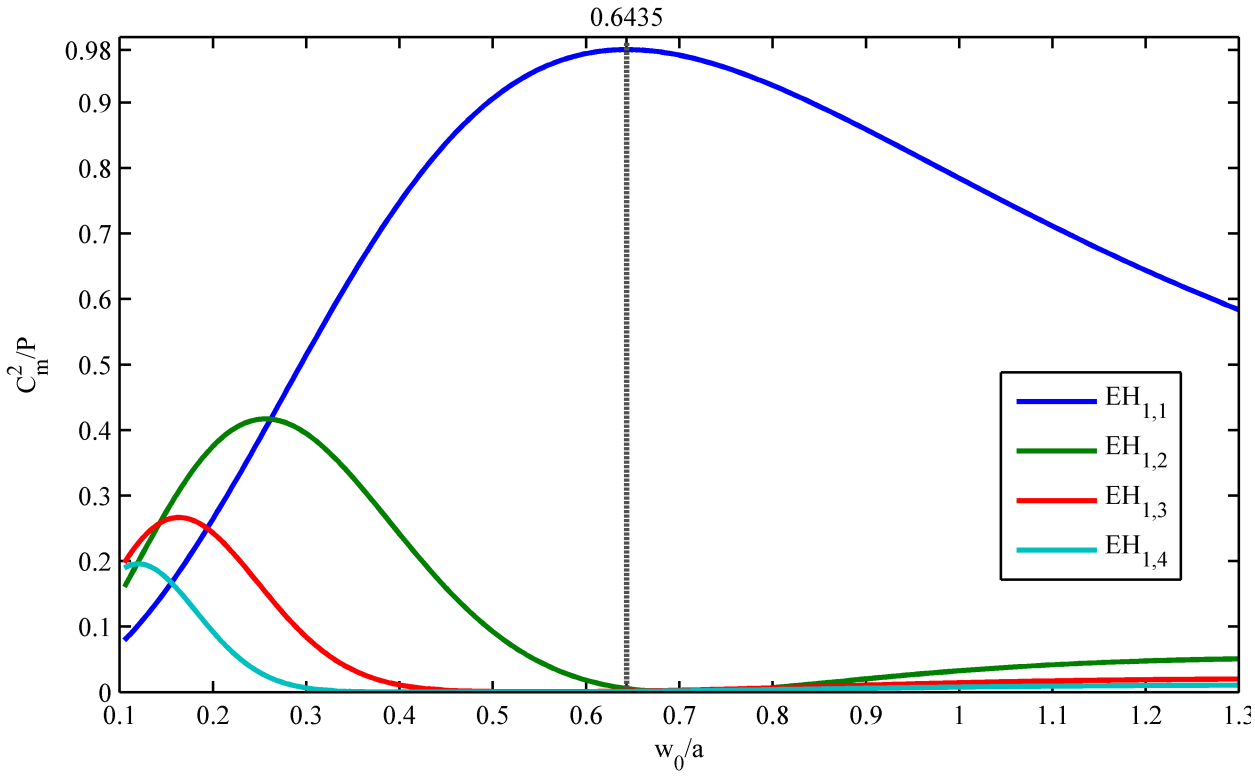

Figure 4.1: Proportion of the incident power coupled into the first four modes, as a function of w_0/a, the ratio of the incident spot radius to the capillary inner bore radius. Waveguide attenuation increases for higher-order modes, so the transmission of a capillary is maximised when the lowest-order mode is preferentially excited. Maximum coupling into the lowest-order mode occurs when $w_0/a = 0.6435$.

4.3 Mode Beating

Multiple modes may be excited in a waveguide either through the coupling described above, or due to laser-plasma interactions within the waveguide. From Equation (4.2) we see that the propagation constant and therefore the phase velocity is different for each mode. The modes therefore interfere, leading to an intensity variation or "beating" with propagation distance. This results in an intensity,

$$I(z,r) = \frac{\epsilon_0 c}{2}\left|\sum_m A_m(r)\exp\left(ik_{1,m}z\right)\right|^2 \tag{4.9}$$

where the factors $A_m(r)$ represent the excited modes and are given by the product of the C_m values by the normalised mode:

$$A_m(r) = C_m \frac{J_0(u_{1,m}r/a)}{a\sqrt{\pi}J_1(u_{1,m})} \tag{4.10}$$

Figure 4.2 shows the longitudinal intensity distribution at a wavelength of 800 nm for the case of perfect matching to a capillary with radius 51 μm, as well as for slight mismatch. The ten lowest-order modes are considered. Even for the case of ideal matching ($w_0 = 0.6435a$), where 98% of the power goes into the lowest-order mode, it is clear that the intensity is significantly modulated along the capillary. Clearly obervable are oscillations due to the interference between the two lowest-order modes, $EH_{1,1}$ and $EH_{1,2}$, with a periodicity given by:

$$\lambda = \frac{2\pi}{\Delta k} = \frac{2\pi}{\beta_{1,1} - \beta_{1,2}} = 10.4\,\text{mm} \tag{4.11}$$

It is seen that even small deviations from the ideal coupling condition cause even greater intensity fluctuations as the power coupled into higher-order modes increases. For $w_0 = 0.7a$

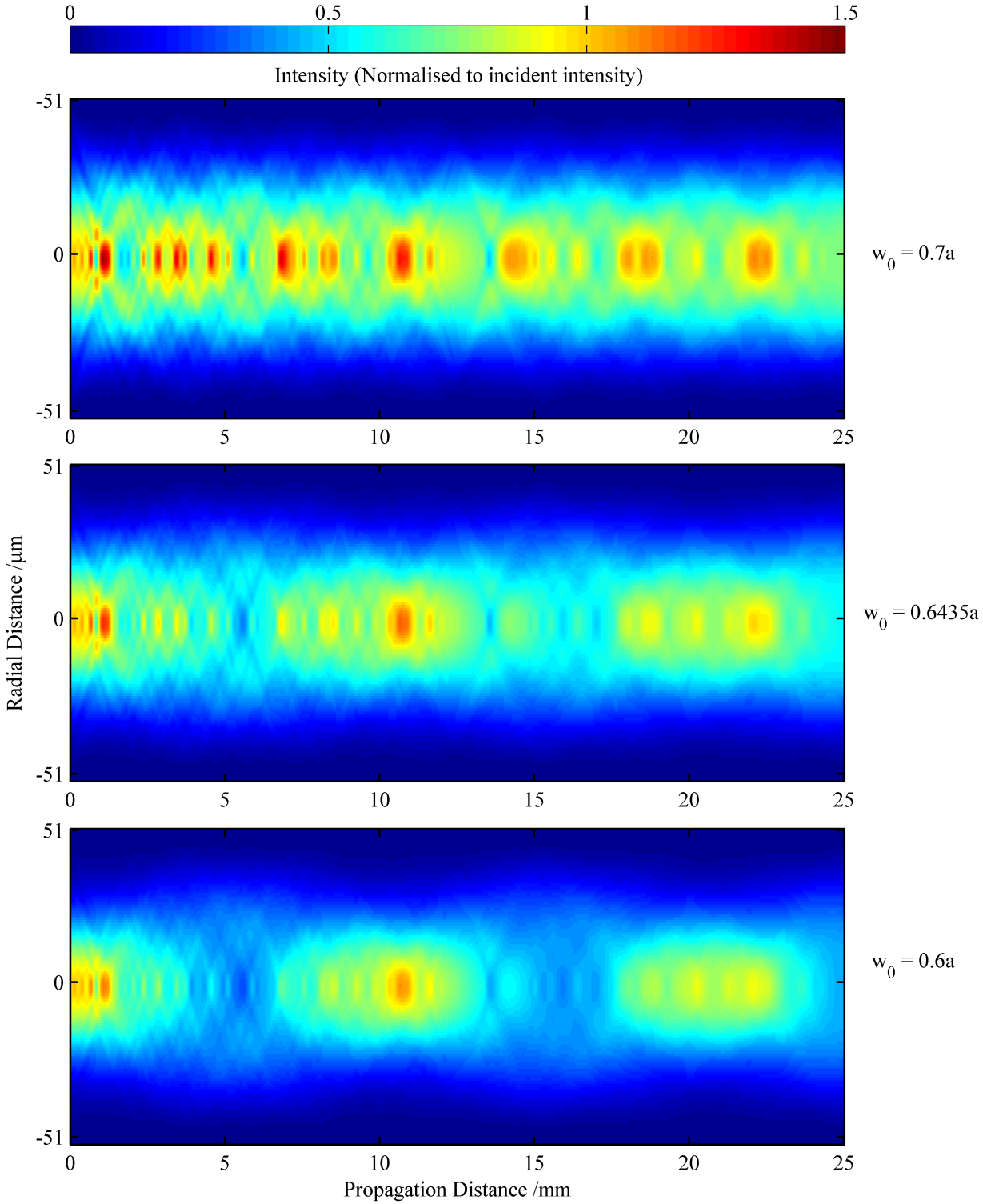

Figure 4.2: Calculated intensity as a function of radial position and propagation distance for three different coupling conditions, for a capillary with $a = 51\,\mu$m. Normalised to the incident intensity.

Table 4.1: Attenuation length, group velocity and distance for mode separation for a 50 fs duration, 800 nm pulse, for the first five modes propagating in a waveguide with an inner diameter of 51 μm and refractive index $\eta_o = 1.45$.

Mode	$1/e^2$ Intensity attenuation length	Group velocity	Distance for 50 fs separation from $EH_{1,1}$
$EH_{1,1}$	96 cm	0.99998 c	-
$EH_{1,2}$	18 cm	0.99990 c	19.5 cm
$EH_{1,3}$	7.4 cm	0.99977 c	7.0 cm
$EH_{1,4}$	4.0 cm	0.99957 c	3.6 cm
$EH_{1,5}$	2.5 cm	0.99931 c	2.2 cm

a significant amount of energy is coupled into the $EH_{1,3}$ mode and intensity fluctuations of period 3.7 mm are observed corresponding to this mode interfering with the $EH_{1,1}$ mode.

I have so far assumed a CW-field. In practise, ultrashort pulses on the order of 50 fs are typically used for HHG in capillaries. These pulses have a limited longitudinal extent ($\approx 15\,\mu$m) which is generally much shorter than the waveguide (≈ 20 mm). Since the different modes have different group velocities, they will slip longitudinally relative to one another and after a certain propagation distance will no longer overlap. From Equation (4.2), the group velocity of the mth mode is:

$$v_{g,m} = \left(\frac{\partial \beta_{1,m}}{\partial \omega}\right)^{-1} = c\left[1 + \frac{1}{2}\left(\frac{u_{1,m}\lambda}{2\pi a}\right)^2\right]^{-1} \tag{4.12}$$

Once the separation of the modes is greater than their longitudinal spatial extent, the mode-beating will disappear. Table 4.3 shows the $1/e^2$ intensity attenuation length for the first four modes, the group velocity and the distance over which they become separated from the $EH_{1,1}$ mode by 50 fs.

We can simulate the effect of finite pulse duration by modifying Equation (4.3) to include

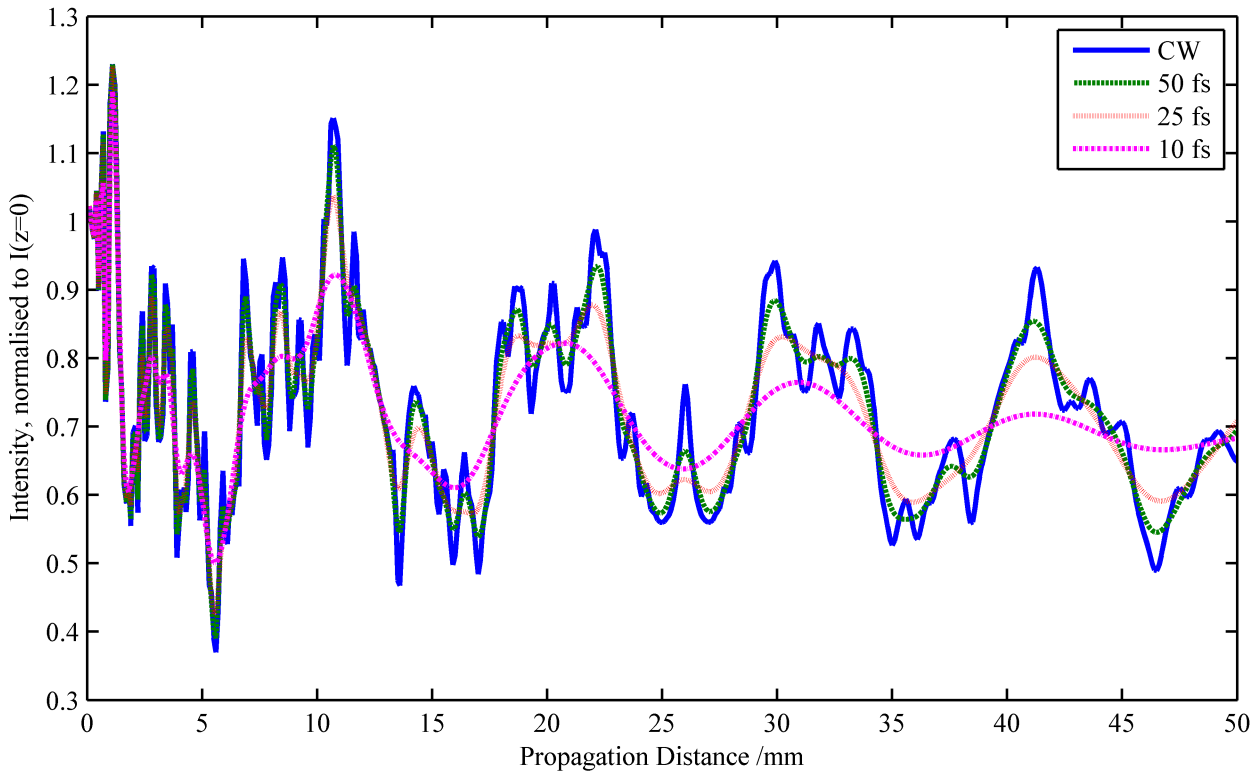

Figure 4.3: Longitudinal intensity variation in a capillary with $w_0 = 0.6345a$, due to beating between the ten lowest order modes, for the case of three different pulse durations as well as the CW case. From Equation (4.3).

a Gaussian temporal profile:

$$I(z,r,t) = \frac{\epsilon_0 c}{2}\left|\sum_p A_p(r)\exp\left(ik_{1,m}z\right)\exp\left(-2\ln 2\frac{(t-z/v_{\mathrm{g},m})^2}{\tau^2}\right)\right|^2, \qquad (4.13)$$

This is only a first-order approximation which does not take account of group velocity dispersion or other higher-order dispersion. Figure 4.3 shows $I(z, r = 0, t = z/v_{\mathrm{g},1})$, i.e. the on-axis intensity at a time corresponding to the peak of the fundamental mode. The first ten modes are included and pulse durations of 10, 25 and 50 fs, as well as the CW case, are shown.

It can be seen that as the pulse duration is decreased, the higher-order beating disappears,

as the higher-order modes lag behind those of lower-order and consequently no longer overlap with them.

4.4 The Effect of Mode Beating on the Propagation of Harmonics

The intensity and phase of the radiation produced by HHG is very sensitive to the driving intensity, as discussed in Chapter 2. We have seen that in capillary waveguides the intensity can fluctuate due to interference between modes. If this mode beating is tailored to the generation conditions, it can be used as a QPM mechanism, by suppressing HHG in regions where the locally-generated harmonic light is out of phase with the harmonic wave. However, the intensity fluctuations of the driving field could also lead to fluctuations in the phase and intensity of the *generated* harmonic radiation, as well as changes in the local coherence length, which could make QPM diffcult to achieve. Quasi-phase-matching techniques require that harmonic emission from consecutive coherence lengths is in-phase, so mode-beating may limit these methods.

I investigate here the effect of mode beating on the HHG process and the consequences for QPM schemes. This is achieved by modelling the propagation of both the driving laser pulse and the generated harmonic pulse in an ionising gas medium contained by a capillary waveguide.

A first-order propagation equation has been developed to describe the propagation of high-intensity pulses in underdense ($\omega_p \ll \omega_0$) media[65, 66], using the scalar wave equation in combination with a semiclassical model for the polarisation response of a field-ionising

medium. This scheme is suitable for the near plane-wave propagation of guided light in a capillary waveguide. In one space dimension, the following propagation equation for the driving field is obtained (in atomic units):

$$\partial_\xi E_\mathrm{l}(\xi,\tau) = -\frac{1}{2c}\int_{-\infty}^{\tau} \omega_p^2(\xi,\tau')E_\mathrm{l}(\xi,\tau')d\tau' - \frac{2\pi I_p}{c}\frac{\partial_\tau n(\xi,\tau)}{E_\mathrm{l}(\xi,\tau)} \tag{4.14}$$

where the moving coordinate frame $\xi = z$ and $\tau = t - z/c$ has been introduced. The driving laser field propagates in the z-direction and is polarised along x. The first spatial and time derivatives are denoted by ∂_ξ and ∂_τ respectively and I_p is the atomic ionization potential. For an initial atomic density n_0, the free elctron density $n(\xi,\tau)$ is determined by

$$n(\xi,\tau) = n_0\left[1 - \exp\left(-\int_{-\infty}^{\tau} d\tau' W(E_l(\xi,\tau'))\right)\right] \tag{4.15}$$

where $W(E_\mathrm{l})$ is the ionization rate given by the ADK expression given in Section 2.2.1. The plasma frequency ω_p, in atomic units is given by:

$$\omega_\mathrm{p}(\xi,\tau) = \sqrt{4\pi n(\xi,\tau)}. \tag{4.16}$$

The first term on the right hand side of Equation (4.14) corresponds to dispersion due to free electrons, while the second term represents energy loss due to ionization. The propagation of the high harmonic radiation is governed by:

$$\partial_\xi E_h(\xi,\tau) = -\frac{2\pi}{c}\partial_\tau D[E_l(\xi,\tau)] - \frac{\alpha}{2}E_h(\xi,\tau) \tag{4.17}$$

where E_h is the electric field of the HHG radiation, α is its absorption length and $D = n_0\langle x\rangle$, where the atomic dipole moment for HHG, $\langle x\rangle$ is obtained from the Lewenstein model

described in Chapter 2.

This set of equations was solved using an explicit finite-difference scheme, coded in Matlab®. For each spatial step, the driving electric field $E_{\rm l}(\xi,\tau)$ was used to calculate the electron density $n(\xi,\tau)$ as a function of time, using the ADK ionisation rates. The finite difference form of Equation 4.14 was then used to find $E_{\rm l}(\xi = z + \Delta z, \tau)$ from $E_{\rm l}(\xi = z, \tau)$ and since the initial driving electric field $E_{\rm l}(\xi = 0, \tau)$ was known, the electric field was found for all ξ. For each value of ξ the calculated electric field $E_{\rm l}(\xi,\tau)$ was used to calculate $D[E_l(\xi,\tau)]$, using the Lewenstein model. This was then used to calculate the harmonic electric field $E_{\rm h}(\xi,\tau)$, from which the harmonic spectrum was calculated. Typical simulation times were approximately 3 hours per millimeter of propagation, using a quad-core 3 GHz processor.

The laser parameters used in these simulations were $\lambda_0 = 800\,\text{nm}$, $\tau_p = 60\,\text{fs}$ and $I_{\rm peak} = 5 \times 10^{14}\,\text{Wcm}^{-2}$ and the generating medium was argon gas at a pressure of 30 mbar. Figure 4.4 shows part of the calculated intensity spectrum of the harmonic light as a function of propagation distance. Oscillations of the harmonic intensity with propagation distance are observed for each harmonic order, corresponding to phase mismatch between the harmonic light generated at different longitudinal points in the gas. The coherence length is seen to decrease with increasing harmonic order, as expected.

The upper plot in Figure 4.5 shows the peak intensity of the driving pulse as it propagates through the gas. The intensity is seen to drop due to temporal broadening of the pulse and energy loss from ionisation. The lower plot shows the intensity of the 79th harmonic through the medium, which oscillates due to phase mismatch. The amplitude of the oscillations decreases with distance, since the driver intensity drops below the level required to generate this harmonic. If QPM is now implemented and harmonic generation is switched off in

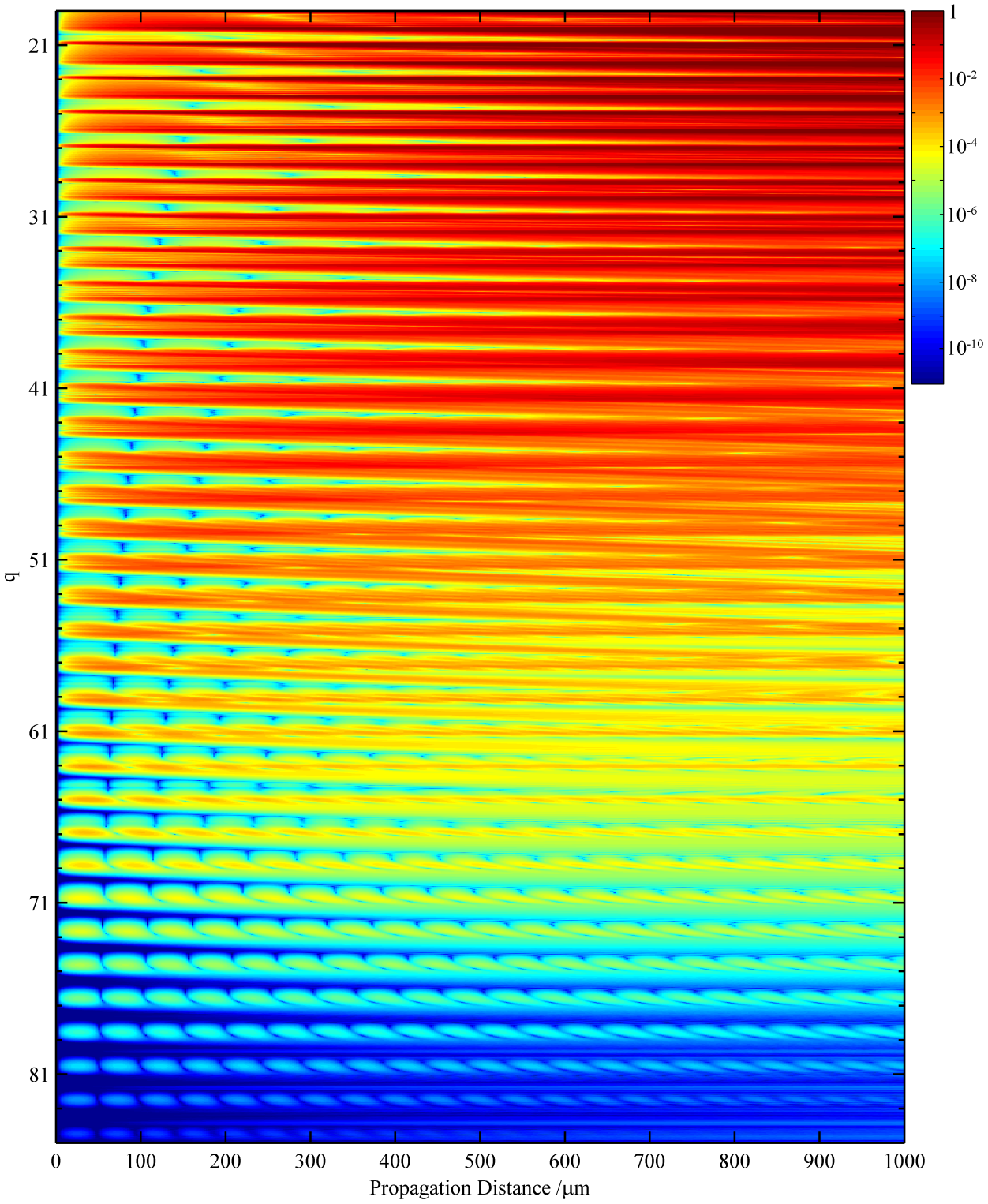

Figure 4.4: The intensity spectrum of the harmonic light generated using a driving pulse with $\lambda_0 = 800\,\text{nm}$, $\tau_p = 60\,\text{fs}$ and $I_{\text{peak}} = 5 \times 10^{14}\,\text{Wcm}^{-2}$ as a function of propagation distance.

the regions where the generated light interferes destructively with the harmonic wave, it is seen that the intensity of the 79th harmonic increases approximately quadratically with propagation distance, as predicted in Section 3.1.

4.4.1 The Effect of Mode Beating on QPM

In order to simulate the effect of mode-beating, the intensity of the driving laser with propagation distance is now modified. The variation in longitudinal intensity at the peak of a driving pulse with $\tau_p = 50\,\text{fs}$ is calculated from Equation (4.3), for coupling into a $51\,\mu$m-radius capillary where the spot size has been chosen to maximise excitation of the lowest-order mode ($w_0 = 0.6435a$). The resulting variation of peak driver intensity through the medium, used to calculate the harmonic emission, is shown at the top of Figure 4.6. The calculated intensity of the 79th harmonic is shown in the lower plot, with the same intensity scale as Figure 4.5. Note that the driving intensity used here is that at the time corresponding to the peak of the lowest order waveguide mode and that this approximation will only be accurate if this mode dominates.

The regular oscillations of the harmonic intensity are no longer evident, due to the strong variations of driver intensity. Generation of the 79th harmonic is confined to regions where the intensity is high enough to produce it. The driving intensity is in fact greater than the input intensity in some regions, leading to sharp jumps in the harmonic intensity.

The variation of the coherence length within the capillary means that quasi-phase-matching by periodic modulation of harmonic generation is now very difficult to achieve. Figure 4.6 also shows the calculated harmonic intensity if the same QPM scheme as in Figure 4.5 were applied, i.e. HHG is switched off for the "out-of-phase" zones determined in the absence of mode-beating. As expected, strong enhancement is no longer seen, since the QPM period

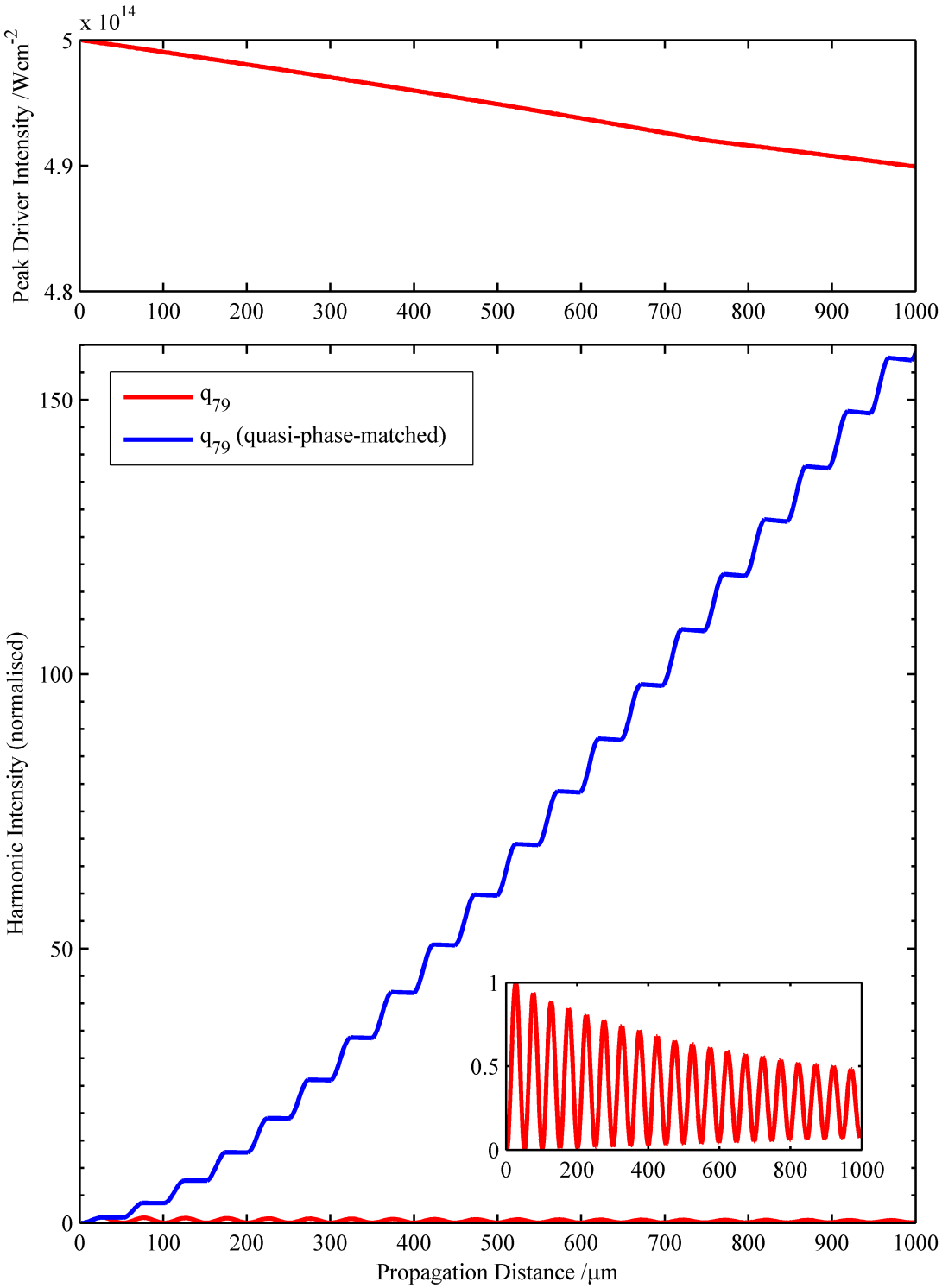

Figure 4.5: Calculated intensity of the driving pulse ($\lambda_0 = 800\,\text{nm}$, $\tau_p = 60\,\text{fs}$ and $I_{\text{peak}} = 5 \times 10^{14}\,\text{Wcm}^{-2}$, upper plot) and the 79th harmonic generated in 30 mbar argon, as a function of propagation distance, with and without (enlarged in inset plot) perfect quasi-phase-matching applied (lower plot).

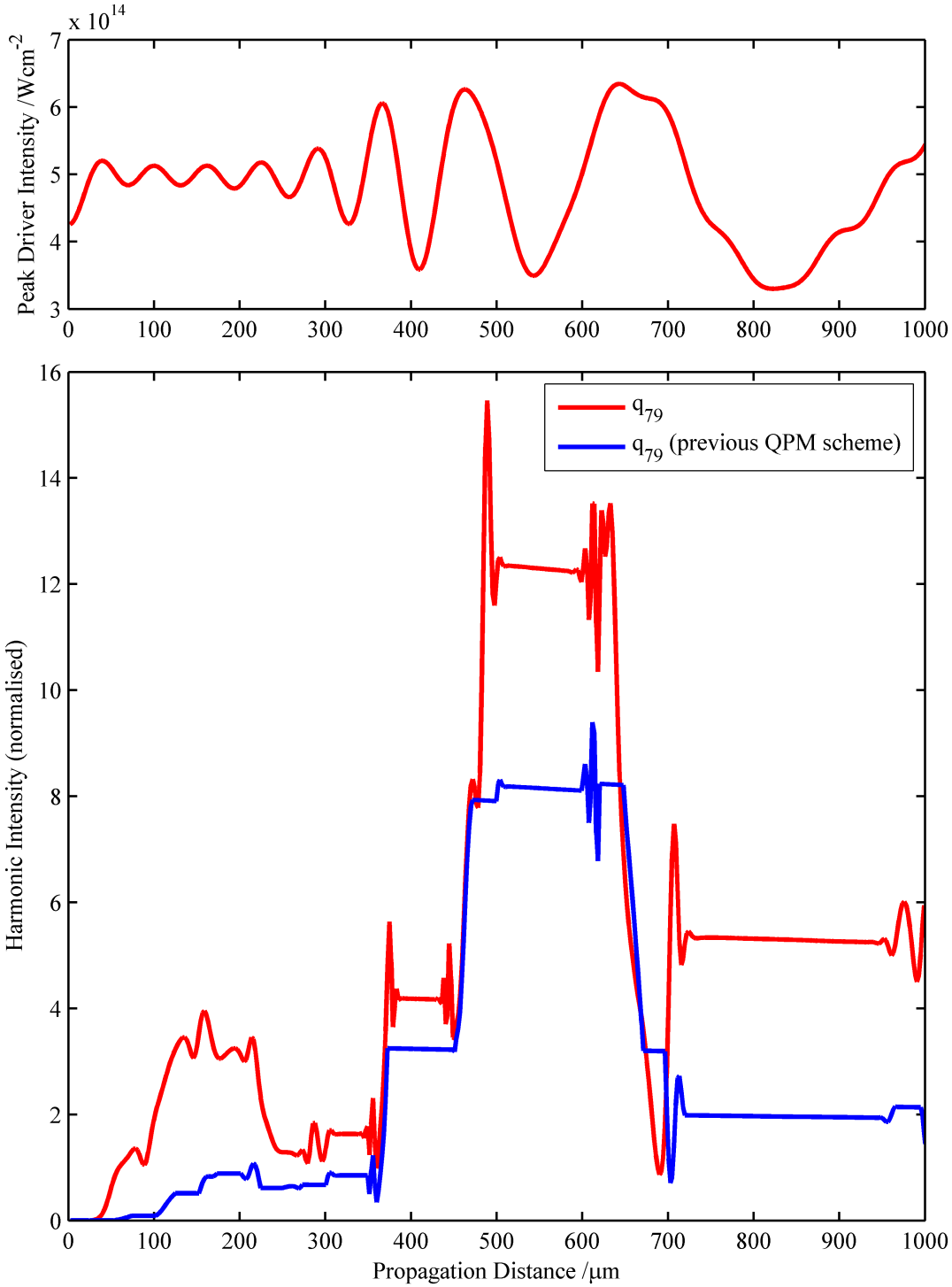

Figure 4.6: Calculated intensity of the driving pulse ($\lambda_0 = 800\,\text{nm}$, $\tau_p = 60\,\text{fs}$ and $I_{\text{peak}} = 5 \times 10^{14}\,\text{Wcm}^{-2}$, upper plot), modified to simulate the beating in a capillary with input spot-size $w_0 = 0.6435a$ and the 79th harmonic generated in 30 mbar argon, as a function of propagation distance (lower plot). The calculated harmonic intensity is also shown, where the same QPM scheme as in Figure 4.5 has been applied.

no longer matches the coherence length. The situation would be even worse if the spot size was not matched to the capillary radius, as it is in this example, since the intensity variation would be even greater due to the excitation of higher-order modes.

Clear coherent zones have nevertheless been observed when generating harmonics in capillary waveguides, for example in the work described in Chapter 6. This can be explained by the fact that these experiments are generally performed in waveguides longer than the 1 mm simulated here. We have seen that the loss-length is shorter for higher-order modes and that these modes also have smaller group velocities and will no longer overlap with the lowest-order mode after a certain propagation distance. Therefore the beating effect will be reduced for increased propagation distances and the intensity will be more uniform. However, these simulations make clear that if the waveguide is too short or the input laser spot is not well-matched to the capillary, intensity fluctuations due to mode beating will make quasi-phase-matching very difficult to achieve.

4.4.2 Mode Beating as a Mechanism for QPM

Note that the calculated harmonic intensity in Figure 4.6 still grows to be over an order of magnitude greater than that calculated in Figure 4.5 for the non-QPM case, in the absence of mode beating. It is unclear if this enhancement in the presence of mode beating is caused by the periodic longitudinal intensity variation acting as a QPM mechanism, or is solely due to the localised increases in driving intensity.

Even for the ideal coupling of a Gaussian beam into a capillary waveguide, high-frequency oscillations of the longitudinal intensity are present due to the excitation of high-order modes. If the period of these oscillations is equal to $2L_c$, QPM may be achieved. Figure 4.7 shows

the intensity of the 77th harmonic for a pulse with peak intensity $I_{\text{peak}} = 5 \times 10^{14}\,\text{Wcm}^{-2}$ and $\tau_p = 50\,\text{fs}$, in 10 mbar argon. The growth in harmonic intensity is shown for the case of no mode-beating and where the intensity varies according to the calculated mode-beating for a capillary with radius $a = 51\,\mu m$ and $w_0 = 0.6435a$. It is seen that the presence of mode-beating increases the harmonic intensity by almost three orders of magnitude. The coherence length of the harmonic generation without mode-beating is measured to be 0.07 mm, so in order to quasi-phase-match, intensity variations with a period of 0.14 mm would be required. For this capillary the mode-beating period, given by Equation (4.11), satisfies this requirement for the case of beating between the 1st and 14th modes. From Equation (4.2), the ratio of the powers coupled into these two modes is $C_{14}^2/C_1^2 \approx 10^{-4}$.

The transverse spatial profile of the beam entering the capillary can be changed to manipulate the QPM effect, for example by changing the input spot-size, the excitation of higher-order modes can be increased, leading to higher-amplitude beating. Figure 4.7 shows the effect on the generated harmonic intensity of reducing the spot-size to $w_0 = 0.6a$. Despite the reduced peak driver intensity, a greater enhancement in the generated harmonic intensity is observed. This suggests an increased enhancement from QPM, due to the 14th harmonic being excited with a greater amplitude and the beating between this mode and lowest-order mode becoming greater.

The effects of quasi-phase-matching and increased driver intensity as causes of the harmonic enhancement may be disentangled by considering a uniform driver intensity, comparable to the peak longitudinal intensity obtained with mode-beating. This is also shown in 4.7. A peak driver intensity of $I_{\text{peak}} = 5.9 \times 10^{14}\,\text{Wcm}^{-2}$ is used and mode-beating is neglected. It can be seen that the harmonic intensity is still greater in the presence of mode-beating by a factor of two, suggesting that although the increased driver intensity has a large effect, there is still an enhancement in the harmonic intensity due to QPM.

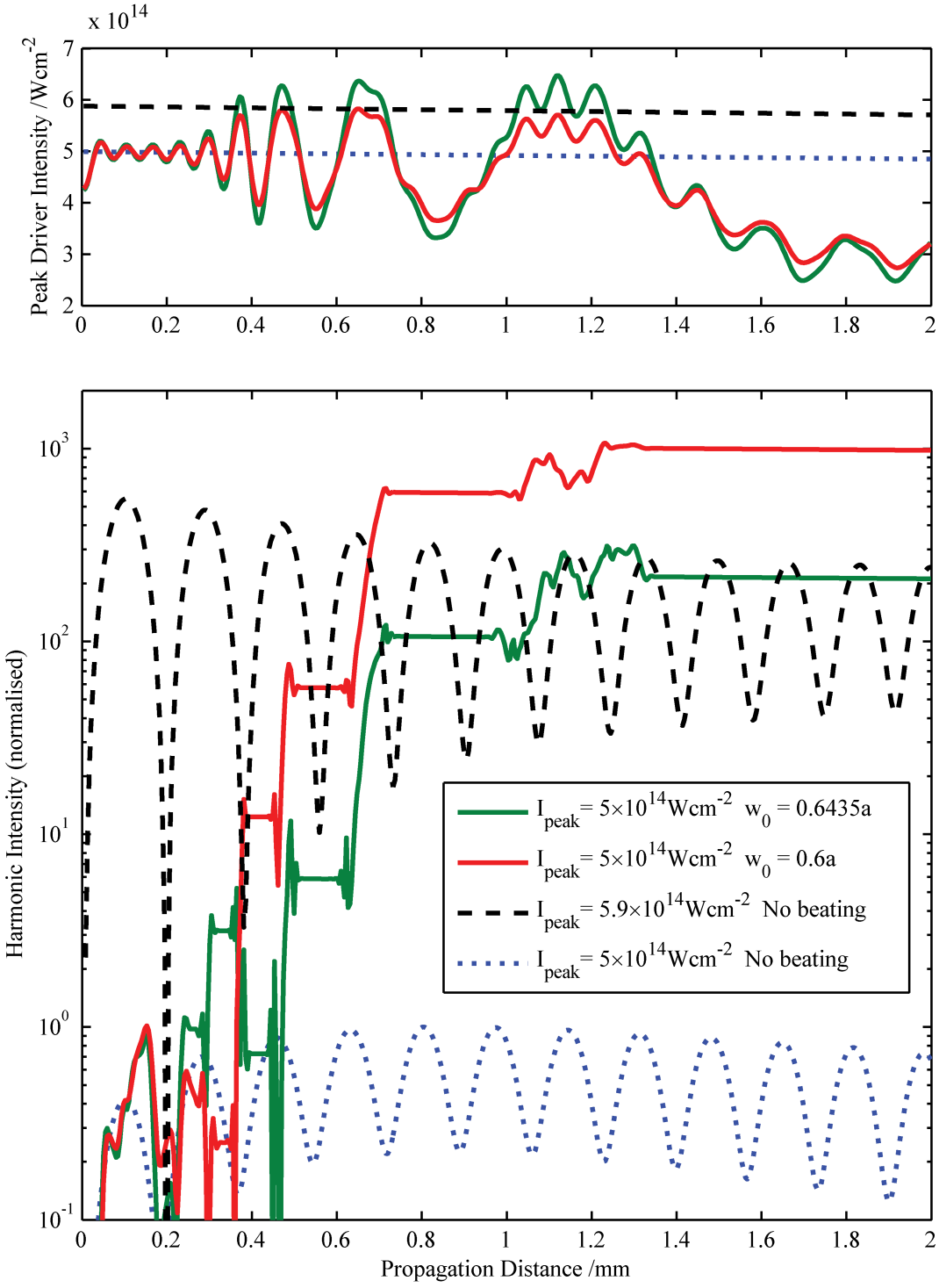

Figure 4.7: Calculated intensity of the driving pulse ($\lambda_0 = 800\,\text{nm}$, $\tau_p = 60\,\text{fs}$ and $I_{\text{peak}} = 5 \times 10^{14}\,\text{Wcm}^{-2}$, upper plot), without beating and modified to simulate the beating in a capillary with input spot-sizes $w_0 = 0.6435a$ and $w_0 = 0.6a$. Also shown is the driving intensity for a pulse with $I_{\text{peak}} = 5.9 \times 10^{14}\,\text{Wcm}^{-2}$. The lower plot shows the resulting intensity of the 77th harmonic generated in each case, in 10 mbar argon, as a function of propagation distance.

4.5 Conclusion

A model for the propagation of a driving laser pulse and the generated harmonic pulse, including the effect of mode-beating in a capillary waveguide, has been developed. It has been shown that over the first millimeter of propagation, mode-beating has a strong effect on the generated harmonics and makes QPM very difficult to achieve in this region. It has also been shown that the mode-beating itself can be used as a QPM mechanism, with an increase in harmonic intensity of a factor of two observed over just 2 mm, simply by adjusting the input spot-size and manipulating the excited modes.

In the analysis up to now I have only considered a Gaussian input spot, but the beam could be manipulated to specifically excite certain modes, by using a spatial light modulator to control the transverse phase and amplitude profile of the beam before the focus[67]. The longitudinal intensity profile due to beating could then be adjusted, in order to optimise the QPM effect.

Chapter 5

The Generation of Ultrafast Pulse Trains

5.1 Introduction

Sequences of closely-spaced ultrashort optical pulses have a range of practical applications, ranging from the generation of terahertz radiation and the control and measurement of atomic and molecular processes to quasi-phase-matching of HHG. I will review existing techniques for generating ultrafast pulse trains as well as some of their applications, before moving on to describe two novel techniques.

Femtosecond pulse trains have been used to study molecular motion in solids by driving selected vibrations of a crystal lattice[68]. By the process of impulsive stimulated Raman scattering, each femtosecond impulse imparts a driving force on the lattice. If the pulse train spacing is chosen correctly, these impulses will be in phase with a particular vibrational mode, leading to a higher amplitude and more selective excitation. The response of the medium can then be monitored using variably-delayed probe pulses, in order to study phonon-assisted

structural changes or chemical reactions.

More recently, a train of ultrashort pulses has been used to generate bursts of narrow-band terahertz-frequency light, by exciting photoconductive dipole antennas[69, 70]. The frequency of the generated radiation may then be tuned by varying the pulse separation in the train. Terahertz radiation has applications in spectroscopy[71], medical imaging[72] and the study of condensed matter in high magnetic fields[73].

The application with which this thesis is primarily concerned is optical QPM of high-harmonic generation, as discussed in Chapter 3. It is with this application in mind that the pulse train generation techniques introduced in this thesis were developed. To be used for this purpose, the pulse trains must fulfil certain criteria. They must have a high-energy (typically $\approx 1\,\mathrm{mJ}$) so that suppression of HHG is achieved, they must be flexible such that they can match a range of coherence lengths and they should have good contrast. The technique should also scale favourably to large numbers of pulses. It is also an advantage if the method is compact, robust and easily repeatable.

Existing methods for pulse train generation include the use of sequential Michelson interferometers[74], which have been used to produce up to 16 pulses. For n interferometers, trains of 2^n pulses may be generated, where the interpulse separation may be varied by adjusting the arm-lengths. This technique is capable of producing high-energy pulse trains reproducibly and efficiently (50% for linearly-polarised pulses), but for large numbers of pulses the scaling of the number of interferometers required is not practical.

An alternative method is to use pulse-shaping techniques in which phase and amplitude masks are placed in the focal plane of a zero-dispersion pulse stretcher[75]. The generation of up to 15 pulses has been demonstrated using this technique, with an energy of $100\,\mu\mathrm{J}$ per pulse. However, the use of these pulse-shaping methods to produce trains of high-energy

pulses is limited due to potential damage to the mask.

5.2 Measurement of Pulse Trains

If ultrafast pulse trains are to be generated, an accurate method is required to characterise them. This is especially important when performing QPM, since the pulse train period should match the coherence length. All of the pulse train measurements presented in this thesis were performed by cross-correlating the train with a single "probe" pulse. This was achieved by overlapping the pulse train and probe beams in a type-II SHG crystal where they generated light at 400 nm. Since this is a nonlinear process, there was a large increase in the intensity of the SHG light when the probe and pulse train pulses were temporally overlapped in the crystal. The delay between the pulse train and probe pulse could be adjusted using a timing slide in one of the beams, allowing the position of overlap to be varied. The SHG signal as a function of timing slide delay then closely mirrored the intensity of the pulse train as a function of time.

Consider an individual pulse in the train and a probe pulse, both having Gaussian temporal intensity distributions with intensity full-width at half-maximum (FWHM) durations of τ_{pt} and τ_p respectively. A timing slide position x corresponds to a delay between the two pulses of $2x/c$. The intensities of the pulse train pulse, I_{pt} and the probe pulse, I_{p} in the frequency-doubling crystal are then:

$$I_{\mathrm{pt}} = I_{\mathrm{pt}}^{0} \exp\left(-4\ln 2\left[\frac{t}{\tau_{\mathrm{pt}}}^{2}\right]\right), \tag{5.1}$$

$$I_{\mathrm{p}} = I_{\mathrm{p}}^{0} \exp\left(-4\ln 2\left[\frac{t-2x/c}{\tau_{\mathrm{p}}}^{2}\right]\right). \tag{5.2}$$

The measured SHG signal I_{SHG} is proportional to the product of the probe and pulse train

intensities within the crystal, as:

$$I_{\mathrm{SHG}} \propto \int_{-\infty}^{\infty} I_{\mathrm{pt}}(t) I_{\mathrm{p}}(t,x) dt \tag{5.3}$$

$$\propto \exp\left(-4\ln 2 \left[\frac{2x}{c\sqrt{\tau_{\mathrm{pt}}^2 + \tau_{\mathrm{p}}^2}}\right]^2\right), \tag{5.4}$$

which is a Gaussian with FWHM duration,

$$\sigma = \frac{c}{2}\sqrt{\tau_{pt}^2 + \tau_{pt}^2}. \tag{5.5}$$

Therefore the measured signal will have wider pulses than the actual train, although the train itself can be recovered by deconvolving with the temporal profile of the probe pulse if it is known sufficiently well.

5.3 The Birefringent Crystal Array Technique

The first technique introduced here for ultrashort pulse train generation makes use of multiple birefringent crystals[76]. Birefringent materials have a polarization-dependent refractive index since they respond differently to the propagation of light through them depending on their orientation to the electric field. Birefringent materials can be thought of as having two axes: the ordinary and extraordinary with refractive indices n_{o} and n_{e} respectively. The birefringence Δn of a material is defined as:

$$\Delta n = n_{\mathrm{e}} - n_{\mathrm{o}}. \tag{5.6}$$

Consider a linearly-polarised pulse of light incident on a birefringent crystal of length x, with the plane of polarisation at 45° to the ordinary axis. This pulse can be resolved into two discrete pulses with equal intensities, one polarized parallel to the ordinary axis and the other parallel to the extraordinary axis. Due to the birefringence of the crystal, these two pulses will propagate through the crystal with different group velocities, $v_{\mathrm{g}}^{\mathrm{o}}$ and $v_{\mathrm{g}}^{\mathrm{e}}$. On leaving the crystal, the two pulses will be separated in time by Δt,

$$\Delta t = x\left(\frac{1}{v_{\mathrm{g}}^{\mathrm{e}}} - \frac{1}{v_{\mathrm{g}}^{\mathrm{o}}}\right), \tag{5.7}$$

leading to two orthogonally-polarised, temporally-separated pulses.

Similarly, if these pulses are passed through another crystal with the same birefringence, but with double the length and with the optical axis oriented so that it is again at 45° to the plane of polarisation of both incoming pulses, the number of pulses will again be doubled. Each additional crystal, of twice the length of the previous one will double the length of the pulse train, so n crystals gives 2^n pulses of equal intensity. In practise, materials of different birefringences may be used, as long as their lengths are chosen so that Δt doubles for each successive crystal. The first and second half of the pulse train will always have orthogonal polarisations, although the polarisations of all the pulses in the train can be made parallel by using a linear polarizer oriented at 45 degrees to the polarisations of the pulses. Hence if pulses with the same polarisation state are required, this technique is 50% efficient. Figure 5.1 illustrates schematically the generation of a train of eight equally-spaced pulses using this method.

The use of multiple crystals to generate a pulse train will add significant material dispersion to the optical path. This can be compensated for by adjusting the compressor in

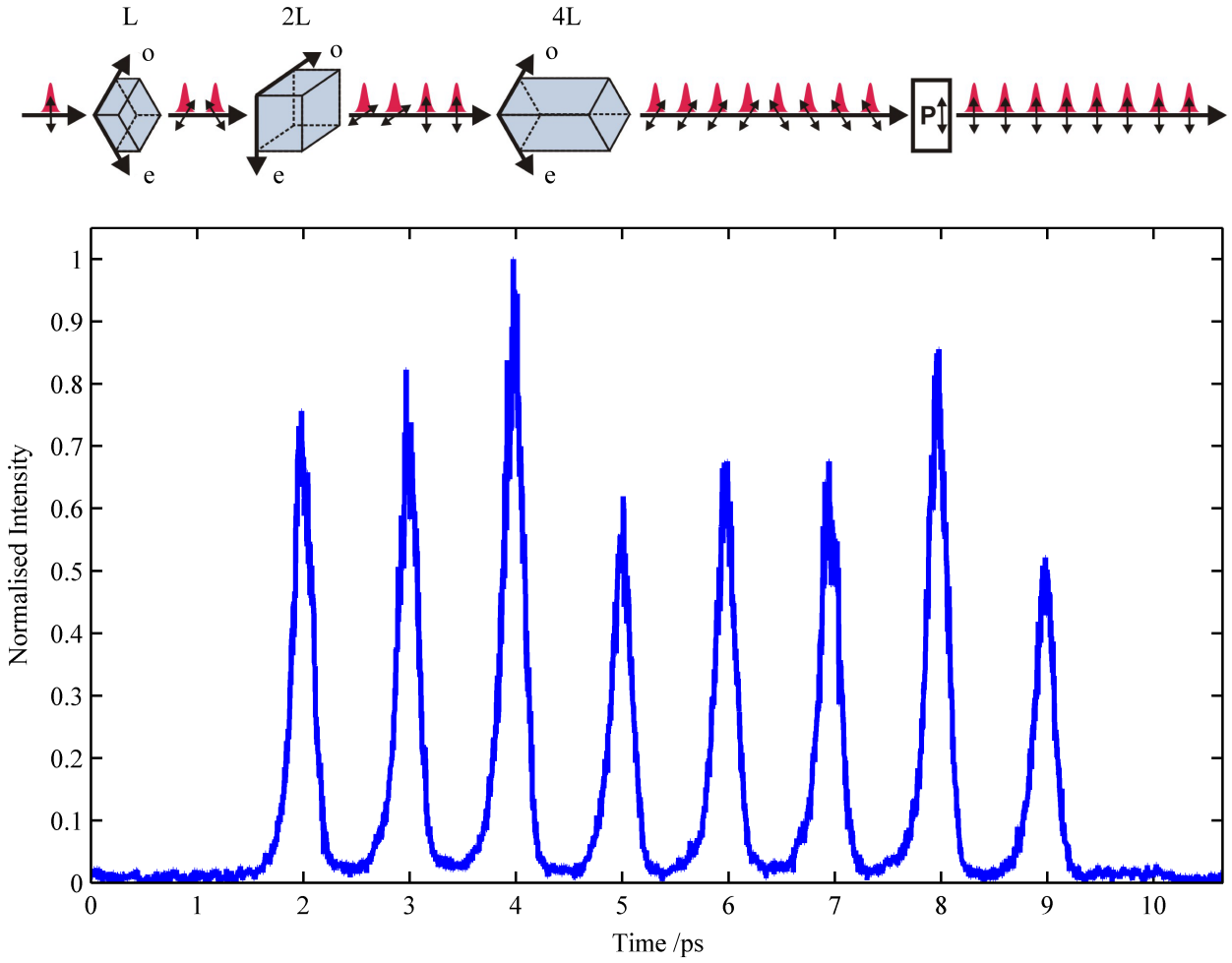

Figure 5.1: A schematic of the arrangement for creating a train of eight equally-spaced pulses, using an array of three birefringent crystals. Below is shown a cross-correlation of a pulse train generated using such an array, obtained by overlapping the pulse train with a probe pulse in a BBO crystals and measuring the second-harmonic light generated as a function of the delay between them.

the CPA laser system. For this reason it is advantageous to keep the amount of material in the beam constant when changing to different pulse trains, so that the compressor does not have to be continually adjusted. This can be achieved since the birefringent crystals which are not necessary for the current pulse train can simply be placed at the front of the crystal array, with the optical axis aligned parallel to the polarisation of the incoming optical pulse. The pulse then experiences the GVD of the material, without being split.

The data presented here was produced by passing a laser pulse of FWHM duration 200 fs through six calcite crystals of length 0.42, 0.83, 1.66, 3.33, 6.65, and 13.3 mm. Calcite is typically used as the birefringent medium, due to its large Δn. The Sellmeier equation for calcite yields $n_o = 1.658$ and $n_e = 1.486$, for $\lambda = 800\,\text{nm}$, giving a pulse splitting of 575 fs per mm of material. The thinnest crystal leads to a pulse splitting of 250 fs such that the split pulses will still overlap. This is evident in Figure 5.2, which shows a train of 64 pulses with this minimum spacing. The crystals in the array are alternately oriented at 0 degrees and 45 degrees so that splitting occurs at each one, to produce $2^6 = 64$ pulses. The individual pulses overlap but are still just discernible. If the first (thinnest) crystal is removed then 32 pulses will be generated, with a spacing which is double the minimum possible spacing.

For quasi-phase-matching under conditions of constant L_c we require a pulse train in which the pulse-separation is equal to the pulse width. This is possible by using a number of overlapping single pulses as individual "macropulses" in the train. For example, Figure 5.3 shows a pulse train in which each pulse in the train is formed from four overlapping pulses. This is achieved by alternating the crystal alignment in order of increasing thickness, but removing the third thinnest crystal. This method produces pulses which are approximately square, which is useful where a sharper increase in intensity is required than that obtained

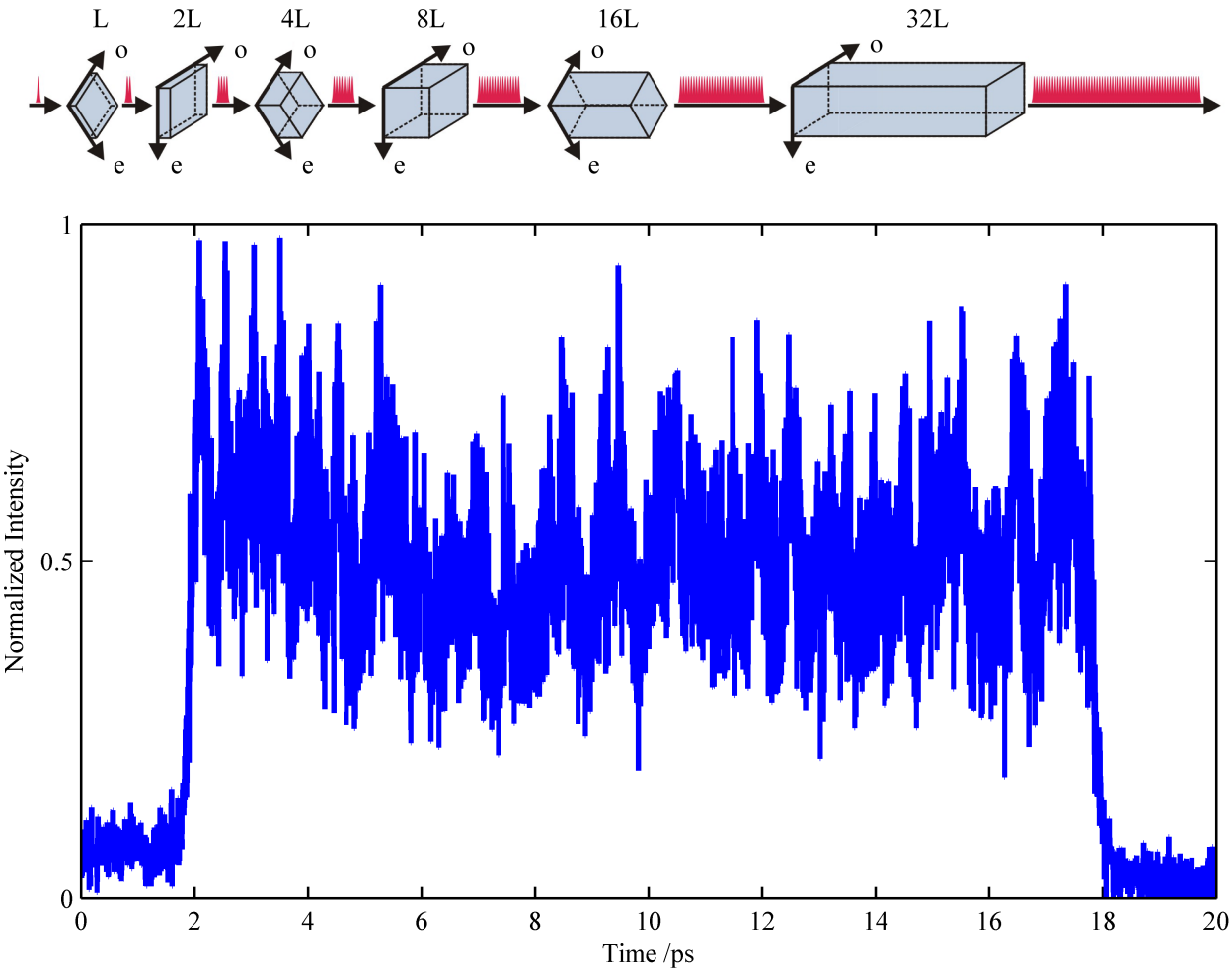

Figure 5.2: Crystal arrangement and cross-correlation of a macropulse consisting of a train of 64 overlapping pulses. Calcite crystals were used, with $L = 0.42\,\mathrm{mm}$.

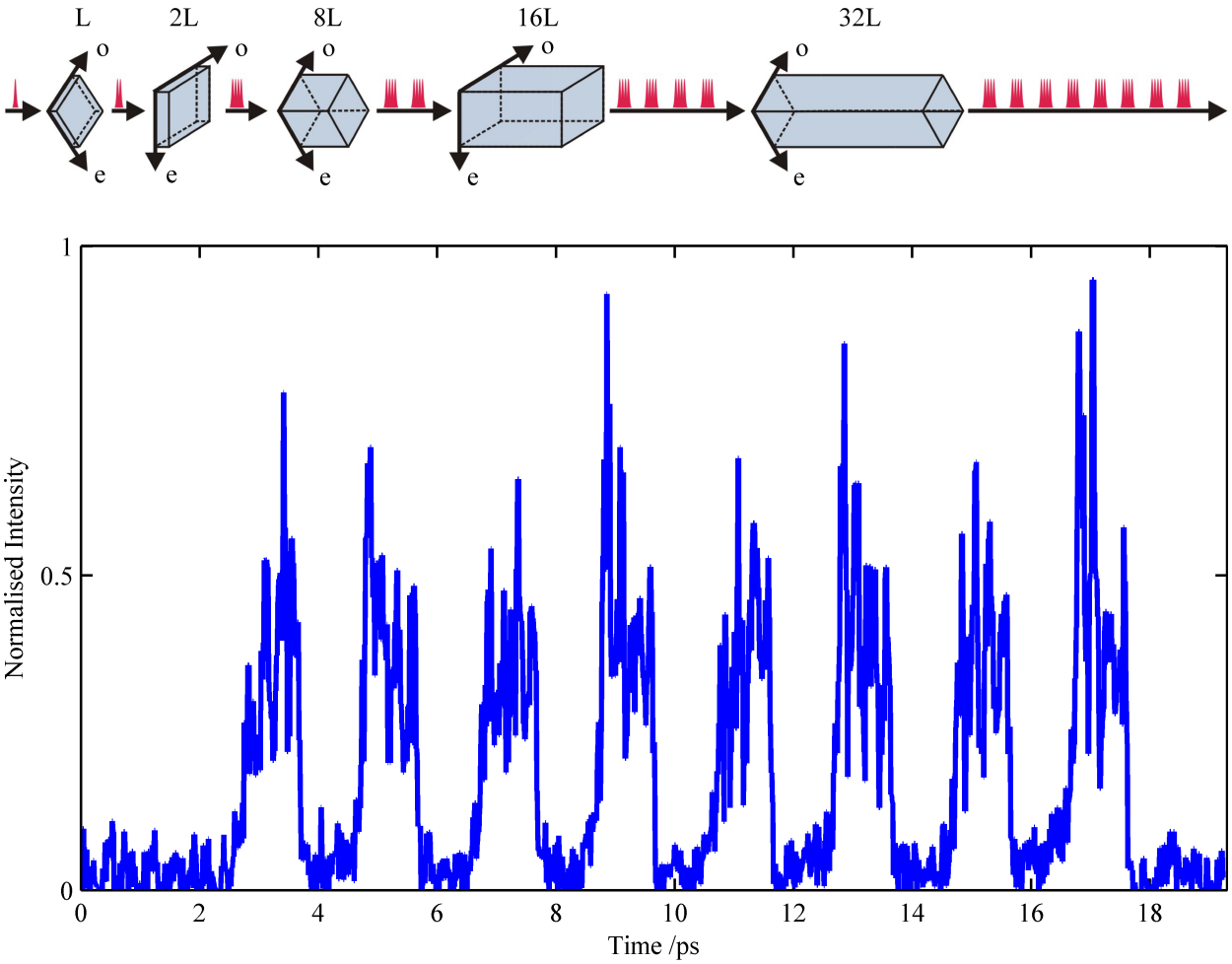

Figure 5.3: Crystal arrangement and cross-correlation of a train of macropulses, each consisting of four overlapping pulses.

with a Gaussian pulse.

It is seen that the peak pulse intensity is not constant within these trains. This is largely due to misalignment of the optical axes of the crystals relative to the plane of polarisation of the pulse. For equal splitting, the plane of polarisation must be at exactly 45 degrees to the optical axis of the crystal. For an uncertainty in crystal orientation of δ radians over n crystals, the ratio of the intensities of the strongest and weakest pulses, ν is given

approximately by:

$$\nu = \left(\frac{\cos\delta + \sin\delta}{\cos\delta - \sin\delta}\right)^{2n} \approx \left(\frac{1+\delta}{1-\delta}\right)^{2n} \tag{5.8}$$

The uncertainty in orientation for the data presnted here was approximately 2 degrees. Over 6 crystals, this gives $\nu \approx 2$, which approximately matches the observed variation in pulse intensity for the case of 64 pulses, shown in Figure 5.2.

This technique is a flexible and compact method for producing trains of ultrashort pulses. One major advantage of this method is that it produces pulse trains which are very reproducible. All that is required to generate a certain train is to orient the crystals correctly, which is easily reproducible if calibrated rotation-mounts are used, without requiring repeated characterisation of the train to ensure that it is correct.

5.4 The Single Birefringent Crystal Technique

The second method for generating ultrafast pulse trains also makes use of birefringence, but by a different mechanism and uses only one birefringent crystal, acting as a multiple-order wave plate.

In this technique, first proposed by Yano et al.[77], a linearly-polarised laser pulse is passed through a grating-pair stretcher, introducing a frequency-chirp. A multiple-order wave plate is placed after the stretcher, with its fast axis at 45° to the plane of polarisation of the laser pulse. Finally, a linear polariser is placed after the wave plate, with its transmission axis parallel to the original plane of polarisation of the light pulse.

In order for the light to be transmitted by the polariser, the wave plate must introduce a phase-shift of $2m\pi$ (m, an integer) between the field components polarised parallel and

perpendicular to the fast axis of the wave plate. For a wave plate of a given thickness, this condition will only be met for certain frequencies and since the laser pulse is frequency-chirped, the pulse after the polariser will be modulated to form a series of pulses. One consequence of this is that the optical frequency variation across the pulse train will be approximately equal to the bandwidth of the original pulse. This may be important if the pulses are being used for spectroscopy, but for the case of QPM, where the pulses are simply being used to disrupt HHG, this is unimportant.

Consider a chirped Gaussian pulse of instantaneous frequency $\omega_0 + 2bt$ and electric field amplitude A. The field in the plane $z = 0$ is given by[2]:

$$E(z=0,t) = A\exp\left(-at^2\right)\exp\left[-i(\omega_0 t + bt^2)\right] \tag{5.9}$$

$$= A\exp\left(-\Gamma_0 t^2\right)\exp\left(-i\omega_0 t\right) \tag{5.10}$$

where $\Gamma_0 \equiv a + ib$ and $a\tau_p^2 = 2\ln 2$, in which τ_p is the intensity FWHM duration of the laser pulse.

We can calculate the effect of propagating such a pulse through a dispersive medium by taking the Fourier transform of the electric field, multiplying by the spectral phase encountered in the medium and then taking the inverse Fourier transform to return to the time domain. For the case of a quadratically-dispersive medium between the planes $z = 0$ and $z = \ell$, the amplitude of the pulse at $z = \ell$ may be written as:

$$E(\ell,t) = A\sqrt{\frac{\Gamma(\ell)}{\Gamma_0}}\exp[\mathrm{i}(\beta_0\ell - \omega_0 t)]\exp\left[-\Gamma(\ell)(t-\beta_0'\ell)^2\right] \tag{5.11}$$

where $\Gamma(\ell)^{-1} = \Gamma_0^{-1} - 2\mathrm{i}\beta_0''\ell$, and where for an angular frequency of ω_0 the wave vector,

group velocity, and reciprocal group velocity dispersion (GVD) of the medium are given by β_0, $1/\beta_0'$, and β_0'' respectively.

Equation (5.11) may be written more conveniently as,

$$E(\ell,t) = f(\ell,t)\exp(-\mathrm{i}\omega_0 t)\exp[\mathrm{i}\phi(\ell,t)], \tag{5.12}$$

where

$$f(\ell,t) = A\exp\left\{-\Re[\Gamma(\ell)](t-\beta_0'\ell)^2\right\}, \tag{5.13}$$

$$\phi(\ell,t) = \beta_0\ell - \gamma(t-\beta_0'\ell)^2, \tag{5.14}$$

and

$$\gamma = \frac{b + 2\beta_0''\ell\,(a^2+b^2)}{(1+2\beta_0''\ell b)^2 + (2\beta_0''\ell a)^2}. \tag{5.15}$$

The amplitude of the radiation passing through the linear polarizer is given by $E_{\mathrm{pol}}(\ell,t) = [E_{\mathrm{e}}(\ell,t) + E_{\mathrm{o}}(\ell,t)]/\sqrt{2}$, where the amplitudes E_{e} and E_{o} are given by expressions of the form of 5.12 and the subscripts 'o' and 'e' denote the ordinary and extraordinary polarizations respectively.

Provided the *difference* of the second- and higher-order dispersion terms for the two polarisations in the wave plate are not too large, the pulse envelopes $f_{\mathrm{o}}(\ell,t)$ and $f_{\mathrm{e}}(\ell,t)$ will be approximately equal, and consequently we may write,

$$E_{\mathrm{pol}} \approx \sqrt{2}\bar{f}(\ell,t)\exp[\mathrm{i}\bar{\phi}(\ell,t)]\cos\left[\frac{\phi_{\mathrm{o}}(\ell,t) - \phi_{\mathrm{e}}(\ell,t)}{2}\right], \tag{5.16}$$

where $\bar{f}(\ell,t)$ and $\bar{\phi}(\ell,t)$ are the average pulse envelope and phases for the two polarizations. We see that the intensity of the chirped pulse leaving the combination of the wave plate

and polarizer is modulated by a cosine-squared function. In other words, a train of pulses is formed.

Peaks of intensity occur when the argument of the cosinusoidal function is equal to $m\pi$, where m is an integer, i.e. when

$$\beta_{0\mathrm{o}}\ell - \beta_{0\mathrm{e}}\ell + \gamma_{\mathrm{e}}(t - \beta'_{0\mathrm{e}}\ell)^2 - \gamma_{\mathrm{o}}(t - \beta'_{0\mathrm{o}}\ell)^2 = 2m\pi. \tag{5.17}$$

The interval between adjacent pulses is then given by,

$$\Delta\tau = \frac{\pi}{(\beta'_{0\mathrm{e}}\gamma_{\mathrm{e}} - \beta'_{0\mathrm{o}}\gamma_{\mathrm{o}})\ell + (\gamma_{\mathrm{o}} - \gamma_{\mathrm{e}})t} \tag{5.18}$$

$$\approx \frac{\pi}{b\ell}\frac{1}{\beta'_{0\mathrm{e}} - \beta'_{0\mathrm{o}}}, \tag{5.19}$$

where the approximation holds if the group velocity dispersion in the wave plate is small, whereupon $\gamma_{\mathrm{o}} \approx \gamma_{\mathrm{e}} \approx b$. We see that if the initial stretched pulse has a constant frequency chirp, and group velocity dispersion in the wave plate can be neglected, the pulses in the train have a constant separation. If these conditions are not met the spacing of pulses in the train will vary during the train, as we will se in Section 5.5.

The relative variation of the separation of the pulses will be most severe when the duration of the stretched pulse is long and the thickness of the wave plate is small. As an example, for calcite we find for the ordinary and extraordinary polarizations respectively at 800 nm: β'_0 equal to 5.58 and 4.98 ps mm^{-1}; β''_0 equal to 76.2 and 39.6 fs^2 mm^{-1}. For the longest stretched pulse used in this work (33 ps) and the thinnest wave plate (0.826 mm), the measured mean pulse spacing of 14 ps corresponds to a b-parameter of 0.45 ps^{-2}. From

Equation (5.18) it is then found that the pulse spacing varies by less than 0.2% over the FWHM duration of the train of pulses.

This pulse train technique was investigated experimentally, using a 10 Hz Ti:Sapphire CPA laser system, delivering linearly-polarised pulses with energy up to 125 mJ at a centre wavelength of 808.8 nm. A schematic diagram of the experimental setup is shown in Figure 5.4. Prior to the compressor, the beam was split using a beamsplitter of 25% reflectivity. The reflected beam was used to form the pulse trains studied in this work, while the transmitted beam was used as a probe. This probe beam could be delayed relative to the driver beam using a computer-controlled timing slide, giving a possible variation of path-difference between the two beams of up to 680 mm. The duration of the driver and probe pulses was measured after the compressor by autocorrelation and minimised by adjusting the grating separation. The pulse train and probe beams were compressed side by side in the same compressor to give pulses of 70 fs and 80 fs duration respectively.

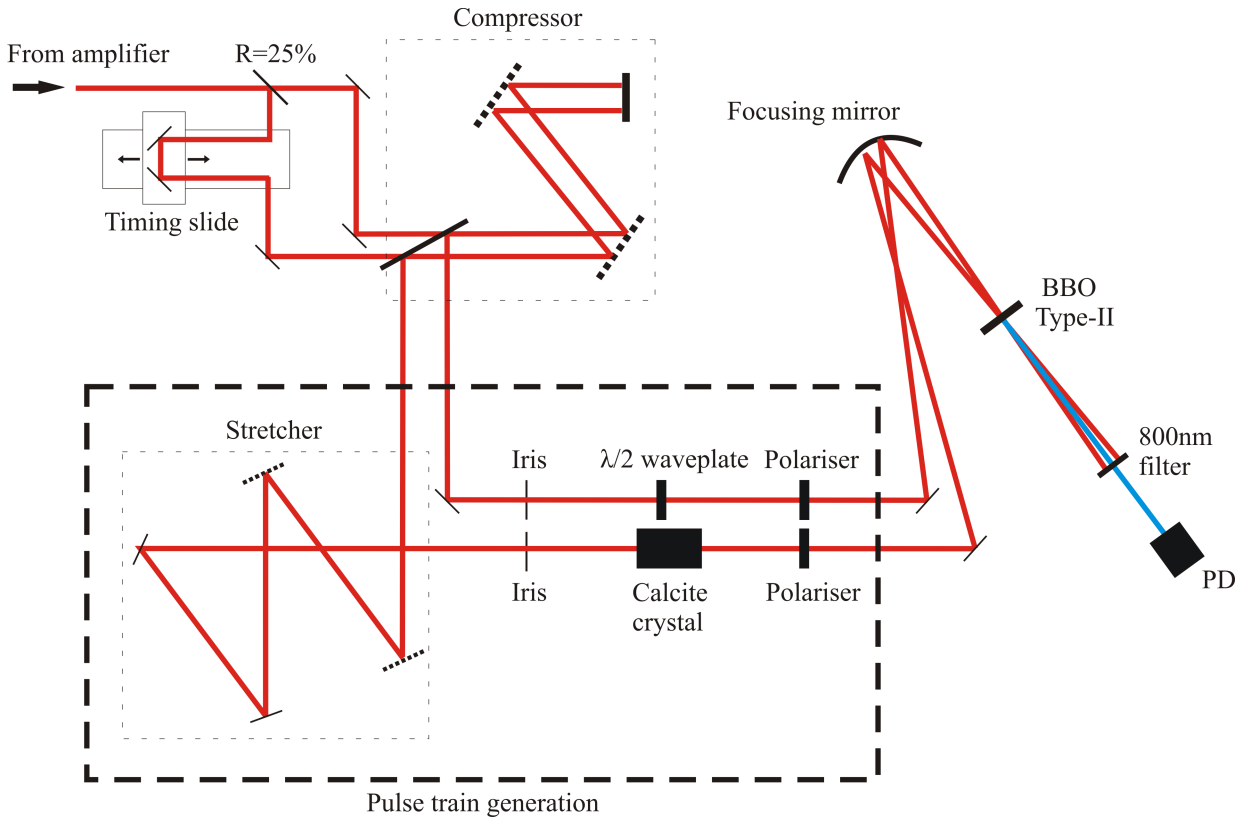

Figure 5.4: Schematic diagram of the experimental arrangement employed to generate trains of femtosecond pulses, using a multiple order wave plate and linear polariser.

The probe beam passed through a rotatable half wave plate and a linear polariser oriented vertically, to enable the energy of the probe pulses to be adjusted. The driver pulse was re-stretched using a pair of gratings with 1200 lines/mm. By varying the separation of the gratings, stretched pulse durations of between 5 ps and 33 ps were obtained. The stretched pulse train beam then passed through a calcite multiple-order wave plate oriented with its fast axis at 45° to the plane of polarisation and a linear polariser oriented parallel to the plane of polarisation of the beam prior to the wave plate.

Cross-correlation of the driver and probe pulses was performed by overlapping the two beams in a 1 mm-thick BBO crystal and observing the intensity of the second-harmonic light generated as the timing slide was adjusted. The separation of the stretcher gratings in the pulse train beam was adjusted to give stretched pulses of FWHM duration between 5 and 33 ps. Calcite crystal waveplates of thicknesses between 0.8 mm and 26.4 mm were used to create pulse trains using these stretched pulses.

The results of the cross-correlations performed with pulse trains generated from each of these stretched pulses is shown in Figure 5.5. In each case the first plot shows the cross-correlation of the stretched pulse, without the calcite crystal or polariser present in the beam. The subsequent plots show the cross-correlations measured with calcite crystals of various thicknesses inserted into the stretched beam. The data-acquisition rate was adjusted so that there were approximately 30 data points per pulse in the train. The noise in the cross-correlations arises from fluctuations in the energies of the two beams.

It is seen that as the crystal thickness is increased, the number of pulses obtained from the stretched pulse increases and the separation between pulses decreases. This is because the separation between the frequencies in the chirped pulse which are retarded enough to result in the required change in polarisation decreases as the crystal length increases, as can be seen from Equation (5.18). Figure (5.6) shows how the separation of the pulses, $1/\Delta\tau$

varies as the crystal thickness is increased and shows the linear dependence expected from Equation (5.19).

Equation (5.16) indicates that the pulse train intensity should be a cosine-squared function of time. Hence the FWHM duration of the individual pulses is simply half the peak-to-peak separation of pulses in the cross-correlation. The average timing-slide separation between peaks in the pulse train obtained with a 10 ps stretched pulse and 6.61 mm-long crystal, shown in Figure 5.5b is 0.06 mm, giving a FWHM pulse duration of the individual peaks of 200 fs. Pulses of shorter duration could not be resolved because the cross-correlation is a convolution of the pulse train with the 80 fs probe pulse. Hence adjacent pulses overlap for pulse trains with individual pulse durations much shorter than 200 fs. However, this does not represent a limit on the minimum pulse duration of the pulses generated using this method.

The convolution of the pulse train with the probe pulse also accounts for the decrease in pulse contrast as we move to shorter individual pulse durations. This is illustrated by the calculation presented in Figure 5.7. The cross-correlation data for the driving pulse with no crystal present (Figure 5.5b, top plot) is multiplied by a cosine-squared function of the same period as that of the pulse train obtained when a crystal of length 6.61 mm is used. This data is then convolved with a Gaussian of duration 80 fs, representing the probe pulse. The plot shows a reduction in contrast similar to that found experimentally.

Any higher-order dispersion in the system will introduce a non-linear chirp to the pulse. For example, third-order dispersion will be evident as a linear variation of the separation of pulses in the pulse train. Figure 5.8 plots $\Delta\tau$ as a function of time for pulse trains produced by passing a 33 ps stretched pulse through wave plates of varying thickness. It is clear that $\Delta\tau$ varies slightly with position in the pulse train; this third-order dispersion could originate from the grating pair or the wave plate material. Indeed in principle, higher-order dispersion

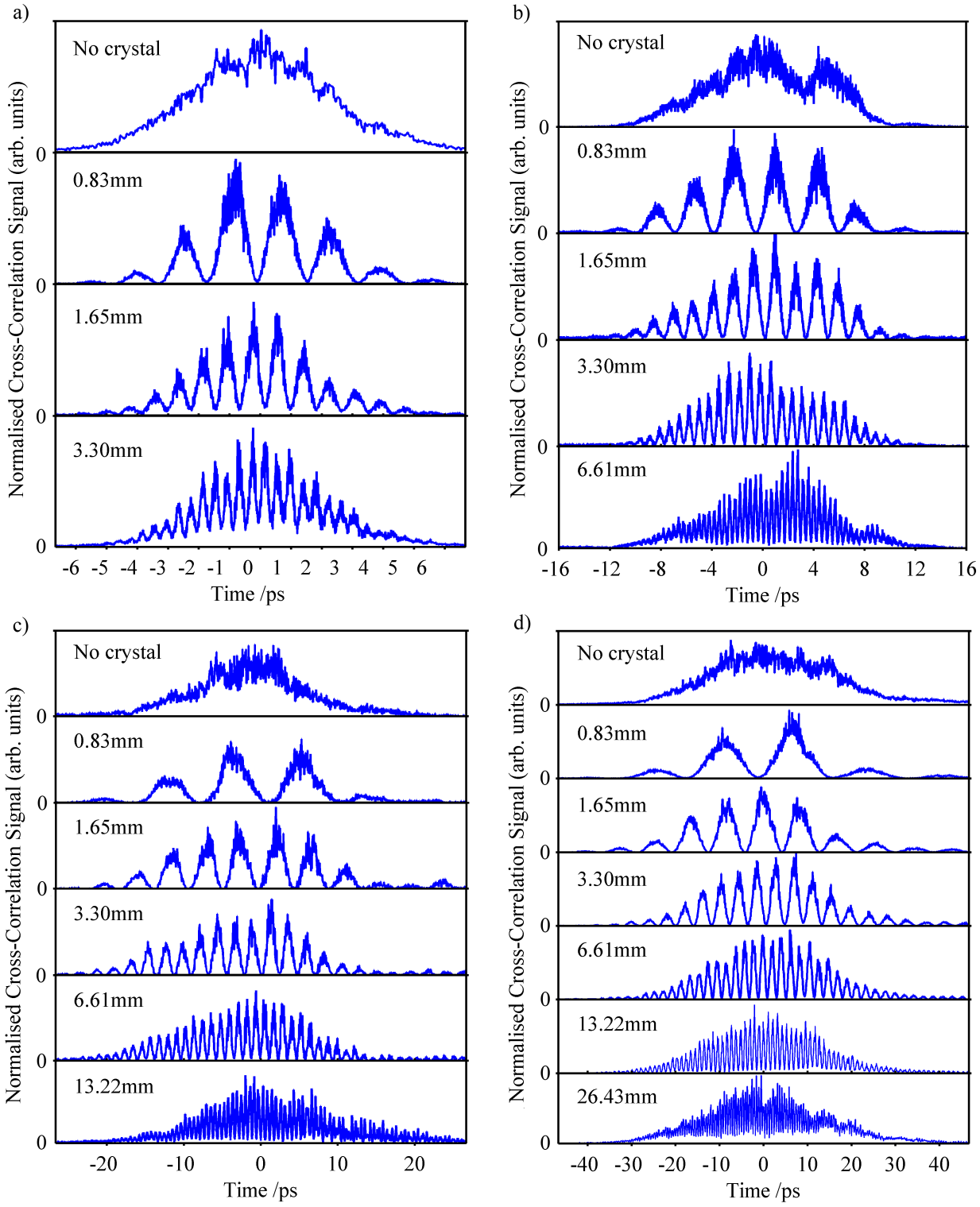

Figure 5.5: Normalised cross-correlation traces obtained with a stretched pulse of a) 5 ps, b) 10 ps, c) 15 ps and d) 33 ps FWHM duration and multiple-order calcite wave plates of various thicknesses.

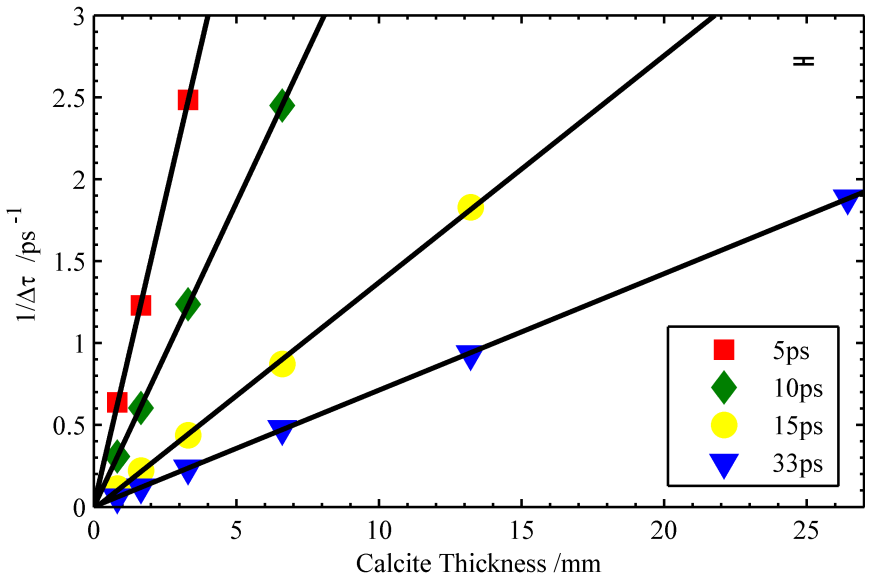

Figure 5.6: Plot of $1/\Delta\tau$ as a function of the thickness of the calcite crystal for stretched pulses of duration 5, 10, 15 and 33 ps, showing the expected linear dependence of Equation (5.19). A typical error bar is also shown.

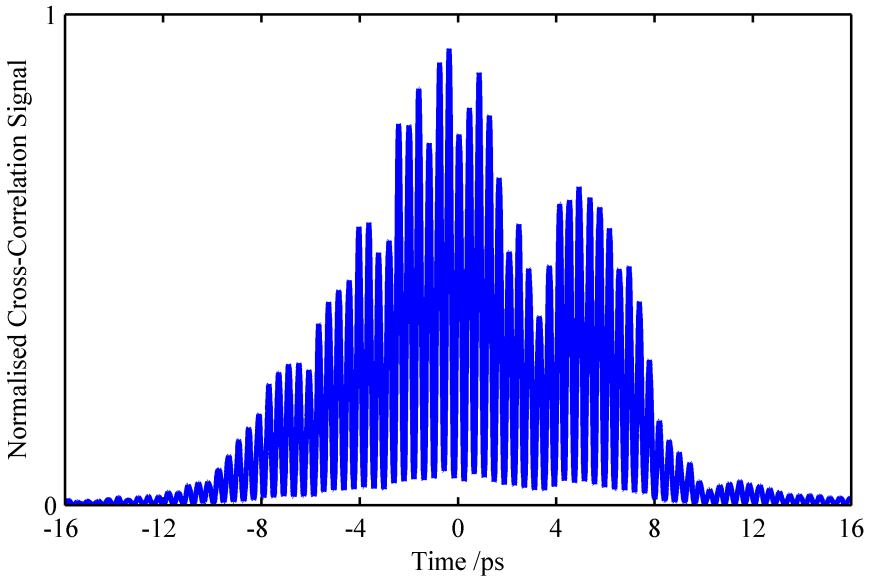

Figure 5.7: A convolution of an 80 fs Gaussian pulse with the data from Figure 5.5b for the case of no crystal, convolved with a cosine-squared function of the same period as that of the pulse train obtained with a 6.61 mm-long crystal, showing the resultant loss of contrast.

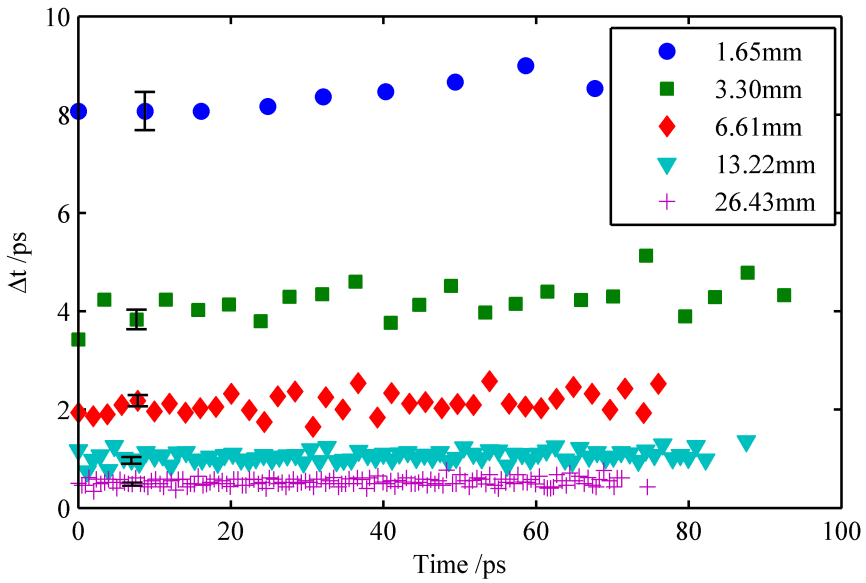

Figure 5.8: Variation of the pulse separation, Δt across the pulse train generated when a 30 ps stretched pulse passes through crystals of varying thicknesses. Typical error bars are shown for each set of data.

could be used to generate pulse trains with arbitrary variation of pulse separation within the train. This technique is demonstrated in the next section.

5.5 Chirped Pulse Trains

The techniques described above for the generation of ultrashort pulse trains produce trains in which the pulse-spacing is fixed. This is suitable for quasi-phase-matching HHG as long as the coherence length is also constant. In practise this is unlikely to be so since L_c depends on the free electron density, which itself depends strongly on the laser intensity. Even in a waveguide, L_c will vary with position due to absorption, defocusing and pulse broadening. Variation of the gas pressure will also lead to changes in L_c along the waveguide. For this reason it may be advantageous to quasi-phase-match with a train of pulses of varying and variable separation. We have seen that this is possible by applying higher-order dispersion.

If arbitrary dispersion can be applied to the stretched pulse then the pulse train may be tailored to match the coherence length in the generating medium.

Consider a pulse (prior to the wave plate and polariser), described as a superposition of harmonic waves of frequency ω described by

$$E = a(\omega) \exp\left[i\Phi(\omega, t)\right] \tag{5.20}$$

where $a(\omega)$ is the spectral amplitude, $\Phi(\omega, t) = \phi(\omega) - \omega t$ and $\phi(\omega)$ is the spectral phase. We can expand $\phi(\omega)$ in a Taylor series about a centre frequency ω_0, giving

$$\phi(\omega) = \sum_{n=0} \frac{1}{n!} \phi^{(n)} (\omega - \omega_0)^n \tag{5.21}$$

where $\phi^{(n)} \equiv \partial^n \phi / \partial \omega^n |_{\omega_0}$.

If we assume that the group delay dispersions of the waveplate and polariser are small, the frequencies passed by this combination are evenly spaced and given by $\omega_p - \omega_0 = p\Delta\omega$, where $p = 0, \pm 1, \pm 2, \pm 3....$ The time taken for the pth pulse, corresponding to a frequency $\omega_p - \omega_0 = p\Delta\omega$ to traverse the waveplate of length L is

$$\tau(p) = L \frac{\mathrm{d}k}{\mathrm{d}\omega} = \frac{\mathrm{d}\phi}{\mathrm{d}\omega} = \sum_{n=1} \frac{1}{(n-1)!} \phi^{(n)} (p\Delta\omega)^{n-1}. \tag{5.22}$$

The pulse spacing is then given by

$$\Delta\tau(p) = \frac{\mathrm{d}\tau}{\mathrm{d}p} = \sum_{n=2} \frac{1}{(n-2)!} \phi^{(n)} p^{n-2} (\Delta\omega)^{n-1}. \tag{5.23}$$

It can be seen that dispersion of order n gives a pulse spacing within the train which varies as p^{n-2}. It is therefore apparent that it is possible to vary $\Delta\tau$ arbitrarily through the pulse train by controlling the third and higher-order dispersions. Although a grating stretcher can provide such dispersion, independent control of each order of dispersion is not possible.

I will describe here the use of an acousto-optic programmable dispersive filter to introduce programmable higher-order phase variations to the stretched pulse, allowing the generation and control of chirped pulse trains[78].

5.5.1 Acousto-Optic Programmable Dispersive Filters

Spectral phase and amplitude control using spatial light modulators[79] and acousto-optic deflectors[80] has been shown to produce nearly arbitrary ultrafast optical waveforms. These devices are placed in the Fourier plane of a zero-dispersion optical line, where the spectral components are spatially separated so that they can be individually manipulated. These techniques have been used to correct for high-order dispersion introduced by laser-amplification systems, leading to shorter output pulses[81]. However, these techniques require multiple high-quality optical elements and are bulky. A pulse energy limitation is also imposed by the damage threshold of these devices.

In the experiments described here, an acousto-optic programmable dispersive filter (AOPDF) [82] was used to manipulate the spectral phase and amplitude of the chirped pulses used to generate pulse trains. This device makes use of the collinear and codirectional coupling in a uniaxial birefringent crystal, by an acoustic wave, of the ordinary and the extraordinary optical waves. The device is compact and can be placed directly in the path of the stretched, chirped pulse, as opposed to being placed in the Fourier plane.

Figure 5.9 shows a schematic of the principle of operation of an AOPDF. A radio fre-

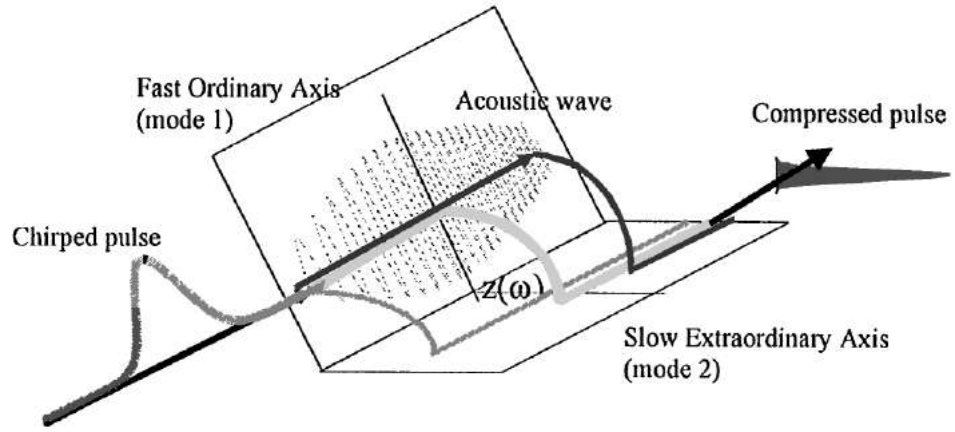

Figure 5.9: Principle of operation of an AOPDF. An acoustic wave induces a longitudinal variation of refractive index, leading to diffraction of the incoming pulse in mode 1 into mode 2, which is orthogonally polarised. Figure from [83].

quency transducer launches an acoustic wave along the z-axis of the birefringent crystal, parallel to the direction of propagation of the optical pulse. The acoustic wave propagates at some speed $v \ll c$ along the z-axis, spatially reproducing the temporal r.f. signal. The mechanical strain within the crystal induces a change of refractive index. This variation of refractive index constitutes a diffraction grating which will diffract part of the incident optical energy from the ordinary axis (mode 1) into the extraordinary axis (mode 2). Every frequency in the incident pulse traverses the crystal until it approaches a phase-matched spatial frequency in the acoustic grating at position $z(\omega)$, where it is diffracted into mode 2. Since the velocities of the two modes are different, the spectral amplitude and phase of the wave exiting the crystal in mode 2 can be determined, by controlling where along the crystal different frequencies are diffracted and with what strength.

An incident optical wave, with frequency ω_1, wavenumber β_1 and spectral electric-field amplitude $\tilde{E}_1(\omega_1)$, interacting with an acoustic wave with frequency Ω, spectral amplitude

$S_{\rm ac}(\Omega)$ and wavenumber K, will give a diffracted optical wave with frequency ω_2, wavenumber β_2 and spectral electric-field amplitude $\tilde{E}_2(\omega_2)$ given by:

$$\tilde{E}_2(\omega_2)\exp i(\omega_2 t-\beta_2 z)\propto\tilde{E}_1(\omega_1)\exp i(\omega_1 t-\beta_1 z)\times S_{\rm ac}(\Omega)\exp i(\Omega t-Kz). \tag{5.24}$$

Energy will only be transferred to mode 2 if the phase-matching conditions are met:

$$\omega_2 = \omega_1+\Omega \tag{5.25}$$

$$\beta_2 = \beta_1+K \tag{5.26}$$

we then have

$$\tilde{E}_2(\omega_2)\propto\tilde{E}_1(\omega_2)\times S_{\rm ac}(\Omega). \tag{5.27}$$

In the time domain:

$$E_2\left(t-\frac{n_2 z}{c}\right)\propto E_1\left(t-\frac{n_1 z}{c}\right)\otimes s_{\rm ac}\left(t-\frac{z}{v}\right) \tag{5.28}$$

where n_1 and n_2 are the refractive indices for the optical waves in mode 1 and 2 respectively and v is the speed of the acoustic wave. We see that $E_2(t)$ can then be considered to be the result of the filtering of $E_1(t)$ by a programmable filter with impulse response $s_{\rm ac}(t)$.

5.5.2 Generation of Chirped Pulse Trains

Figure 5.10 shows a schematic diagram of this technique. The experimental setup was very similar to that shown in Figure 5.4. Pulses from a 1 kHz, Ti:Sapphire regenerative amplifier, with output energy 0.5 mJ and pulse duration 50 fs were split with a beamsplitter of reflectivity 25%. The reflected beam was used as the probe while the transmitted pulses

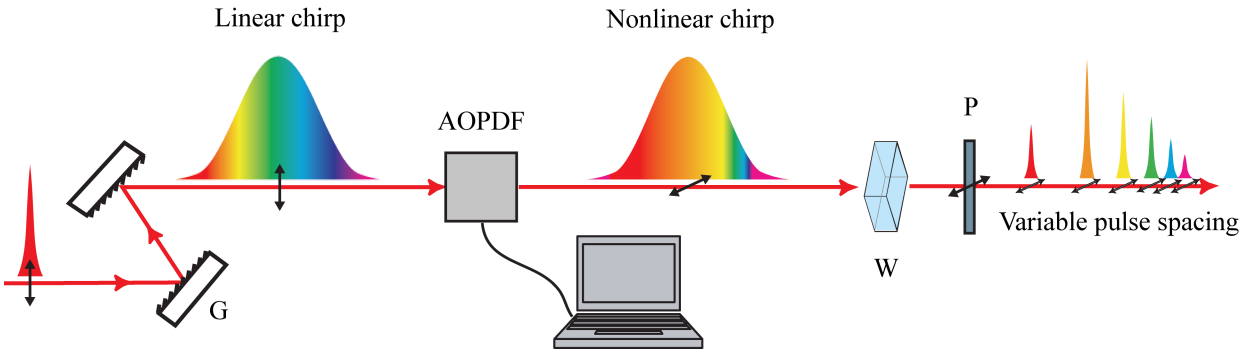

Figure 5.10: Experimental setup used to generate and control trains of ultrashort pulses. G, grating stretcher; W, multiple-order waveplate; P, polariser.

were stretched using a pair of 1200 lines/mm gratings. In contrast with the technique described in Section 5.4, the stretched pulses were then passed through an AOPDF before passing through the waveplate and linear polarizer. The AOPDF used was a FASTLITE Dazzler HR-800, containing a 7 cm-long TeO_2 crystal, allowing a programmable delay of up to 8 ps. The generated pulse trains were measured as before, by overlapping them with the probe pulse reflected by the beamsplitter, in a 1 mm-thick BBO crystal and measuring the SHG light intensity as a function of timing slide position.

Figure 5.11 shows the cross-correlation signals obtained with a 0.8 mm-thick calcite crystal and $\phi^{(3)} = \pm 1 \times 10^6$ fs^3 introduced by the AOPDF. The gratings were separated by 20 mm to give a stretched pulse of duration 1.4 ps. The generated pulse trains comprise approximately seven pulses, each with a duration of approximately 550 fs. It can be seen that the pulse separation within the train varies strongly and that the direction of this variation depends on the sign of $\phi^{(3)}$. Also plotted is $\Delta\tau_{p,p-1}$ as a function of p, showing that $\Delta\tau_{p,p-1}$ varies linearly, as expected and by approximately 160% over the duration of the pulse train.

Figure 5.12 shows cross-correlations of the pulse trains generated using a 1.6 mm-long calcite crystal, as the third order dispersion introduced by the AOPDF is varied. The same grating separation was used, giving a 1.4 ps stretched pulse. Linear fits were performed on

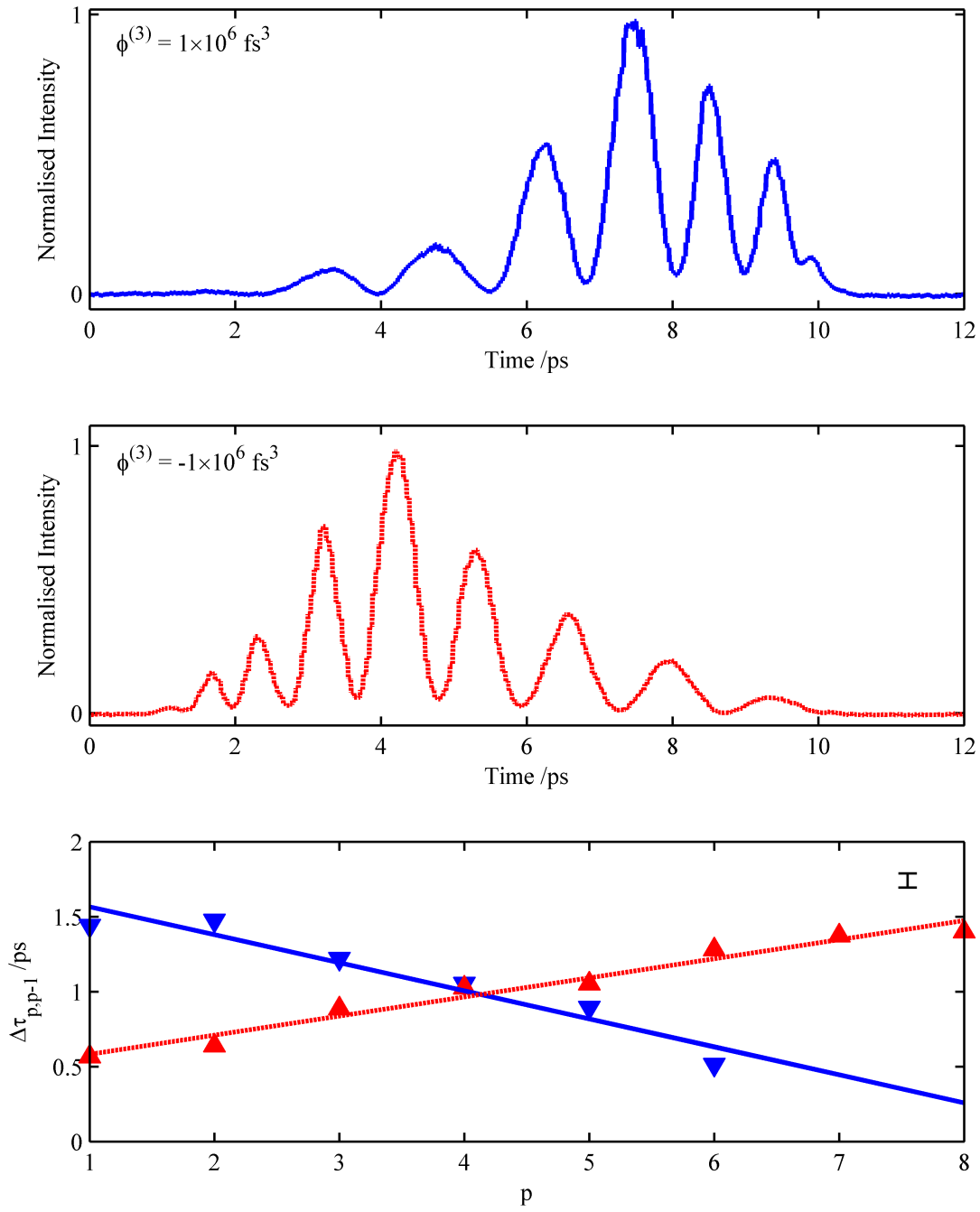

Figure 5.11: Cross-correlation signal recorded for a 1.4 ps stretched pulse, a 0.8 mm crystal and $\phi^{(3)} = \pm 1 \times 10^6\,\mathrm{fs}^3$. The lower plot shows $\Delta\tau_{p,p-1}$ as a function of p for the two sets of data, along with linear fits and a typical error bar.

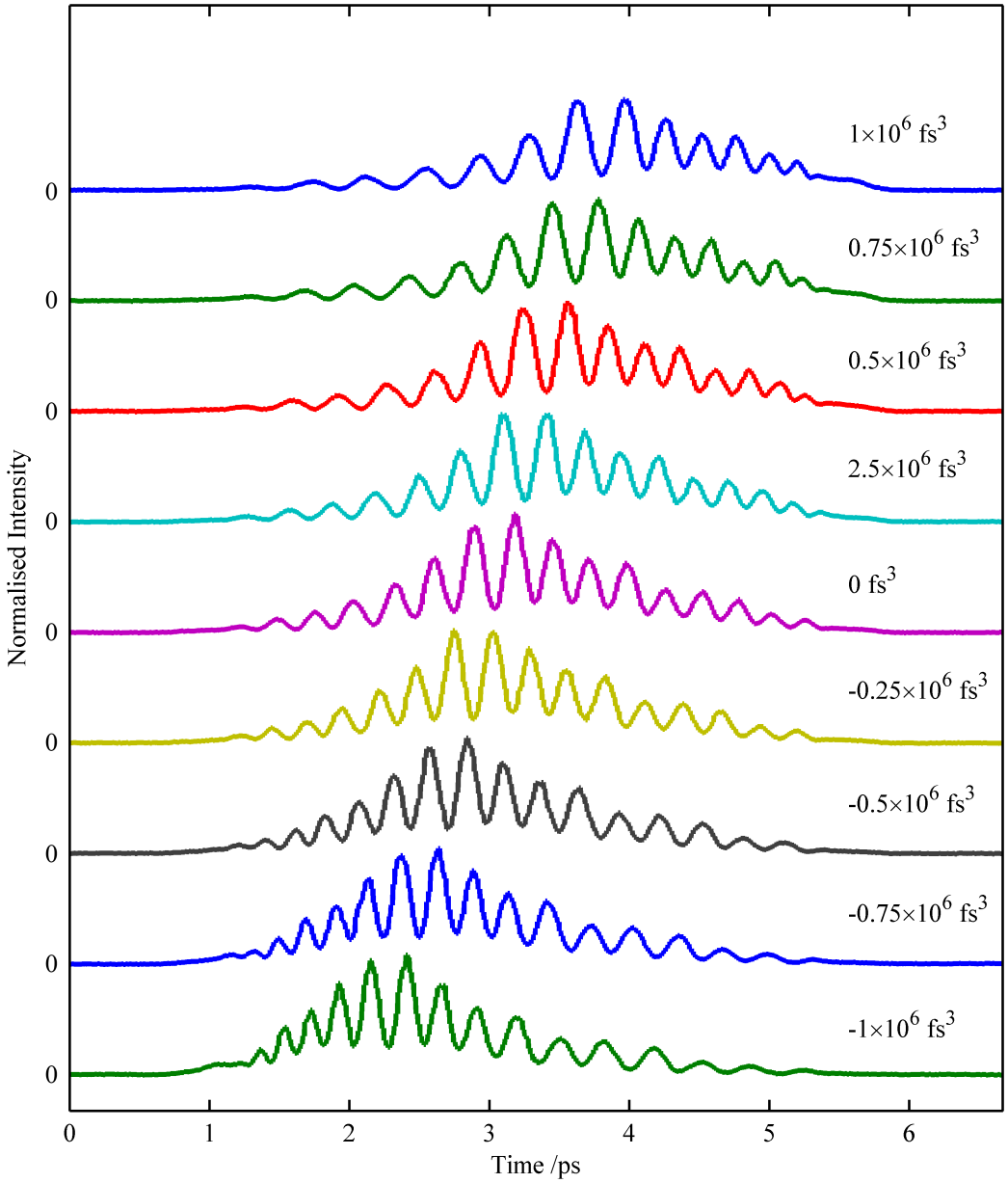

Figure 5.12: Cross-correlation signals recorded for a 1.4 ps stretched pulse, a 1.6 mm crystal and various third-order dispersions applied by the AOPDF.

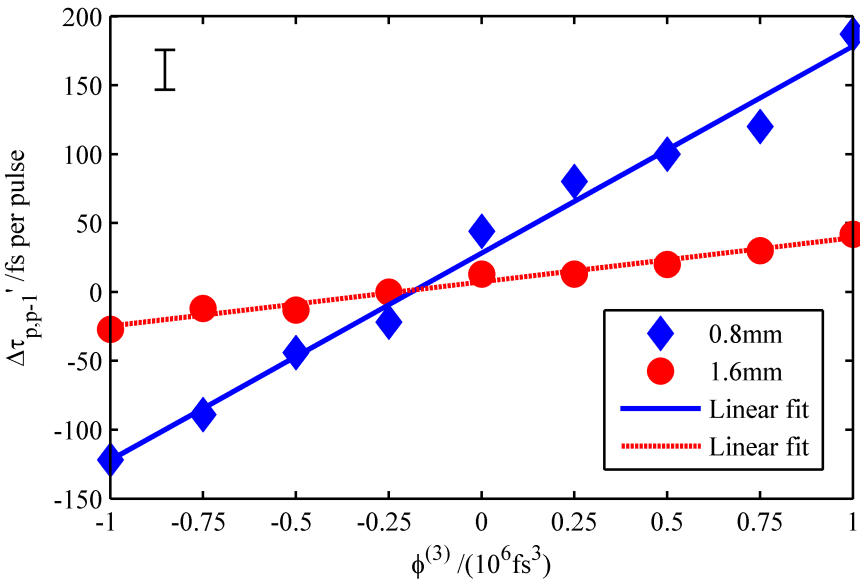

Figure 5.13: The rate of change of pulse separation with pulse number, $\Delta\tau'_{p,p-1}$ is plotted as a function of $\phi^{(3)}$ for a 0.8 mm and 1.6 mm-long calcite crystal. A typical error bar is also shown.

$\Delta\tau_{p,p-1}$ as a function of p, as in Figure 5.11, for each of these plots, yielding $\Delta\tau'_{p,p-1}$, the rate of change of $\Delta\tau$ with p. Figure 5.13 shows the measured $\Delta\tau'_{p,p-1}$ as a function of $\phi^{(3)}$ for crystals of length 0.8 mm and 1.6 mm. Note that there is still a variation in $\Delta\tau$ across the pulse trains, even when the third-order dispersion applied by the AOPDF is zero. This is due to third-order dispersion from other sources, including the grating-pair stretcher and material dispersion.

Higher-order dispersion was also investigated. From Equation (5.23), it is apparent that fourth-order dispersion should lead to a quadratic variation in pulse spacing. Figure 5.14, shows the cross-correlation of a pulse train generated in a 0.8 mm crystal, with a fourth-order dispersion, $\phi^{(4)} = \pm 1 \times 10^8\,\mathrm{fs}^4$ introduced by the AOPDF. It is seen that the pulse spacing matches well to a quadratic fit.

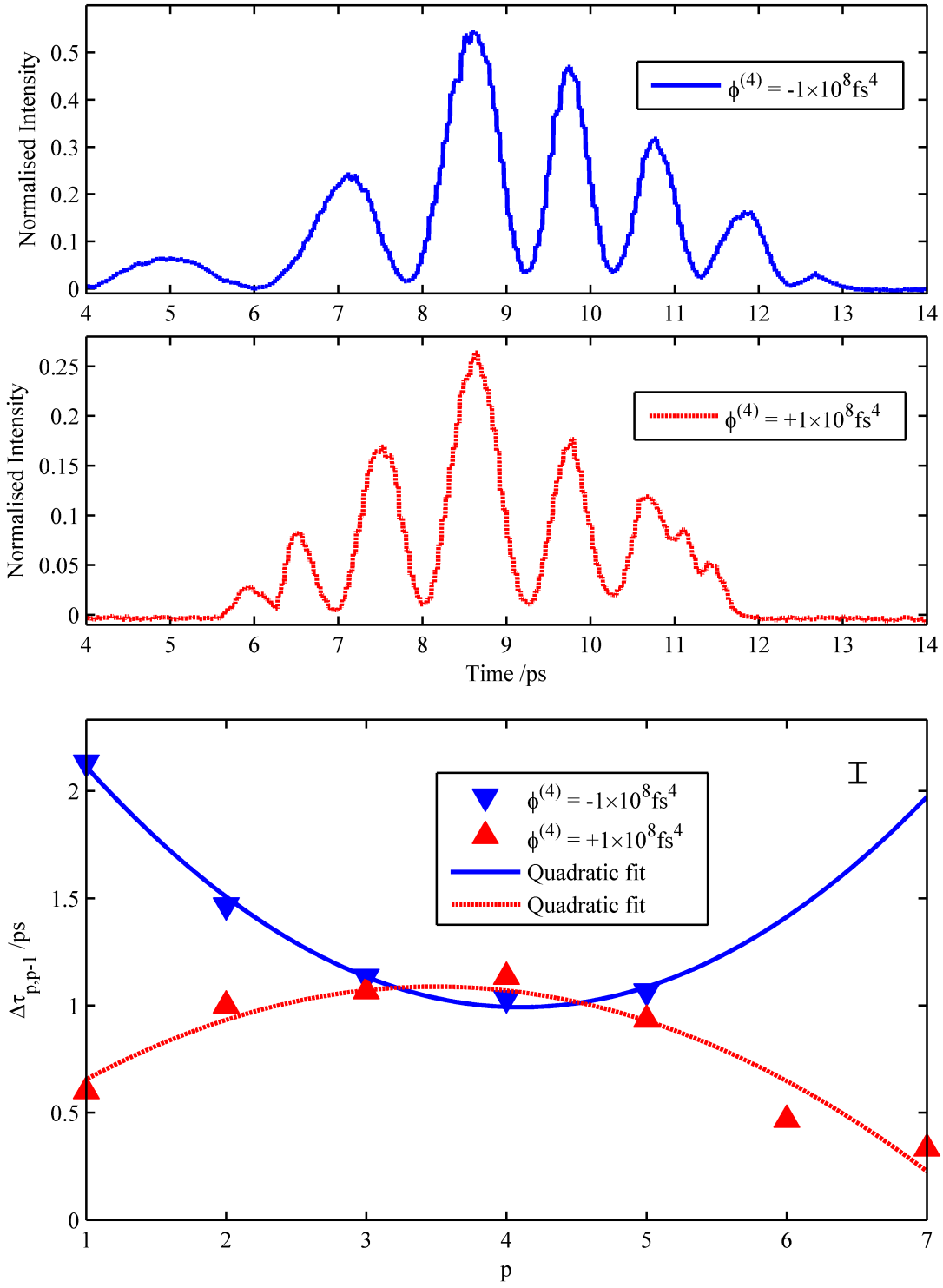

Figure 5.14: Cross-correlation signal recorded for a 1.4 ps stretched pulse, a 0.8 mm crystal and $\phi^{(4)} = \pm 1 \times 10^8\,\mathrm{fs}^4$. The lower plot shows $\Delta\tau_{p,p-1}$ as a function of p for the two sets of data, along with quadratic fits and a typical error bar.

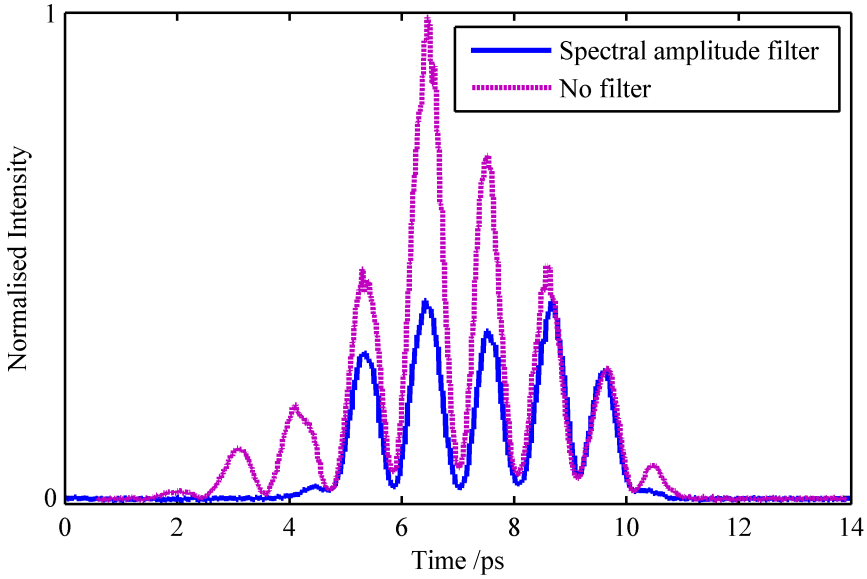

Figure 5.15: Cross-correlation signal recorded for a 1.4 ps stretched pulse generated in a 0.8 mm crystal, with and without a spectral amplitude filter of bandwidth 21 nm applied.

The AOPDF can be used to control the spectral amplitude as well as the spectral phase of the optical pulse. Since the frequency varies with time, this corresponds to shaping the temporal profile of the pulse. This technique can therefore be used to control the amplitude of the pulses in a train, for example it might be desirable for each pulse to have the same intensity, in order to produce a "square" pulse train. Figure 5.15 shows a pulse train generated in a 0.8 mm-long calcite crystal, with and without a spectral amplitude filter of bandwidth 21 nm applied, using the AOPDF. The profile of the amplitude filter was adjusted iteratively to make the pulses in the train as similar in intensity as possible.

Since arbitrary spectral and temporal shaping is possible with an AOPDF, the pulse trains themselves could be generated directly, simply by applying the correct amplitude or phase filter with the AOPDF[84]. However, this presents problems when the pulse trains are required to have a high energy, for the following reasons.

The pulse shaper, whether it be an AOPDF or an alternative device, may be placed either before or after the amplification stage of a laser system. Placing it before the amplifier has the advantage that damage to the shaper is unlikely, due to the low peak-powers involved. Also, in the case of saturated amplifiers, losses incurred during the pulse shaping process do not matter. However, for high power amplifiers, shaped pulses may lead to nonlinearities within the amplifier. Strong modulation of the amplitude or phase of the stretched pulse could lead to nonlinear distortion of the amplified output waveform and possibly damage to the amplifier optics. Therefore it is not possible to generate high-energy pulse trains using pulse-shaping techniques alone. If the pulse shaping is performed before the amplifier, nonlinearities can result in damage, whereas if the pulse shaping is performed after amplification, the energy of the shaped pulse is limited by the device's damage threshold.

The single crystal technique is therefore unique in that it allows the generation of high-power, adaptive pulse trains. It is not necessary to apply strongly modulated spectral amplitude or phase variations in order to produce the pulse train, since this is done by the waveplate/polariser combination after amplification. Therefore the spectral phase control can take place before amplification, with the pulse train generation occurring afterwards, allowing high-energy pulse trains to be generated without the risk of damage to the amplifier.

5.6 Conclusion

Two novel techniques have been described and demonstrated for the generation of ultrashort trains of optical pulses. A robust and reproducible method, involving an array of birefringent crystals, has been shown to generate pulse trains with high contrast and energy. The pulse trains generated with this technique have been used to quasi-phase-match high harmonic

generation, as will be described in the next chapter.

A more flexible technique has also been introduced, which makes use of a multiple-order wave plate and linear polariser combination to modulate the intensity of a chirped pulse, creating a train of pulses. The addition of an AOPDF has been shown to allow the creation of trains with varying interpulse separation, by modifying the spectral phase of the stretched pulse. This allows the generation of high-energy adaptive pulse trains. This technique could be used for QPM where the coherence length varies with position through the generating medium.

Chapter 6

The Counterpropagating Pulse QPM Experiment

We have seen that counter-propagating light can be used to suppress harmonic generation in regions where the driver and counterpropagating pulses overlap. By using a train of optical pulses it is then possible to suppress HHG in the regions which contribute destructively to the harmonic wave, leading to a dramatic increase in harmonic flux. The experiments described in this chapter aimed to use our novel pulsetrain generation techniques, described in Chapter 5, to achieve QPM over multiple coherence lengths.

Experiments similar to those described here were attempted in 2004 and 2006, using the 10 Hz, high-power end of the Terawatt laser in the Clarendon Laboratory. On both attempts, suppression of harmonic generation by counterpropagating light was observed, but little or no enhancement was seen. The experiments described in this chapter began at the end of 2008, using the 1 kHz beam available after the first amplification stage of the Terawatt laser. Switching to a higher-repetition rate laser system made a significant difference when

acquiring HHG spectra, with data acquisition times significantly reduced and much-improved shot-to-shot pulse energy stability.

6.1 The Experiment

The experiment made use of a chirped-pulse amplification Ti:Sapphire laser system, consisting of a mode-locked oscillator seeding a regenerative amplifier, to give linearly-polarised pulses at a repetition rate of 1 kHz, with an energy of 0.5 mJ and FWHM duration of 50 fs. The spectrum of the output pulses was centered at 808 nm.

The experimental arrangement is shown in Figure 6.1. The beam from the regenerative amplifier, with diameter 8.5 mm, passed through a half-wave plate followed by a polarising beamsplitter, to give two beams: the driver, used to generate harmonics, and the counter-propagating beam (CPB), used to suppress them. By rotating the half-wave plate, and hence the plane of polarisation, the splitting of the energy between the two beams could be varied. In the results presented in this chapter, the driver pulse typically had an energy of 0.27 mJ, leaving 0.23 mJ for the counter-propagating pulses.

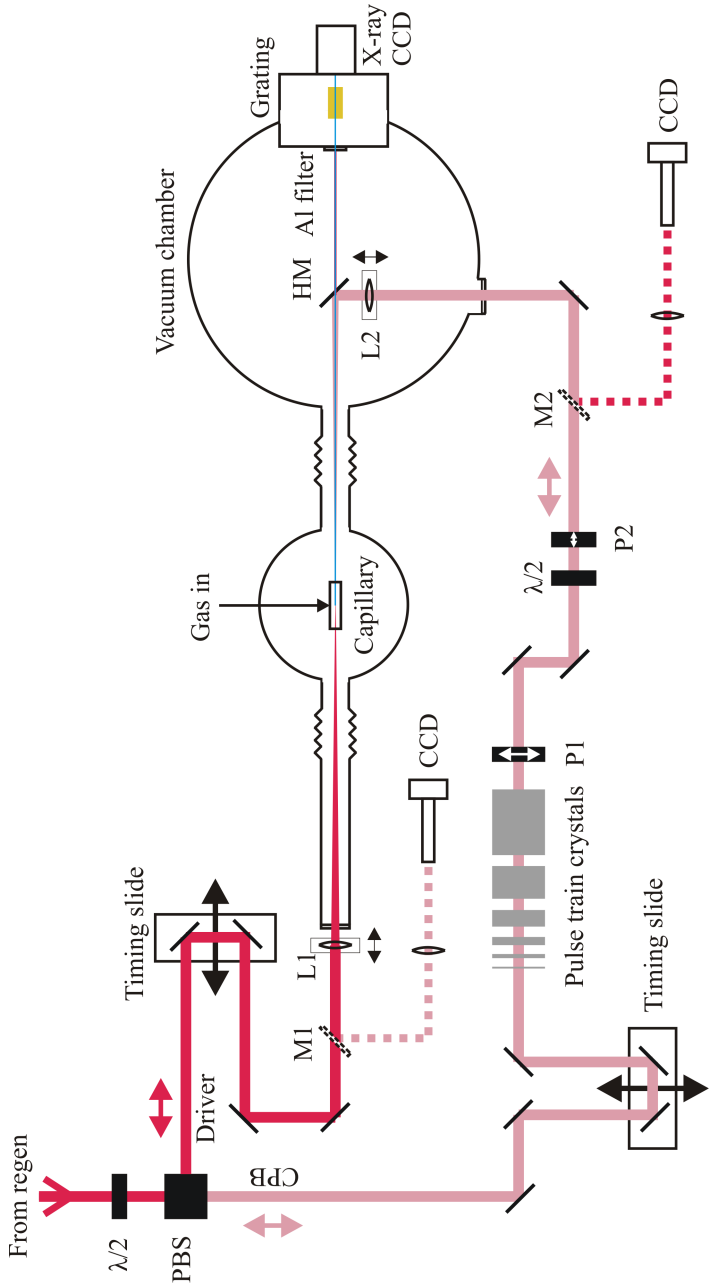

Figure 6.1: Experimental setup. The output of the amplifier was split into the driver beam and CPB, using a polarising beamsplitter (PBS). The driver was focussed by L1 onto the entrance of the capillary, held in vacuum. The CPB passed across a timing slide and then through the crystal/polariser combination to generate a train of pulses. A half-wave plate and polariser combination was then used for energy control and to bring the polarisation parallel to the driver before entering the chamber. The CPB beam was focussed using L2 (identical to L1) onto the capillary exit. L2 was placed directly before HM, a holey mirror. The generated XUV light passed through the hole in HM and into the spectrometer. Aluminium filters were used to reject the fundamental light. M1 and M2 are drop-in mirrors, used to monitor the driver and CPB spots after passing through the capillary.

After passing through the beamsplitting cube, the driver was focussed by lens L1, of focal length 500 mm, into a vacuum chamber and onto the entrance of a capillary containing the generating gas. The counter-propagating beam was passed through a timing slide, consisting of a retro-reflector mounted on a motorized linear-translation stage. This allowed precision control of the path length of the CPB, and therefore the position of overlap in the capillary of the driving and counterpropagating pulses. The CPB then passed through an array of six birefringent crystals, followed by a linear polariser. As described in Section 5.3, this combination of birefringent crystals and polariser can be used to generate trains of pulses. Finally, a half-wave plate and polariser combination was used to rotate the polarisation of the CPB such that it was parallel to that of the driver beam, in order to maximise the suppression effect, as well as for energy control. The CPB then entered the vacuum chamber and was focussed by lens L2 (identical to L1) onto the exit of the capillary. After the lens, the beam was turned 90 degrees by a mirror with a 2 mm-diameter hole through its centre (HM). This hole was drilled at 45 degrees to the plane of the mirror and allowed the harmonic radiation generated in the capillary to pass through the mirror and enter the spectrometer behind it. The lens focussing the CPB beam was located approximately 5 cm prior to the mirror-with-hole, so that the beam diameter at the surface of the hole was approximately 7.5 mm. The hole was found to reduce the energy of the CPB pulses by approximately 30%, but the focal spot, shown in Figure 6.4, retained an approximately Gaussian radial intensity distribution which was well-matched to the radius of the capillary waveguide.

Extreme ultraviolet radiation generated within the capillary passed through the hole in the holey mirror and was dispersed by a flat-field spectrograph consisting of a 1200 lines/mm, gold-coated grating and a cooled Andor CCD (model number DO440-BN). The grating was curved to focus the XUV radiation parallel to the direction of dispersion. The CCD could be moved up and down in the focal plane of the grating in order to image different spectral

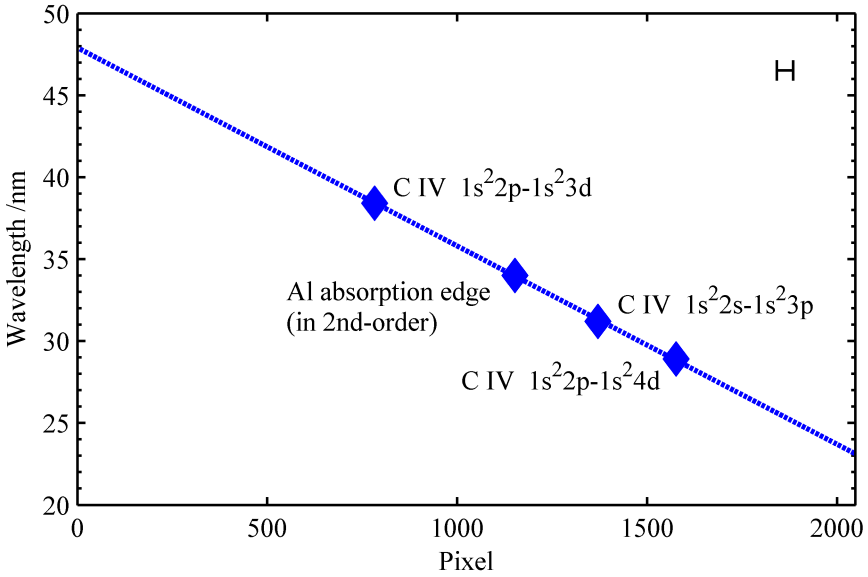

Figure 6.2: Spectrometer calibration, showing the wavelengths of the identified spectral lines as a function of the pixel number, as well as a linear fit and a typical error bar.

regions. Two 0.2 μm-thick Al filters were placed in front of the spectrograph in order to attenuate the 800 nm laser light, while transmitting the XUV light. Without these filters, the CCD was saturated by light from the driving laser.

6.2 Spectrometer Calibration

In order to map CCD pixel number along the chip to wavelength, a calibration was required. One easily obtained data point was the absorption L-edge of the Aluminium filter. A piece of iron was placed at the focus of the CPB, creating a quasi-continuum of XUV light. The 17.1 nm absorption edge was then visible in the recorded spectrum, as well as in second-order at an apparent wavelength of 34.2 nm. Further data points were obtained by observing laser-plasma emission lines with a polyethylene target. Three carbon plasma emission lines were identifiable by their strength and relative spacing[85]. Figure 6.2 shows the resulting

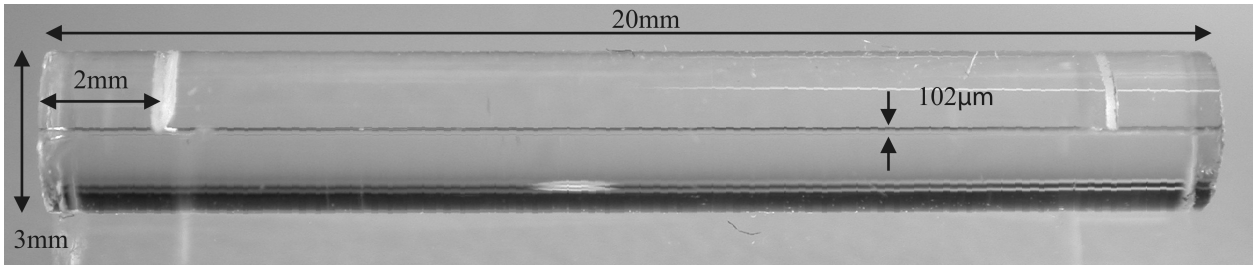

Figure 6.3: A hollow glass capillary, used to contain the gas medium and guide the laser pulses over an extended distance, compared to a free-focus geometry.

calibration, showing a linear fit to be a very good approximation. In the configuration used in the experiments reported in this chapter, the spectrometer could detect radiation in the spectral range 23–48 nm (the 17th–33rd harmonics of an 800 nm driver).

6.3 HHG in Capillaries

The medium used for generating the harmonic radiation was argon gas in the inner bore of a glass capillary waveguide with outer diameter 3 mm. As discussed in Chapter 4, grazing-incidence guiding in these capillaries helps to maintain uniform intensity through the generation region. By maintaining a high intensity over an extended distance, harmonic flux is increased and variation of the coherence length is minimised. Such uniform conditions are ideal for quasi-phase-matching with a non-chirped pulse train. In order to maximise transmission through our capillary, the inner diameter was chosen to maximise coupling into its lowest order mode, as discussed in Section 4.2. The focal spot size, w_0 for both beams was measured to be 35 μm, giving a matched waveguide radius of $a = w_0/0.6435 = 54\,\mu$m. Glass capillaries with inner core radii of 51 μm or 60 μm were available to us, so the former were used.

Figure 6.3 shows the capillary design used in this experiment. The capillary had a length

of 20 mm, with gas slots cut 2 mm from each end. A diamond-wire saw with attached microscope was used to cut the slots[86], allowing precision control of their depths so that they impinged minimally on the inner bore itself. This resulted in gas holes on the inner bore with a diameter of approximately 30 μm. Gas entered the inner bore through these holes and this gas region was isolated from the vacuum using rubber o-rings placed around the capillary between the slots and the ends of the capillary. The gas pressure was expected to be constant between the gas slots, but decrease between the slots and the ends of the capillary, which were at vacuum. For quasi-phase-matching we required a constant coherence length in order to match our pulse-trains of constant inter-pulse spacing. Therefore it was preferable to minimise the length of these end-regions, where there would be considerable variation of the gas pressure and hence coherence length. For this reason they were made to be 2 mm long - just long enough to accommodate the o-rings.

Other groups have used laser machining to cut the gas slots[86], allowing very precise and reproducible holes to be formed. This could be achieved using our laser, however it was found that the ablated glass would solidify in the inner bore of the capillary. This problem might be overcome by filling the inner bore with a gas or liquid, to prevent the glass solidifying on the inner wall.

It was necessary to guide both beams simultaneously through the capillary, a significant challenge, especially with the capillary sitting inside a vacuum chamber. The capillary chamber was attached with flexible bellows to the main chamber, which contained the holey mirror and spectrometer. The capillary chamber was mounted on x-y stages at both its ends, allowing full adjustment of the orientation of the capillary.

The protocol for guiding was to first align both beams as well as possible to a line which passed through the holey mirror and into the spectrometer, defined by a pair of irises, with

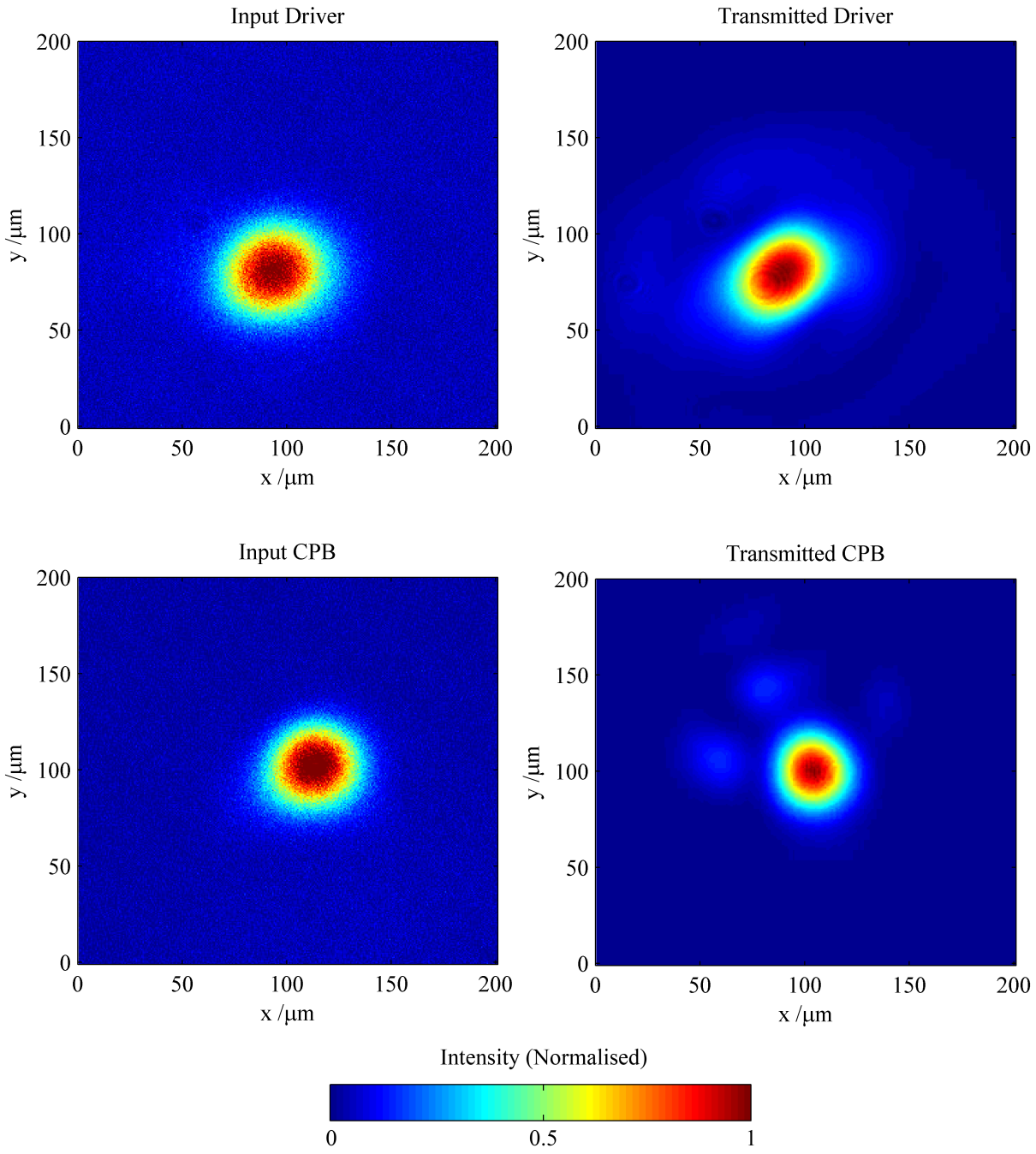

Figure 6.4: Images of the focal spots of the beams before and after transmission through the capillary waveguide, normalized to their own peaks.

the capillary removed. The capillary was then aligned to the driver beam to give the best output spot. Finally the CPB beam was steered into the capillary using the turning mirrors outside of the chamber. Transmissions of 80% for the driving beam were routinely achieved for guiding in vacuum. Guiding was not as good for the CPB beam, with transmissions of around 25% measured. Figure 6.4 shows images of the driver and CPB spots before and after passing through the capillary.

From Equation (4.3) we can calculate the theoretical transmission of our evacuated capillary, given the measured spot size of 35μm. For the driver, this gives a transmission of 83% after propagation over 20 mm, which agrees well with the measured value. For the CPB, taking into account the 30% loss at the holey mirror, the calculation gives a transmission of 58%. This is significantly more than the measured value and can be attributed to imperfect coupling and guiding, due to poor alignment. It is not surprising that the CPB guiding was worse than for the driver beam, since it was more challenging to align the CPB to the capillary using mirrors outside of the chamber, than to align the capillary to the driver beam.

High-harmonic XUV radiation was observed when the driver beam was focused into the argon-filled capillary. The harmonic signal was maximised by observing the harmonics on the CCD in real-time and adjusting the grating separation in the compressor within the amplifier. This effectively compensated for the second-order dispersion encountered by the driver pulses whilst propagating through the optics, maximising their peak intensity on target. Figure 6.5 shows a typical harmonic spectrum obtained from the capillary, for an input pulse energy (measured before the lens) of 0.27 mJ and an argon pressure of 50 mbar. Well-defined harmonic peaks are observed as well as a cut-off at approximately 25 nm. The harmonic intensity also drops off at the long-wavelength end of the spectrum, due to absorption by the argon gas, which increases sharply with wavelength in this region. From the

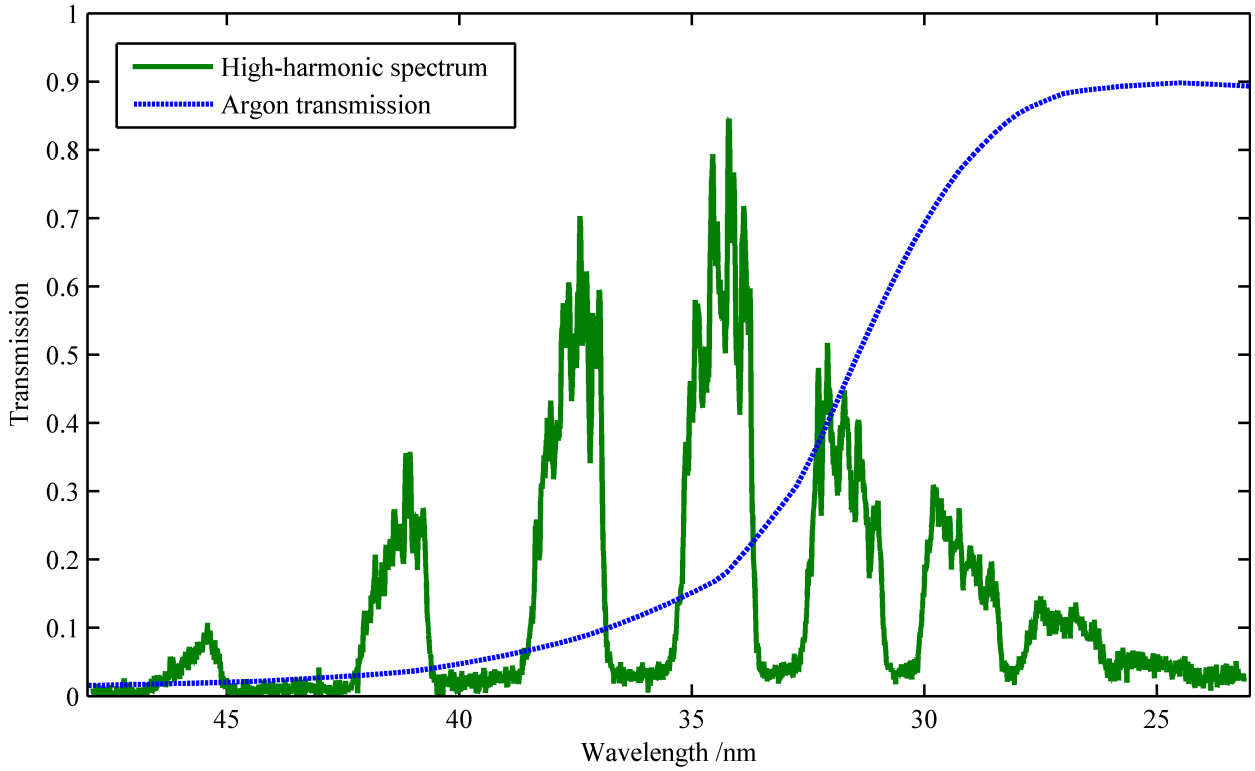

Figure 6.5: A typical harmonic spectrum for a peak intensity $I_{\text{peak}} \approx 2 \times 10^{14}\,\text{Wcm}^{-2}$. Also shown is the spectral transmission of 1 mm argon at a pressure of 50 mbar.

spectrometer calibration these harmonics can be identified as the 17th–31st harmonics of the 800 nm driver.

For a spot-size, $w_0 = 35\,\mu$m and FWHM pulse duration of 50 fs, the pulse energy of 0.27 mJ corresponded to an incident peak intensity of $2.8 \times 10^{14}\,\mathrm{Wcm^{-2}}$ and a transmitted peak intensity of approximately $2 \times 10^{14}\,\mathrm{Wcm^{-2}}$. For this intensity Equation (2.2) predicts an HHG cutoff at a wavelength of 23 nm, in good agreement with the spectrum shown in Figure 6.5.

Note that the grating was not optimally positioned for correct focussing onto the x-ray CCD, and therefore the spectral widths of the harmonics were broadened. This was due to a change in the spectrometer setup following the failure of an x-ray camera. Unfortunately there was insufficient time to perform the necessary changes to mount the grating in the correct position. Nevertheless, it was still possible to resolve the individual harmonic peaks.

6.4 Pulse Trains

The birefringent crystal array method for pulse train generation (described in Section 5.3) was chosen for this experiment. Although the single crystal method is more flexible and compact, it was decided that the array method would be better in terms of repeatability and ease of use. Only pulse trains with constant spacing were required and switching between different pulsetrains using the array method is achieved simply by turning the crystals in their mounts, rather than having to realign a grating stretcher whenever the pulse train was changed. The polarisation of the pulse train beam was set to be parallel to that of the driving beam, in order to maximise the suppression effect. Perpendicular polarisations could have been used, in order to prevent the counterpropagating beam from re-entering the laser system, using an optical isolator. However, as discussed in Section 3.4, a given suppression

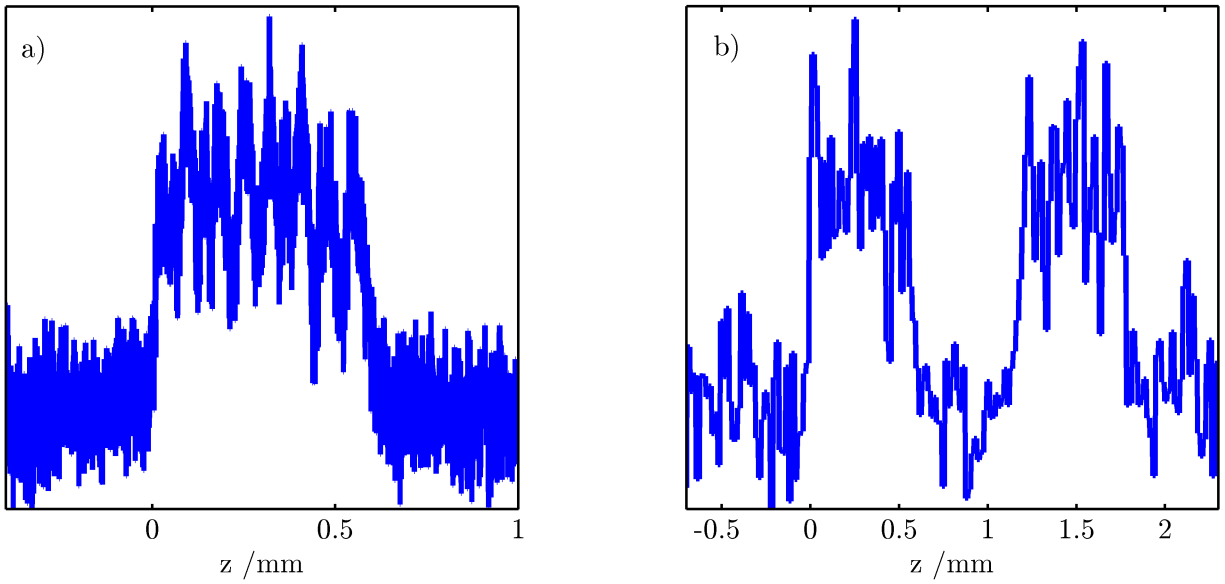

Figure 6.6: Cross correlations of (a) one macropulse consisting of 8 individual pulses and (b) two such macropulses.

requires more counterpropagating energy for the case of perpendicular polarisations than for parallel orientations. Since the laser energy was a major limiting-factor in the experiment, parallel polarisations were therefore used.

After passing through the crystals and other optics, the counterpropagating pulses were broadened to approximately 230 fs FWHM by material dispersion. The thickness and material of the thinnest crystal in the array was such that its birefringence led to a splitting of a 230 fs-duration pulse into two pulses separated by 200 fs. Hence they were overlapping, allowing the generation of long pulses, made up of many overlapping individual pulses. The thinnest crystal used was a 7 mm-thick quartz crystal, followed by calcite crystals of thicknesses 0.8, 1.6, 3.3, 6.6 and 13.2 mm, such that the optical path difference difference for the orthogonal polarisations doubled for each crystal.

The results presented here were obtained using counterpropagating "macropulses" which were made up of eight individual overlapping input pulses, having a total length of 0.6 mm.

Cross-correlations of an individual macropulse and a train of two of these pulses are shown in Figure 6.6.

6.5 Energy Requirement for Suppression

In Section 3.4 the intensity ratios in the driver and CPB beams required to suppress harmonic generation were discussed. In this experiment we were limited to an energy of 0.5 mJ, to be shared between the driver and CPB pulses. This limit on the CPB energy was a major limiting factor on the experiment, especially since the method used to generate pulse trains was inherently only 50% efficient.

We will consider the pulsetrain shown in Figure 6.6(a), which comprised eight overlapping pulses, each having a duration of 230 fs. The macropulse was approximately square and had an overall duration of 2 ps and an energy of 0.12 mJ. Only approximately 25% of this energy was transmitted by the capillary, leaving 0.03 mJ. The driver pulse had a duration of 55 fs on target and an energy of 0.27 mJ, of which around 80% was transmitted by the capillary, leaving 0.22 mJ.

The approximate ratio of the average intensities in the CPB and driver was then:

$$\frac{I_{\mathrm{CPB}}}{I_{\mathrm{driver}}} \approx \frac{0.03}{2000} \times \frac{55}{0.22} = 0.0037 \tag{6.1}$$

Note that these energy estimates are for the driver and CPB pulses after they have traversed the capillary — they will have a greater energy when they first enter the capillary.

From section 3.4 we have the following condition for harmonic suppression:

$$\frac{I_{\mathrm{CPB}}}{I_{\mathrm{driver}}} \approx \left(\frac{\pi}{2q}\right)^2 \tag{6.2}$$

So for the 27th harmonic an intensity ratio $I_{\mathrm{CPB}}/I_{\mathrm{driver}} = 0.003$ is required to suppress harmonic generation with a parallel-polarized counter-propagating pulse. Therefore suppression of the 27th and higher harmonic orders should just be observable with one such macropulse. Adding more pulses would lead to a corresponding reduction of intensity in each macropulse, reducing the suppression effect and therefore any enhancement due to quasi-phase-matching. Adding a second macropulse would halve the energy per macropulse, reducing the intensity to a level well below that estimated to fully suppress generation of the 27th harmonic.

6.6 Oscillation and Enhancement with a Single Pulse

The first step of the experiment was to scan a single counterpropagating pulse through the generation region. In order to implement QPM over multiple coherent zones, knowledge of the local coherence length is required and this can be measured by using one pulse to suppress generation by out-of-phase regions, leading to intensity peaks as emission from adjacent in-phase zones adds constructively. This provides directly a map of the coherence length along the capillary. However, strong oscillation of the harmonic output as a function of timing slide position will only be present if the overlap region between the driver and CPB is approximately equal to the coherence length. If it is too large then HHG will also be suppressed in regions where it contributes constructively to the harmonic field. If the overlap region is too small, then only part of the destructive region will be suppressed. Figure 6.7 shows a typical plot of harmonic spectrum as a function of x, the position of overlap within the capillary of the driving pulse with a single counterpropagating pulse. The counterpropagating pulse has an effective longitudinal extent of 0.3 mm.

Note that there is some ambiguity when discussing the "length" of a counterpropagating pulse. There is a factor of two due to the fact that the change in path difference between the

two beams is twice the change in timing slide timing position. There is also a factor of two due to the fact that the pulses in the beams are counterpropagating with a relative velocity of $2c$. If a pulse is measured by cross-correlation to have a spatial extent of Δz, then if it is counterpropagating with another pulse, they will overlap for an "effective" width of $\Delta z/2$.

The exit of the capillary (the end of the capillary closest to the spectrometer) is at approximately $x = 20\,\text{mm}$ and the gas slot is at $x = 18\,\text{mm}$. These positions were determined by placing a beamsplitter at a position corresponding to the exit of the capillary, with the capillary removed. The driver beam passed through the beamsplitter while the CPB was reflected from it. The pulses from these beams were then cross-correlated by overlapping them in a BBO crystal and measuring the SHG intensity as a function of timing slide position. Since the path length from the beamsplitter was the same for both beams (taking into account the thickness of the beamsplitter), overlap of the pulses in the SHG crystal also corresponded to them overlapping at the beamsplitter.

As expected, oscillations were observed in the intensity of some harmonic orders. The periodicity of these modulations was expected to be twice the coherence length, $2L_c$, which allowed a direct measurement of L_c. Enhancement of the harmonic intensity of 60% was achieved for $q = 27$. We define "enhancement" as the ratio of the harmonic intensity at a given position to that when the timing slide position is far from the region where it produces oscillations, i.e the counterpropagating beam is effectively absent.

The amplitude of the modulations was seen to vary with position through the capillary, due to variations in the coherence length, absorption of the harmonic light by the gas and possibly due to variations in the spatial overlap of the driver and CPB beams. The greatest amplitude of oscillation will occur when the effective counter-propagating pulse length is equal to the coherence length and the signal strength from the two constructively interfering zones is the same. This is generally not the case, due to absorption of the XUV light by

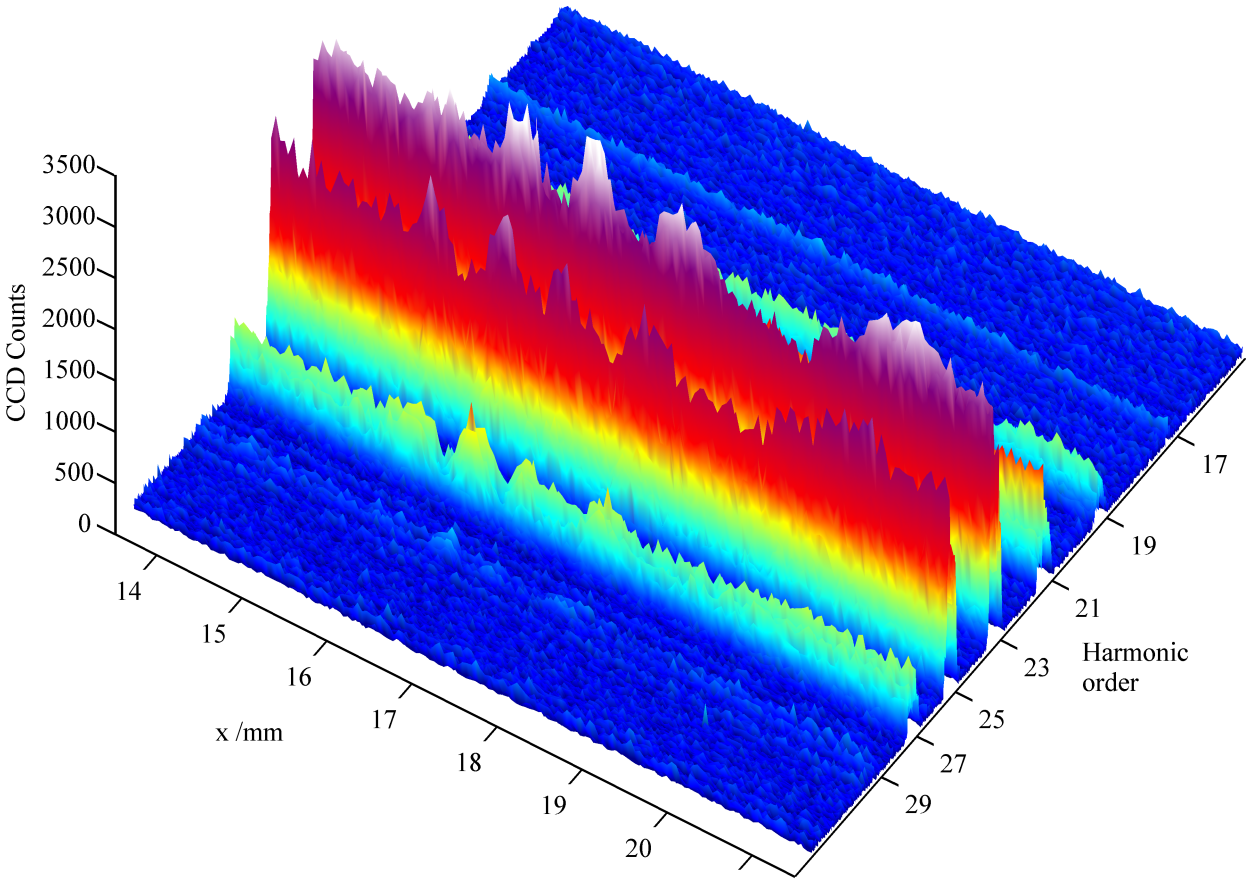

Figure 6.7: Measured HHG spectra (raw data) as a function of the position x of the point of collision between the driver pulse and a 0.3 mm-long counterpropagating pulse, in a capillary containing 50 mbar argon.

the gas medium or variations in the driver intensity, contributing to the observed lack of contrast. The modulation amplitude was also seen to vary with harmonic order, due to the dependence of both the coherence length and the suppression effect on q. The variation of L_c with q is discussed in Section 6.9.

Figure 6.8 shows the enhancement factor as a function of the harmonic order, q, for the scan shown in Figure 6.7. Also plotted as a function of q is the measured coherence length L_c, found by measuring the peak–trough intensity separation at the point of maximum enhancement. It can be seen that the enhancement is greatest for the harmonics for which the coherence length is approximately equal to the effective counterpropagating pulse length of 0.3 mm. This is expected since for this L_c, the counterpropagating pulse leads to the suppression of the entire out of phase-region and no more.

6.7 Oscillation and Enhancement with Two Pulses

Having characterised the generation region with a single macropulse, the next step was to attempt to quasi-phase-match over multiple coherence zones, using a train of counter-propagating pulses. However, as described in Section 6.5, even with a train of only two macropulses, the intensity in each pulse would not be enough to suppress harmonic generation fully. Hence it would be expected that any oscillations and enhancement would be weak. We would still however expect to see greater enhancements for two counter-propagating macropulses over one, if the intensity of each macropulse in both cases is the same. Figure 6.9 shows the intensity of the 27th harmonic as a function of collision point in a capillary containing 80 mbar argon gas for different counterpropagating pulsetrains. For the case of a single counter-propagating macropulse containing all the available energy (0.12 mJ incident

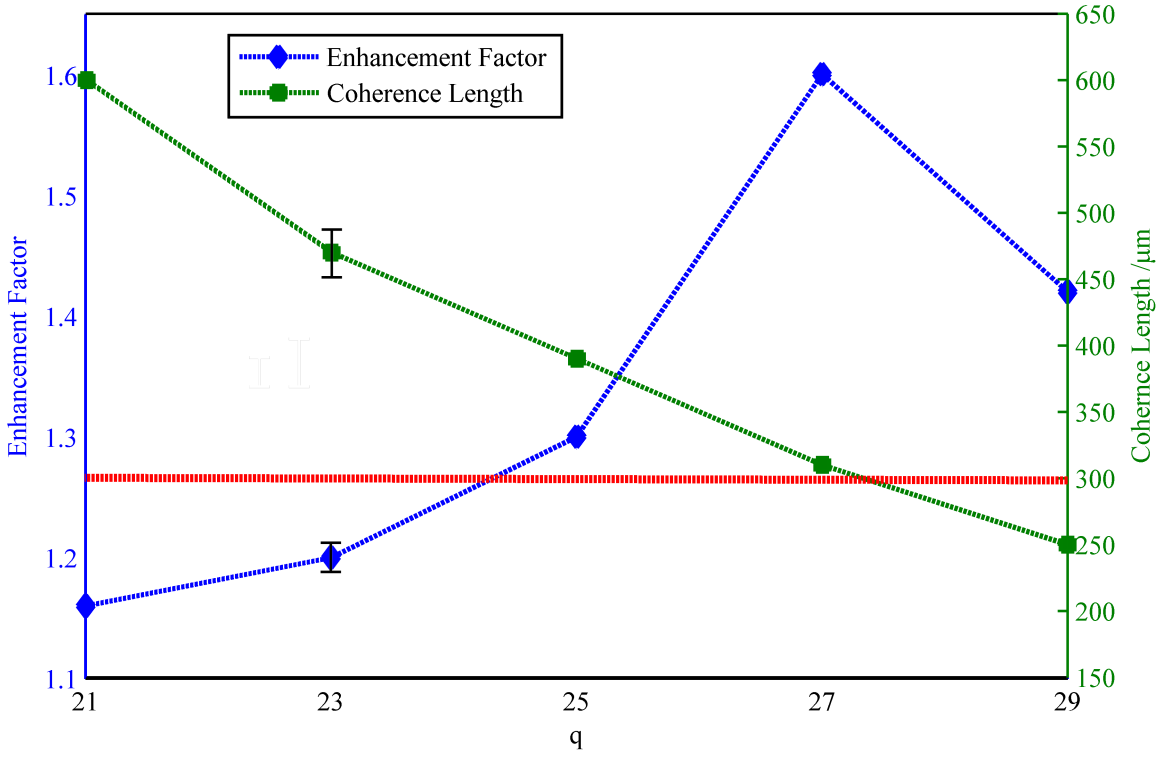

Figure 6.8: Measured enhancement factor and coherence length for the observed harmonics. The red line represents the effective counterpropagating pulse length. As expected, the enhancement is maximised when the coherence length matches this. Indicative error bars are shown.

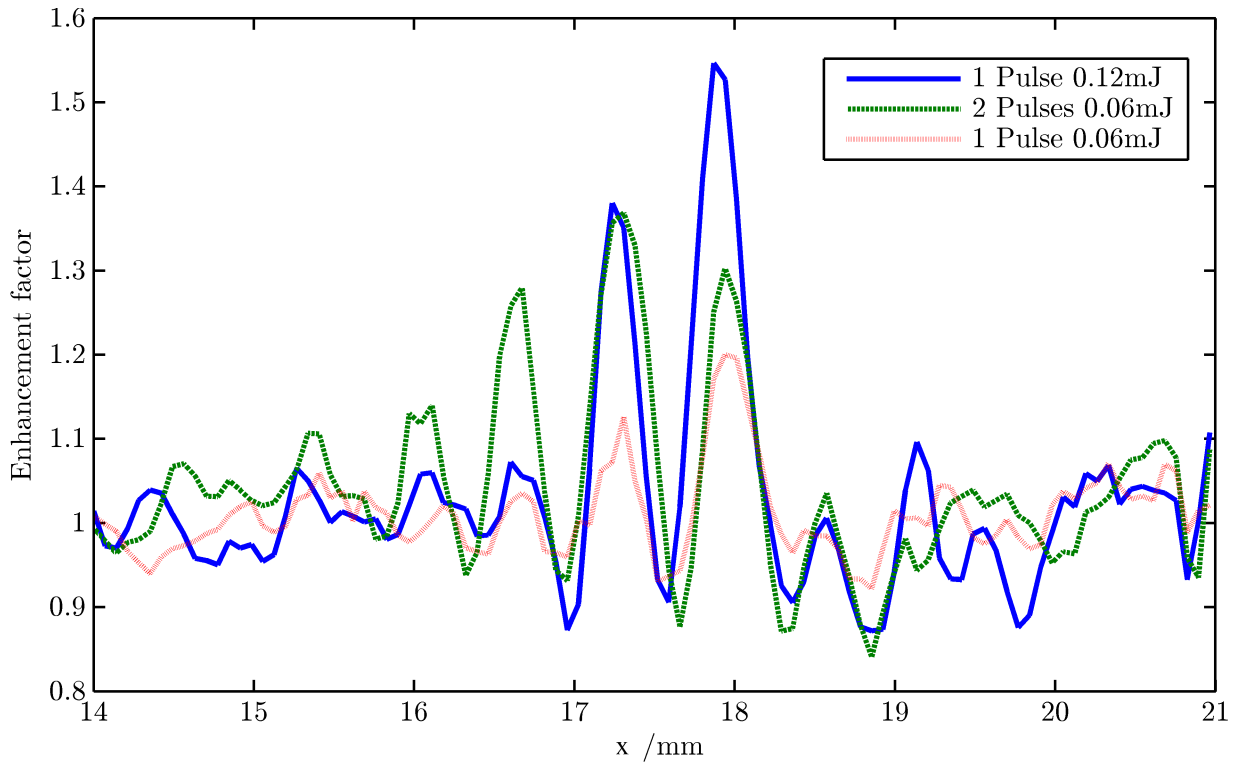

Figure 6.9: Measured intensity of the 27th harmonic as a function of overlap position, x with three pulse trains: (a) one pulse of energy 0.12 mJ, (b) one pulse with energy 0.06 mJ and (c) two pulses, each with energy 0.06 mJ.

on the capillary), strong oscillations in the signal and enhancement of nearly 60% can be seen. If the energy in this single macropulse is reduced by half, the oscillations and enhancement in the 27th harmonic are correspondingly weaker, due to reduced suppression. However, if two such macropulses are used, each with 0.06 mJ on target, much stronger oscillations are seen corresponding to quasi-phase-matching over three coherence lengths. The stronger effect of two counter-propagating macropulses is also evident in the fact that large-amplitude oscillations are seen further into the capillary than for the case of one macropulse.

6.8 Simulation of Experimental Scans

The model of driver and harmonic propagation described in Section 4.4 can be used to simulate these scans, i.e. the measured HHG signal as a function of the point of collision, x of the driving and counterpropgating pulses in the capillary.

The propagation of the driving pulse is governed by Equation 4.14. As before, once the driving field has been determined, the dipole moment, $\langle x \rangle$ can then be calculated, using the Lewenstein model described in Chapter 2. The evolution of the electric field of the generated harmonic radiation through the capillary can then be determined using Equation (4.17):

$$\partial_\xi E_h(\xi,\tau) = -\frac{2\pi}{c}\partial_\tau D[E_l(\xi,\tau)] - \frac{\alpha}{2}E_h(\xi,\tau) \tag{6.3}$$

where the symbols have the same meaning as in Section 4.4.

The experimental scans presented here correspond to the measured harmonic intensity at the end of the generation region ($z = L_g$), as a function of the position, x, of the point at which the driver pulse overlaps with a train of counterpropagating square pulses, $I_{\mathrm{h}}(\xi = L_{\mathrm{g}}, x)$. This experimentally-measured intensity can be modelled by solving Equation (6.3) for $\xi = L_{\mathrm{g}}$, with an additional factor χ multiplying the source term:

$$\partial_\xi E_h(\xi,\tau) = -\frac{2\pi}{c}\partial_\tau[\chi(z,x,w,s)D] - \frac{\alpha}{2}E_h(\xi,\tau) \tag{6.4}$$

Here, $\chi(z,x,w,s)$ is a function which corresponds to modulation of HHG by the counter-

propagating pulse according to:

$$\chi = 1 - s \quad \text{for} \quad x + 2(n-1)w \leq z \leq x + (2n-1)w \tag{6.5}$$

$$= 1 \quad \text{otherwise} \tag{6.6}$$

where $z = x$ corresponds to the front of the first pulse in the train, n is an integer labeling the nth pulse in the train, w is the length of each pulse and s is the degree of modulation of the harmonic field due to the pulses, with $s = 1$ corresponding to total suppression, as shown in Figure 6.10. This corresponds to the ideal case of "square" pulses, although this is a reasonable approximation for the case of the macropulses shown in Figure 6.6.

Figure 6.11 shows a lineout of the measured signal for the 27th harmonic for an argon pressure of 80 mbar, obtained by binning over 100 pixels centered on the peak of the harmonic, corresponding to summing over a spectral region of width 1.2 nm. The inset plot shows the coherence length as a function of position along the capillary, obtained by measuring the peak-to-trough separation in the intensity oscillations. The coherence length is seen to increase markedly around the gas slot, consistent with reductions in both the gas pressure and driver intensity. Further into the capillary, the oscillations are approximately constant, suggesting that the gas pressure and driving laser intensity are both approximately uniform in this region.

Figure 6.12 shows a simulation of the data presented in Figure 6.11, using the model described above. Due to computational limitations, only the last 10 mm of the scan was simulated — the exact propagation length was chosen so that the phase of the intensity modulations matched the experimental data. For these simulations, the initial peak intensity and FWHM duration of the driving laser pulse were set to $2.5 \times 10^{14}\,\mathrm{Wcm^{-2}}$ and 55 fs respectively. The pressure profile of the argon along the capillary was taken to be a constant

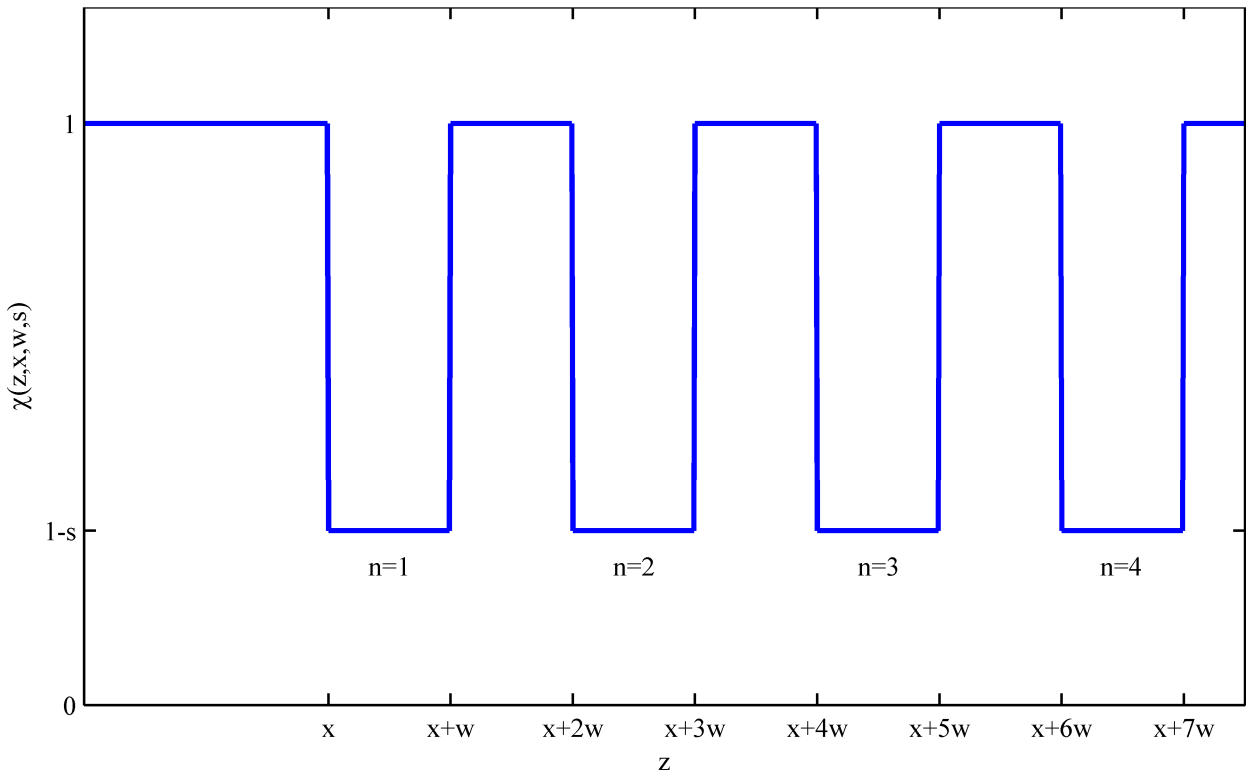

Figure 6.10: The suppression factor, $\chi(z, x, w, s)$ due to a pulse train, where $z = x$ corresponds to the front of the first pulse in the train, n is an integer corresponding to the nth pulse in the train, w is the width of each pulse and s is the degree of suppression due to the pulses.

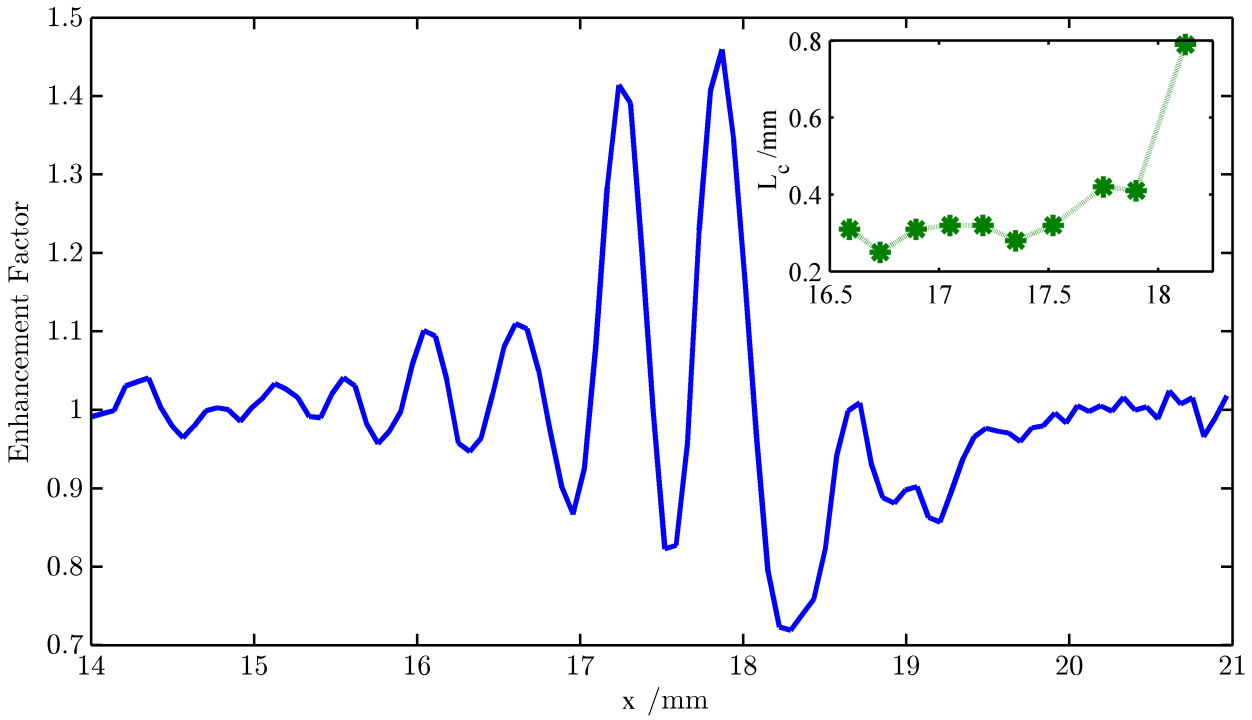

Figure 6.11: Intensity of the 27th harmonic integrated over a spectral width of 1.2 nm (100 pixels) as a function of overlap point, normalised to the value when the counterpropagating pulse collides with the driver pulse far from the region of interest. Inset shows the measured variation of L_c through the capillary.

value of 80 mbar up until the gas slot at 18 mm, followed by a linear decrease to vacuum at the capillary exit at 20 mm. The only parameter not known was the degree of suppression, s induced by the counterpropagating pulse. It can be seen that choosing $s = 0.2$ matches the experimental data well. This implied suppression effect of 20% is low compared with our calculations. This may be due to the fact that the counterpropagating pulse is not perfectly square but consists of a series of discrete, overlapping pulses. Therefore it will be "corrugated" and the necessary suppression intensity may not be maintained over it's full duration. The reduced suppression effect may also have been caused by beating of the intensity of the counterpropagating light, or misalignment of the counterpropagating beam.

The main features of the data are reproduced by the simulation, such as the final deeper and broader dip in the intensity just past the gas slot at $z = 18$ mm, corresponding to suppression of HHG in a region where Δk is smaller, the coherence length is longer and hence the contribution to the observed intensity is relatively high.

This calculation may also be used to determine the enhancement factor which would be achieved if the harmonic suppression was perfect, corresponding to $s = 1$, as shown in Figure 6.12. This would be achieved if the energy in the counterpropagating pulse was great enough to completely suppress HHG. An enhancement factor of 4.5 is predicted in this case, greater than the factor of 4 that one might expect from constructive generation from two coherence lengths. This is because in the absence of a counterpropagating pulse, the observed harmonics are generated in the last coherence length. However, there is less harmonic generation here than further into the capillary, due to depletion of the driver pulse and the lower gas pressure at the end of the capillary. Quasi-phase-matching with a single pulse allows HHG from the next coherence length into the capillary to contribute. In fact the contribution from this zone is greater than that from the last zone, so an increase in intensity of greater than four is observed.

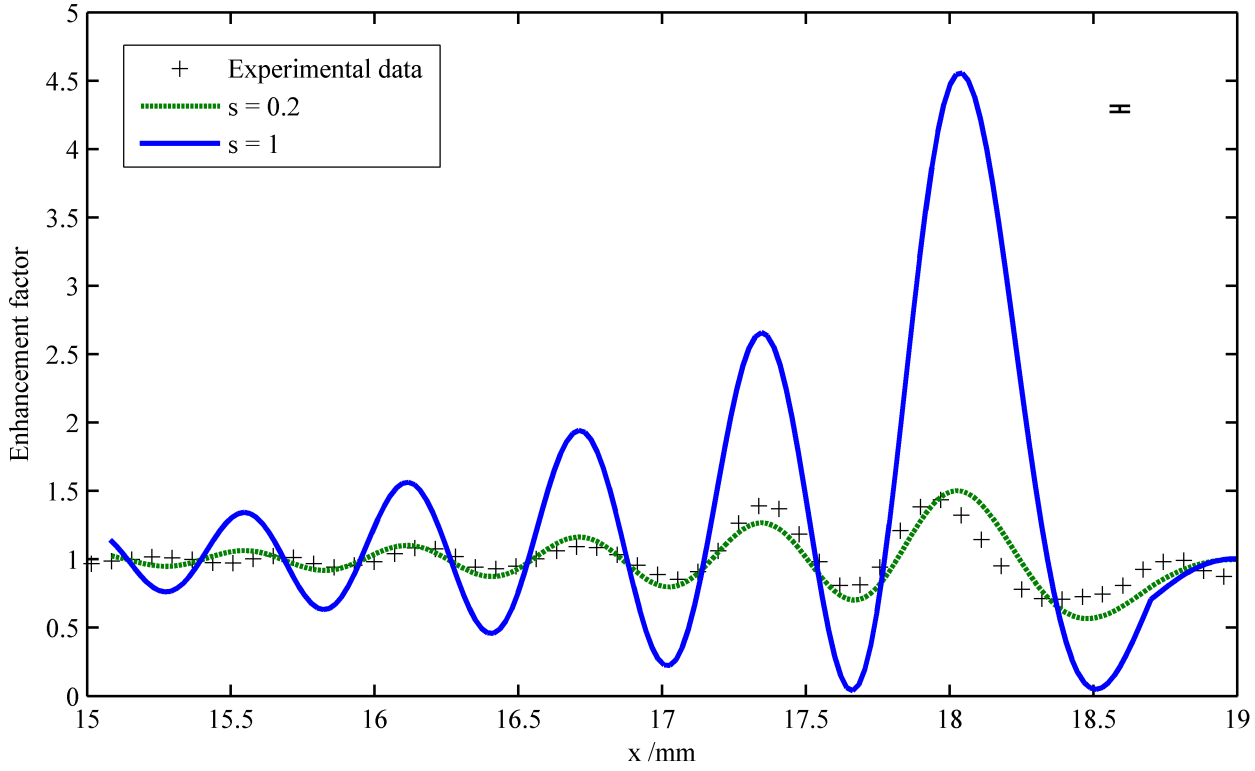

Figure 6.12: Measured intensity of the 27th harmonic as a function of overlap position with a single counter-propagating, 0.3 mm pulse, as well as simulations of these scans for the cases $s = 0.2$ and $s = 1$. The data is plotted for the last few millimeters of the waveguide only, since oscillations were not observed further into the capillary. A typical error bar for the measured data is shown.

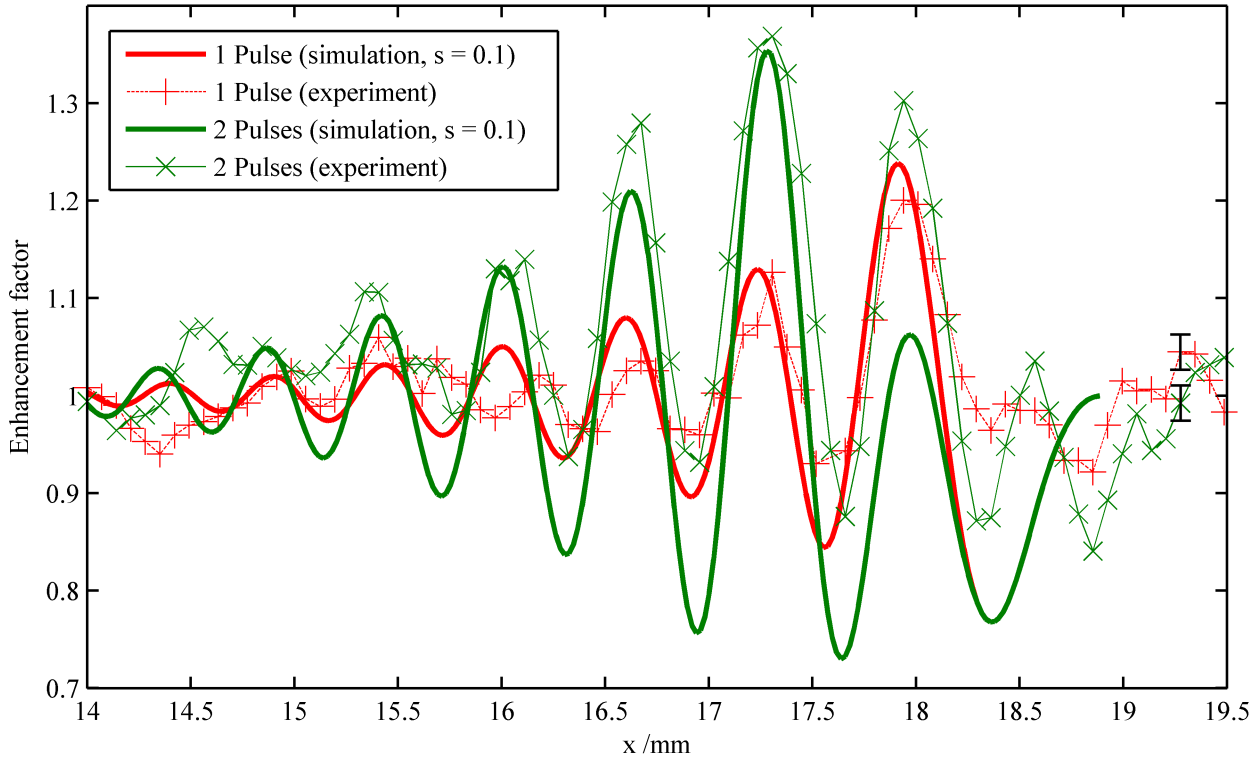

Figure 6.13: Simulation of the intensity of the 27th harmonic as a function of overlap position with one and two pulses: $s = 0.1$ in both cases. The experimental data from Figure 6.9 is also shown, with indicative error bars.

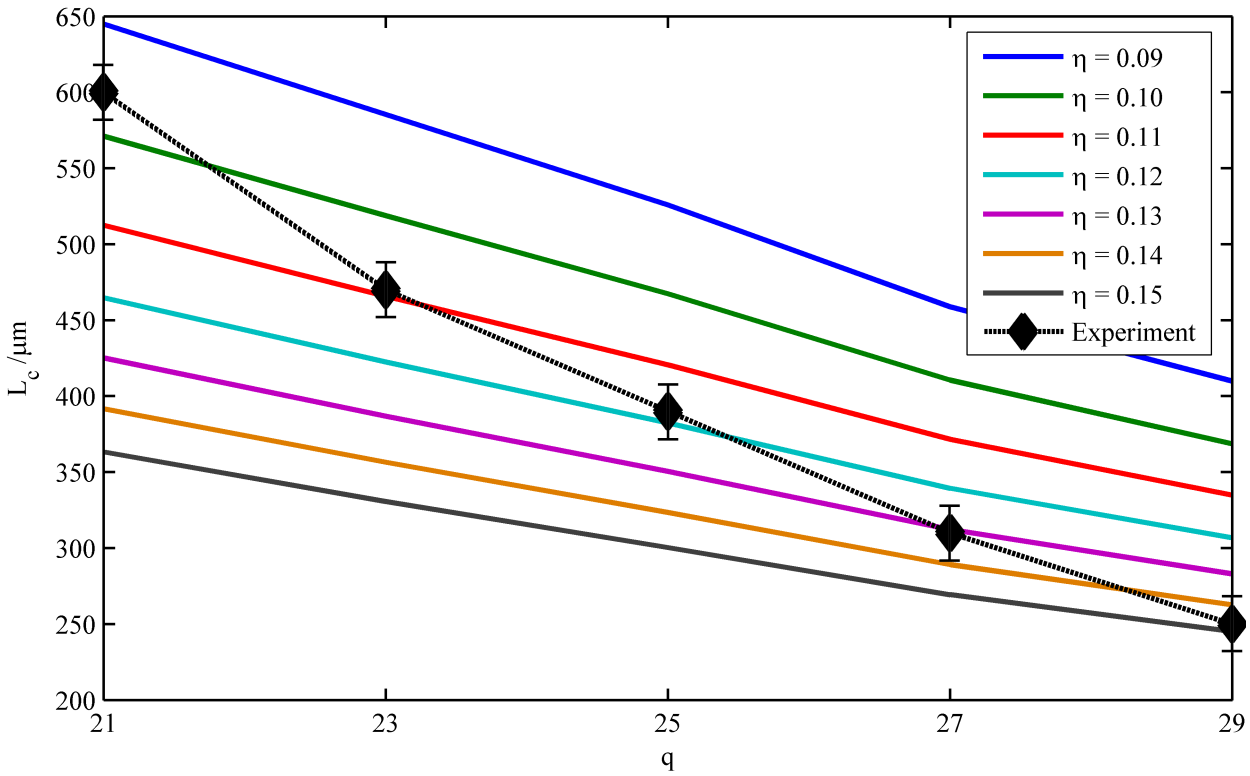

Figure 6.14: Calculated coherence length as a function of harmonic order q, from Equation (3.25). Also plotted are the measured coherence lengths from Figure 6.11.

Figure 6.13 shows a simulation of a scan with both one and two counterpropagating pulses. The measured enhancement factors shown in Figure 6.9 are reproduced if each pulse has a suppression factor of approximately 10%. The other parameters are the same as for Figure 6.12. The main features of Figure 6.9 are reproduced by the simulation; the enhancement factor is greater for the case of two counterpropagating macropulses of the same intensity and strong oscillations are seen further into the capillary for a train of two macropulses than for a single counterpropagating macropulse.

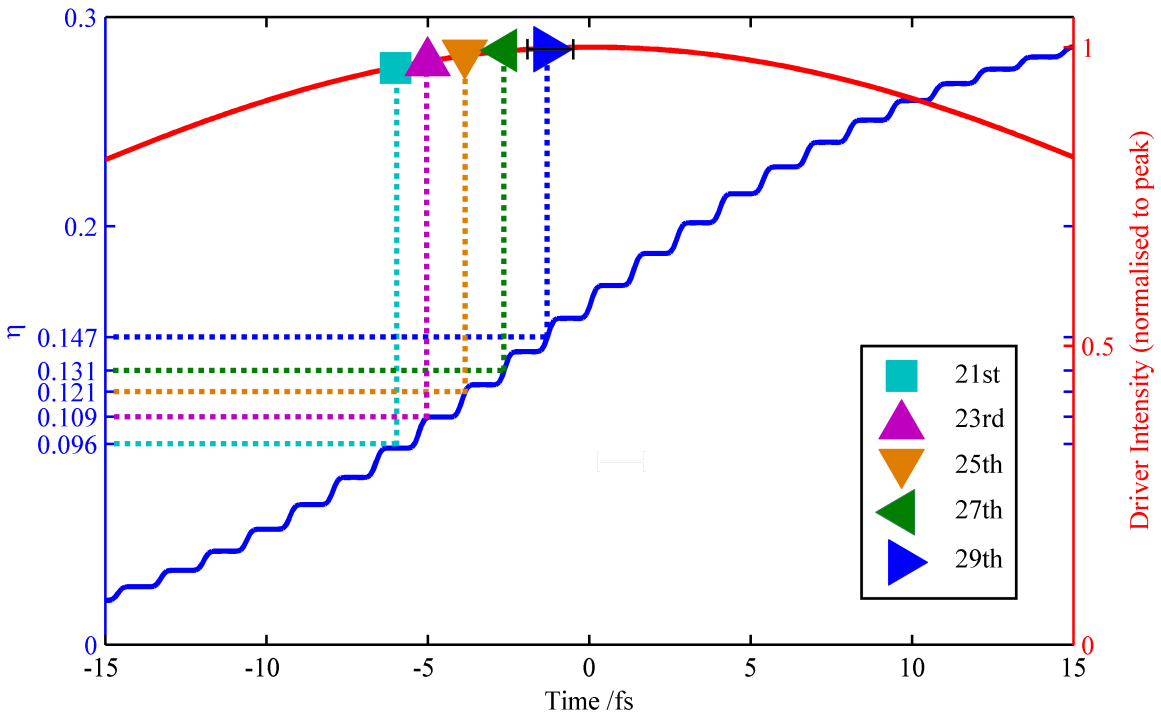

Figure 6.15: Calculated ionization fraction as a function of time during a 55 fs Gaussian driving pulse of peak intensity 2×10^{14} Wcm^{-2} in argon, as calculated from the ADK theory described in Section 2.2.1. The ionization fractions at which the harmonics are generated, obtained from Figure 6.14, are also shown. This allows a determination of when during the driving pulse the different harmonics are produced. An indicative error bar is shown.

6.9 Variation of Coherence Length with Harmonic Order

We can extract information about the dynamics of the HHG process from the variation of coherence length with harmonic order. Equation (3.25) can be used to determine the ionisation fraction which a given L_c corresponds to, for a particular harmonic. The measured coherence length can then be used to determine the ionisation fraction at which the different harmonic orders have been generated at. The ionisation fraction as a function of time can be obtained from ADK simulations and therefore we can then identify when during the driving pulse the different harmonics have been generated.

Figure 6.14 shows the expected analytical dependence of the coherence length on harmonic

order, for a range of constant ionization fractions, as well as the experimentally measured coherence lengths. It can be seen that the coherence lengths of harmonics of increasing q are consistent with increasing ionization fractions. Figure 6.15 shows the ionization fraction as a function of time for a driving pulse of duration 55 fs, calculated using the ADK expression. The ionisation fractions associated with the different harmonics are plotted. This provides a mapping to time within our driving pulse, i.e. it tells us when during the pulse the different harmonics were generated. This analysis suggests that the observed harmonics were generated in a narrow, 5 fs window at the peak of the pulse, with the highest harmonics generated closest to the peak, as expected, since the intensity is greatest here.

In Section 2.2.5, a time-frequency analysis of the single-atom dipole moment showed that a given harmonic was generally produced as long as the intensity was above a threshold value, as shown in Figure 2.7 where a given harmonic is seen to be generated for a range of driving intensities. We might therefore expect there to be a distribution of coherence lengths associated with the generation of a harmonic, corresponding to a range of free electron densities. However, clear oscillations corresponding to a single coherence length are observed experimentally. This apparent discrepancy can be resolved by considering propagation effects. Although a given harmonic is produced for any intensity greater than the threshold value, the greatest contribution occurs when the phase mismatch is minimised, i.e. when the ionisation fraction is lowest and there is just enough intensity to generate the harmonic. This can be seen by performing a wavelet transform on the propagated harmonic field obtained in Section 6.8, 3 mm from the end of the capillary. Figure 6.16 shows the wavelet transform, performed as described in Section 2.2.5. It is seen that most high-order harmonic emission now occurs over just a few optical cycles, and for a correspondingly small range of driving intensities. The driving laser pulse still has a symmetric temporal profile

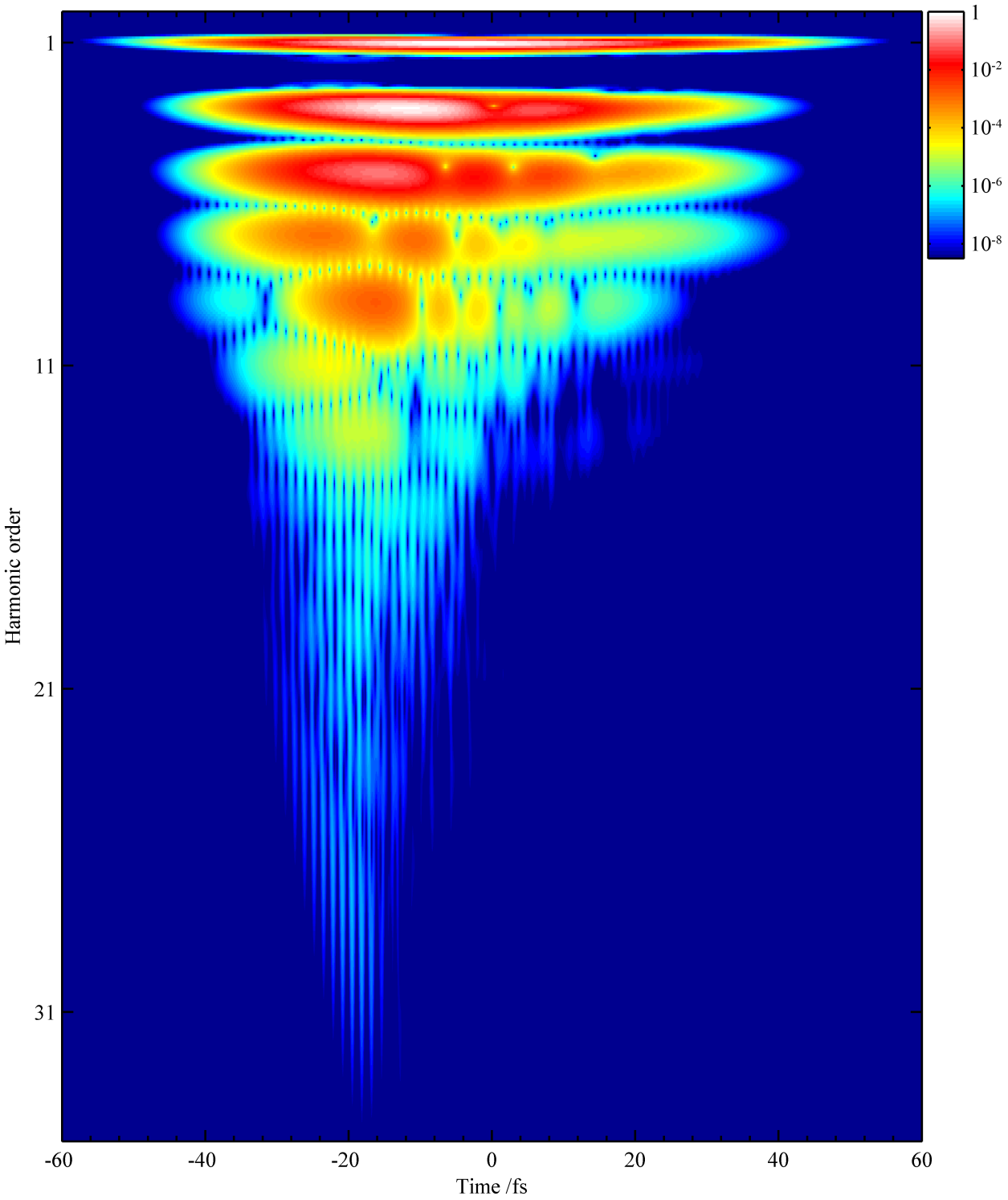

Figure 6.16: A wavelet transform of the propagated harmonic field (modulus squared), illustrating that the greatest contribution to the propagated high-order harmonics comes from the leading edge of the driving pulse, where the phase-mismatch is smallest.

here and the single-atom emission will remain high whilst the intensity is great enough — the asymmetry in this time-frequency representation is due to the increased phase-mismatch as the free electron density increases later on in the pulse.

6.10 Conclusion

Enhancement by up to 60 percent of the intensity of the 27th harmonic has been demonstrated in a gas-filled capillary waveguide, using a single counterpropagating pulse. Quasi-phase-matching using a sequence of two counterpropagating pulses has also been achieved. It was confirmed that the maximum enhancement occurred for the harmonic whose coherence length most closely matched the effective counterpropagating pulse length. Simulations agreed well with the experimental scans and allowed the suppression effect of the counterpropagating pulses to be determined. The measured variation of coherence length with harmonic order also yielded information on the dynamics of the HHG process.

Previous demonstrations of QPM using counterpropagating pulses[58, 59] have reported enhancements of harmonic radiation at a wavelength of 19 nm, of up to a factor of four for one pulse and a factor of fifteen for two pulses. The results presented here do not exhibit enhancements this large. This discrepancy could be attributed to energy limitations, as discussed in Section 6.5. There is also ambiguity in the concept of "enhancement" in this context, as discussed in Section 3.3.

It was therefore not possible to investigate the effect of counterpropagating trains of more than two macropulses. This could in theory be overcome by reducing the coherence length, since the duration and therefore the energy of each counterpropagating macropulse could be reduced, allowing more of them to be generated. This reduction in L_c should be possible by increasing the electron density or moving to higher harmonics. Higher gas pressures

were investigated, in an attempt to increase the electron density, but shorter L_c were not observed, perhaps due to the increased absorption of the harmonics by the gas. Higher-order harmonics could not be accessed due to limitations on the driver pulse energy.

Chapter 7

Conclusion

This thesis has described simulations of the high-harmonic generation process in capillary waveguides, as well as experimental demonstrations of novel pulse train generation techniques and the quasi-phase-matching of HHG using counterpropagating light. The key findings are reviewed here and prospects for developing and extending these techniques are discussed.

7.1 Summary of Work

Simulations of the HHG process in gas-filled capillary waveguides and quasi-phase-matching techniques have been carried out. For the first time, simulations of the effect of mode beating on HHG have been performed which include the effect of finite pulse duration and which use a realistic singe-atom model. It was found that longitudinal variations of the driving laser intensity in a capillary waveguide, due to mode beating, make QPM very difficult to achieve, but simulations suggest that the use of longer waveguides may help by damping-out higher-order modes. The use of mode beating to quasi-phase-match the generation process was also studied. It was found that increases in harmonic intensity, due to mode-beating

QPM, of a factor of two could be achieved over just 1 mm, by making small changes to the focal spot size.

Two novel pulsetrain techniques have been described. The birefringent crystal array technique has been demonstrated to be reproducible and reliable, with cross-correlation measurements confirming that pulse trains with high contrast and energy can be generated. The single-crystal technique, involving a combination of multiple-order waveplate and polariser, has also been shown to form pulse trains from a chirped pulse. This second technique was extended to the generation of adaptive pulse trains by controlling the phase of the input optical pulse using an AOPDF. Linear and quadratic changes in pulse spacing have been measured by applying third and fourth-order dispersion respectively.

The HHG suppression mechanism using counterpropagating light was investigated. Experiments were performed to compare the suppression effect using counterpropagating pulses with linear polarisations parallel and perpendicular to that of the driving light. These showed that suppression was much greater for the parallel case, with approximately an order of magnitude higher counterpropagating intensity required for the same degree of suppression if the polarisations were perpendicular.

Robust suppression of the HHG process with a single counterpropagating pulse in a capillary waveguide was demonstrated and coherent oscillations in the harmonic intensity were measured as the pulse was scanned through the generation region. This provided information on the generating conditions in our waveguide, through the variation in coherence length. Further analysis of these measurements provided a mapping of the generation of the individual harmonic orders to time during the driving pulse.

It was demonstrated that QPM could be achieved by using a single counterpropagating pulse or a train of two pulses, generated using the birefringent crystal array technique. Selective enhancement of the 27th harmonic order of up to 60% was achieved using a single

pulse. Further enhancement could not be achieved, due to limitations on the energy in the counterpropagating beam, leading to less than 100% suppression of HHG in the out-of-phase regions.

Simulations of the experimental scans agreed well with the data and suggested that the suppression effect due to the single counterpropagating pulse was only approximately 20%.

7.2 Future Prospects

7.2.1 QPM Using Counterpropagating Pulse Trains

QMP of HHG using counterpropagating optical pulses has been shown to be a viable technique for increasing the efficiency of HHG and there is great potential to develop and extend this method to shorter wavelengths and higher flux.

A higher-energy laser system would allow more than the two counterpropagating pulses demonstrated here to be used, with a corresponding increase in enhancement. Shorter counterpropagating pulses could also be used to match the shorter coherence lengths associated with higher harmonics towards the cutoff, where the generation process is particularly inefficient. Short coherence lengths are also found when performing HHG in plasma waveguides[87]. These devices allow harmonic generation from a pre-ionized medium and can also guide the driving pulse over extended distances.

Matching to shorter coherence lengths does however present additional technical challenges. The effect of a single counterpropagating pulse (used to probe and characterize the medium) on the output harmonic intensity would be very small and the QPM effect will be very sensitive to the relative timing of the driver and counterpropagating pulses.

It has been shown that the coherence length can change substantially over extended

generation lengths. Therefore if QPM is to be achieved optimally, the pulse trains must be adapted to these generation conditions. I have shown that high-energy adaptive pulse trains can be produced using an acousto-optic programmable dispersive filter in combination with the single-crystal pulse train technique. Genetic algorithms could be used to maximise the harmonic output by making changes to the pulsetrain and observing the change in harmonic intensity, similar to previous work where the temporal and spatial profile of the driving pulse was optimized by adaptive control[88, 89]. These techniques could be used to optimise multiple harmonic orders or even provide new information on the QPM mechanism itself. These adaptive pulse trains could also be used to achieve random phase-matching[90], which in principle could allow enhancement of harmonic flux over a broad bandwidth, resulting in the generation of high peak-power attosecond pulses.

The harmonic cutoff can be extended significantly by making use of few-cycle driving pulses, since very high intensities can be achieved before the medium becomes fully ionized. Spielman et al. have generated harmonics up to 600 eV in this way[91], using an 800 nm driving pulse. However, in order to reach these high intensities, the beam must be focused to a very small spot-size. It has been shown that the harmonic phase is very sensitive to the driving intensity, so the large intensity variation through the focus leads to a strongly varying harmonic phase. This reduces the coherence length below that set by dispersion ($L_c \approx 10\,\mu$m for Spielmann et al.), which is possibly beyond the capabilities of QPM with pulse trains. However, if a waveguide geometry is used, the spatial intensity variation might be reduced, increasing the coherence length to a scale where the high photon energies generated with few-cycle pulses can be produced with much greater efficiency by employing pulse train quasi-phase-matching.

A related QPM technique proposed by Cohen et al.[92], which can be applied to very short coherence lengths down to a few microns, is grating-assisted phase-matching (GAPM).

Rather than using a train of pulses to suppress HHG in out-of-phase zones, a quasi-CW counterpropagating field is used to periodically correct the phase of the harmonics. If the wavelength of the counterpropagating field is tuned to be twice the coherence length in the medium, then its intensity can also be tuned such that the intensity-dependent phase of the harmonics compensates for the phase-slippage. This technique would be particularly applicable to HHG in plasma waveguides where the coherence length is particularly short due to the high free-electron density.

7.2.2 Multi-Mode QPM

An alternative mechanism for QPM of HHG investigated in this thesis is the beating of modes in a capillary waveguide. The experimental demonstration of this technique[54] has stimulated much interest and there is considerable scope to develop this method.

It has been shown that a spatial light modulator can be used to control the transverse phase and amplitude profile of a beam before the focus, in order to selectively excite certain modes of a waveguide[67]. This technique could be used to excite only two modes, resulting in a regular beating of the intensity suitable for QPM. One drawback of this technique is that the propagation constants for a waveguide of a certain diameter are fixed, so the beat period cannot be easily tuned to the coherence length of harmonic generation, although this itself could be varied by changing other parameters, such as the driving intensity or gas pressure.

There is scope for improved modelling of the effect of mode beating on the HHG process and its potential use as a QPM mechanism. The simulations presented in this thesis do not take into account the effect of the ionising gas medium on mode propagation. Courtois et al.[93] have shown that this leads to a nonlinear coupling between the modes, resulting in a periodic energy transfer between them. A better understanding of this effect through

simulation and experiment is necessary to realise the potential of this QPM mechanism.

The progress demonstrated in this thesis represents a step towards the goal of significantly increasing the conversion efficiency of HHG. Advances such as those described here, coupled with developments in high-power laser technology, mean that there is great potential for high-harmonic generation to become a practical source of intense, coherent x-rays and a revolutionary tool in a range of scientific disciplines.

Bibliography

[1] T. H. Maiman. Stimulated optical radiation in ruby. *Nature*, 187(4736):493–494, 1960.

[2] A. E. Siegman. *Lasers*. University Science Books, 1990.

[3] Hiroyuki Daido. Review of soft x-ray laser researches and developments. *Reports on Progress in Physics*, 65(10):1513–1576, 2002.

[4] S. Sebban, T. Mocek, I. Bettaibi, B. Cros, G. Maynard, A. Butler, A. J. Gonzalves, C. M. McKenna, D. J. Spence, S. M. Hooker, L. M. Upcraft, P. Breger, P. Agostini, S. le Pape, P. Zeitoun, C. Valentin, P. Balcou, D. Ros, S. Kazamias, A. Klisnick, G. Jamelot, B. Rus, and J. F. Wyart. Progress on collisionally pumped optical-field-ionization soft x-ray lasers. *Selected Topics in Quantum Electronics, IEEE Journal of*, 10(6):1351–1362, 2005.

[5] S. Suckewer, C. Skinner, H. Milchberg, C. Keane, and D. Voorhees. Amplification of stimulated soft x-ray emission in a confined plasma column. *Physical Review Letters*, 55(17):1753–1756, 1985.

[6] William T. Silfvast, John J. Macklin, and Obert R. Ii. High-gain inner-shell photoionization laser in cd vapor pumped by soft-x-ray radiation from a laser-produced plasma source. *Opt. Lett.*, 8(11):551–553, 1983.

[7] J. J. Rocca, V. Shlyaptsev, F. G. Tomasel, O. D. Cortázar, D. Hartshorn, and J. L. A. Chilla. Demonstration of a discharge pumped table-top soft-x-ray laser. *Physical Review Letters*, 73(16):2192–2195, 1994.

[8] G. J. Tallents. The physics of soft x-ray lasers pumped by electron collisions in laser plasmas. *Journal of Physics D: Applied Physics*, 36(15):R259–R276, 2003.

[9] T. Mocek, B. Rus, M. Stupka, M. Kozlová, A. R. Präg, J. Polan, M. Bittner, R. Sobierajski, and L. Juha. Focusing a multimillijoule soft x-ray laser at 21 nm. *Applied Physics Letters*, 89(5):051501, 2006.

[10] Daniel Zimmer, Bernhard Zielbauer, Vincent Bagnoud, Udo Eisenbarth, Dasa Javorkova, and Thomas Kuehl. An improved double-pulse non-normal incidence pumping geometry for transient collisionally excited soft x-ray lasers. *Opt. Express*, 16(14):10398–10404, 2008.

[11] J. Arthur. Linac coherent light source (lcls) design study report. Technical report, 1999.

[12] J. D. Kmetec, C. L. Gordon, J. J. Macklin, B. E. Lemoff, G. S. Brown, and S. E. Harris. Mev x-ray generation with a femtosecond laser. *Physical Review Letters*, 68(10):1527–1530, 1992.

[13] Gy Farkas and Cs Toth. Proposal for attosecond light pulse generation using laser induced multiple-harmonic conversion processes in rare gases. *Physics Letters A*, 168(5-6):447–450, 1992.

[14] P. M. Paul, E. S. Toma, P. Breger, G. Mullot, F. Auge, Ph Balcou, H. G. Muller, and P. Agostini. Observation of a train of attosecond pulses from high harmonic generation. *Science*, 292(5522):1689–1692, 2001.

[15] M. Hentschel, R. Kienberger, Ch Spielmann, G. A. Reider, N. Milosevic, T. Brabec, P. Corkum, U. Heinzmann, M. Drescher, and F. Krausz. Attosecond metrology. *Nature*, 414(6863):509–513, 2001.

[16] M. Drescher, M. Hentschel, R. Kienberger, M. Uiberacker, V. Yakovlev, A. Scrinzi, Th Westerwalbesloh, U. Kleineberg, U. Heinzmann, and F. Krausz. Time-resolved atomic inner-shell spectroscopy. *Nature*, 419(6909):803–807, 2002.

[17] R. Kienberger, E. Goulielmakis, M. Uiberacker, A. Baltuska, V. Yakovlev, F. Bammer, A. Scrinzi, Th Westerwalbesloh, U. Kleineberg, U. Heinzmann, M. Drescher, and F. Krausz. Atomic transient recorder. *Nature*, 427(6977):817–821, 2004.

[18] R. Kienberger, M. Hentschel, M. Uiberacker, Ch Spielmann, M. Kitzler, A. Scrinzi, M. Wieland, Th Westerwalbesloh, U. Kleineberg, U. Heinzmann, M. Drescher, and F. Krausz. Steering attosecond electron wave packets with light. *Science*, 297(5584):1144–1148, 2002.

[19] Randy A. Bartels, Ariel Paul, Hans Green, Henry C. Kapteyn, Margaret M. Murnane, Sterling Backus, Ivan P. Christov, Yanwei Liu, David Attwood, and Chris Jacobsen. Generation of spatially coherent light at extreme ultraviolet wavelengths. *Science*, 297(5580):376–378, 2002.

[20] M. Wieland, C. Spielmann, U. Kleineberg, T. Westerwalbesloh, U. Heinzmann, and T. Wilhein. Toward time-resolved soft x-ray microscopy using pulsed fs-high-harmonic radiation. *Ultramicroscopy*, 102(2):93–100, 2005.

[21] Richard L. Sandberg, Ariel Paul, Daisy A. Raymondson, Steffen Hädrich, David M. Gaudiosi, Jim Holtsnider, Ra'anan I. Tobey, Oren Cohen, Margaret M. Murnane, Henry C.

Kapteyn, Changyong Song, Jianwei Miao, Yanwei Liu, and Farhad Salmassi. Lensless diffractive imaging using tabletop coherent high-harmonic soft-x-ray beams. *Physical Review Letters*, 99(9), 2007.

[22] Etienne Gagnon, Predrag Ranitovic, Xiao-Min Tong, C. L. Cocke, Margaret M. Murnane, Henry C. Kapteyn, and Arvinder S. Sandhu. Soft x-ray-driven femtosecond molecular dynamics. *Science*, 317(5843):1374–1378, 2007.

[23] Arvinder S. Sandhu, Etienne Gagnon, Robin Santra, Vandana Sharma, Wen Li, Phay Ho, Predrag Ranitovic, Lewis C. Cocke, Margaret M. Murnane, and Henry C. Kapteyn. Observing the creation of electronic feshbach resonances in soft x-ray-induced o2 dissociation. *Science*, 322(5904):1081–1085, 2008.

[24] J. Itatani, J. Levesque, D. Zeidler, Hiromichi Niikura, H. Pepin, J. C. Kieffer, P. B. Corkum, and D. M. Villeneuve. Tomographic imaging of molecular orbitals. *Nature*, 432(7019):867–871, 2004.

[25] Ra'anan I. Tobey, Mark E. Siemens, Oren Cohen, Margaret M. Murnane, Henry C. Kapteyn, and Keith A. Nelson. Ultrafast extreme ultraviolet holography: dynamic monitoring of surface deformation. *Opt. Lett.*, 32(3):286–288, 2007.

[26] A. Mcpherson, G. Gibson, H. Jara, U. Johann, T. S. Luk, I. A. Mcintyre, K. Boyer, and C. K. Rhodes. Studies of multiphoton production of vacuum-ultraviolet radiation in the rare gases. *J. Opt. Soc. Am. B*, 4(4):595, 1987.

[27] P. B. Corkum. Plasma perspective on strong field multiphoton ionization. *Physical Review Letters*, 71(13):1994–1997, 1993.

[28] M. Lewenstein, Ph, Yu, Anne Lchar39huillier, and P. B. Corkum. Theory of high-harmonic generation by low-frequency laser fields. *Physical Review A*, 49(3):2117–2132, 1994.

[29] Jeffrey L. Krause, Kenneth J. Schafer, and Kenneth C. Kulander. High-order harmonic generation from atoms and ions in the high intensity regime. *Physical Review Letters*, 68(24):3535, 1992.

[30] K. S. Budil, P. Salières, M. D. Perry, and Anne L'huillier. Influence of ellipticity on harmonic generation. *Physical Review A*, 48(5):R3437–R3440, 1993.

[31] L. V. Keldysh. Ionization in the field of a strong electromagnetic wave. *Soviet Physics JETP*, 20:1307–1314, 1965.

[32] M. V. Ammosov, N. B. Delone, and V. P. Krainov. Tunnel ionization of complex atoms and of atomic ions in an alternating electromagnetic field. *Soviet Physics - JETP*, 64(6):1191–1194, 1986.

[33] C. Spielmann, C. Kan, N. H. Burnett, T. Brabec, M. Geissler, A. Scrinzi, M. Schnurer, and F. Krausz. Near-kev coherent x-ray generation with sub-10-fs lasers. *Selected Topics in Quantum Electronics, IEEE Journal of*, 4(2):249–265, 1998.

[34] A. D. Bandrauk, S. Chelkowski, D. J. Diestler, J. Manz, and K. J. Yuan. Quantum simulation of high-order harmonic spectra of the hydrogen atom. *Physical Review A (Atomic, Molecular, and Optical Physics)*, 79(2), 2009.

[35] Maciej Lewenstein, Pascal Salières, and Anne L'huillier. Phase of the atomic polarization in high-order harmonic generation. *Physical Review A*, 52(6):4747, 1995.

[36] C. Kan, C. E. Capjack, R. Rankin, and N. H. Burnett. Spectral and temporal structure in high harmonic emission from ionizing atomic gases. *Physical Review A*, 52(6):R4336–R4339, 1995.

[37] E. Priori, G. Cerullo, M. Nisoli, S. Stagira, S. De Silvestri, P. Villoresi, L. Poletto, P. Ceccherini, C. Altucci, R. Bruzzese, and C. de Lisio. Nonadiabatic three-dimensional model of high-order harmonic generation in the few-optical-cycle regime. *Physical Review A*, 61(6):063801, 2000.

[38] M. B. Gaarde, Ph, A. L'huillier, K. J. Schafer, and K. C. Kulander. Macroscopic studies of short-pulse high-order harmonic generation using the time-dependent schrödinger equation. *Physical Review A*, 57(6):4553–4560, 1998.

[39] Philippe Antoine, Bernard Piraux, and Alfred Maquet. Time profile of harmonics generated by a single atom in a strong electromagnetic field. *Physical Review A*, 51(3):R1750–R1753, 1995.

[40] Emily Gibson. *Quasi-Phase Matching of Soft X-ray Light from High-Order Harmonic Generation using Waveguide Structures.* PhD thesis, 1997.

[41] Hyun J. Shin, Dong G. Lee, Yong H. Cha, Jung H. Kim, Kyung H. Hong, and Chang H. Nam. Nonadiabatic blueshift of high-order harmonics from ar and ne atoms in an intense femtosecond laser field. *Physical Review A*, 63(5):053407, 2001.

[42] Ariel R. Libertun, Xiaoshi Zhang, Ariel Paul, Etienne Gagnon, Tenio Popmintchev, Sterling Backus, Margaret M. Murnane, Henry C. Kapteyn, and Ivan P. Christov. Design of fully spatially coherent extreme-ultraviolet light sources. *Applied Physics Letters*, 84(19):3903–3905, 2004.

[43] Charles G. Durfee, Andy R. Rundquist, Sterling Backus, Catherine Herne, Margaret M. Murnane, and Henry C. Kapteyn. Phase matching of high-order harmonics in hollow waveguides. *Physical Review Letters*, 83(11):2187–2190, 1999.

[44] Andy Rundquist, Charles G. Durfee, Zenghu Chang, Catherine Herne, Sterling Backus, Margaret M. Murnane, and Henry C. Kapteyn. Phase-matched generation of coherent soft x-rays. *Science*, 280(5368):1412–1415, 1998.

[45] J. A. Armstrong, N. Bloembergen, J. Ducuing, and P. S. Pershan. Interactions between light waves in a nonlinear dielectric. *Physical Review Online Archive (Prola)*, 127(6):1918–1939, 1962.

[46] P. A. Franken and J. F. Ward. Optical harmonics and nonlinear phenomena. *Reviews of Modern Physics*, 35(1):23–39, 1963.

[47] A. Feisst and P. Koidl. Current induced periodic ferroelectric domain structures in linbo[sub 3] applied for efficient nonlinear optical frequency mixing. *Applied Physics Letters*, 47(11):1125–1127, 1985.

[48] M. H. Chou, K. R. Parameswaran, M. M. Fejer, and I. Brener. Multiple-channel wavelength conversion by use of engineered quasi-phase-matching structures in linbo3 waveguides. *Opt. Lett.*, 24(16):1157–1159, 1999.

[49] P. L. Shkolnikov, A. Lago, and A. E. Kaplan. Optimal quasi-phase-matching for high-order harmonic generation in gases and plasma. *Physical Review A*, 50(6):R4461–R4464, 1994.

[50] J. Seres, V. S. Yakovlev, E. Seres, Ch Streli, P. Wobrauschek, Ch Spielmann, and F. Krausz. Coherent superposition of laser-driven soft-x-ray harmonics from successive sources. *Nature Physics*, 3(12):878–883, 2007.

[51] Ivan Christov, Henry Kapteyn, and Margaret Murnane. Quasi-phase matching of high-harmonics and attosecond pulses in modulated waveguides. *Opt. Express*, 7(11):362–367, 2000.

[52] A. Paul, R. A. Bartels, R. Tobey, H. Green, S. Weiman, I. P. Christov, M. M. Murnane, H. C. Kapteyn, and S. Backus. Quasi-phase-matched generation of coherent extreme-ultraviolet light. *Nature*, 421(6918):51–54, 2003.

[53] Emily A. Gibson, Ariel Paul, Nick Wagner, Ra'anan Tobey, David Gaudiosi, Sterling Backus, Ivan P. Christov, Andy Aquila, Eric M. Gullikson, David T. Attwood, Margaret M. Murnane, and Henry C. Kapteyn. Coherent soft x-ray generation in the water window with quasi-phase matching. *Science*, 302(5642):95–98, 2003.

[54] M. Zepf, B. Dromey, M. Landreman, P. Foster, and S. M. Hooker. Bright quasi-phase-matched soft-x-ray harmonic radiation from argon ions. *Physical Review Letters*, 99(14):143901, 2007.

[55] Justin Peatross, Sergei Voronov, and I. Prokopovich. Selective zoning of high harmonic emission using counter-propagating light. *Opt. Express*, 1(5):114–125, 1997.

[56] Matt Landreman, Kevin O'Keeffe, Tom Robinson, Matt Zepf, Brendan Dromey, and Simon M. Hooker. Comparison of parallel and perpendicular polarized counterpropagating light for suppressing high harmonic generation. *J. Opt. Soc. Am. B*, 24(9):2421–2427, 2007.

[57] S. L. Voronov, I. Kohl, J. B. Madsen, J. Simmons, N. Terry, J. Titensor, Q. Wang, and J. Peatross. Control of laser high-harmonic generation with counterpropagating light. *Physical Review Letters*, 87(13):133902, 2001.

[58] A. L. Lytle, X. Zhang, J. Peatross, M. M. Murnane, H. C. Kapteyn, and O. Cohen. Probe of high-order harmonic generation in a hollow waveguide geometry using counterpropagating light. *Physical Review Letters*, 98(12), 2007.

[59] Xiaoshi Zhang, Amy L. Lytle, Tenio Popmintchev, Xibin Zhou, Henry C. Kapteyn, Margaret M. Murnane, and Oren Cohen. Quasi-phase-matching and quantum-path control of high-harmonic generation using counterpropagating light. *Nat Phys*, 3(4):270–275, 2007.

[60] Amy L. Lytle, Xiaoshi Zhang, Richard L. Sandberg, Oren Cohen, Henry C. Kapteyn, and Margaret M. Murnane. Quasi-phase matching and characterization of high-order harmonic generation in hollow waveguides using counterpropagating light. *Opt. Express*, 16(9):6544–6566, 2008.

[61] Xiaoshi Zhang, Amy L. Lytle, Oren Cohen, Margaret M. Murnane, and Henry C. Kapteyn. Quantum-path control in high-order harmonic generation at high photon energies. *New J. Phys.*, 10(2):025021, 2008.

[62] A. L. Lytle, X. Zhang, P. Arpin, O. Cohen, M. M. Murnane, and H. C. Kapteyn. Quasi-phase matching of high-order harmonic generation at high photon energies using counterpropagating pulses. *Opt. Lett.*, 33(2):174–176, 2008.

[63] E. A. J. Marcatili and R. A. Schmeltzer. Hollow metallic and dielectric waveguides for long distance optical transmission and lasers. *Bell Syst. Tech. J.*, 43:1783–1809, 1964.

[64] B. Cros, C. Courtois, G. Matthieussent, A. Di Bernardo, D. Batani, N. Andreev, and S. Kuznetsov. Eigenmodes for capillary tubes with dielectric walls and ultraintense laser pulse guiding. *Physical Review E*, 65(2):026405, 2002.

[65] M. Geissler, G. Tempea, A. Scrinzi, M. Schnürer, F. Krausz, and T. Brabec. Light propagation in field-ionizing media: Extreme nonlinear optics. *Physical Review Letters*, 83(15):2930–2933, 1999.

[66] M. Geissler, G. Tempea, and T. Brabec. Phase-matched high-order harmonic generation in the nonadiabatic limit. *Physical Review A*, 62(3):033817, 2000.

[67] D. Walter, T. Pfeifer, C. Winterfeldt, R. Kemmer, R. Spitzenpfeil, G. Gerber, and C. Spielmann. Adaptive spatial control of fiber modes and their excitation for high-harmonic generation. *Opt. Express*, 14(8):3433–3442, 2006.

[68] A. M. Weiner, D. E. Leaird, Gary P. Wiederrecht, and Keith A. Nelson. Femtosecond pulse sequences used for optical manipulation of molecular motion. *Science*, 247(4948):1317–1319, 1990.

[69] Yongqian Liu, Sang-Gyu Park, and A. M. Weiner. Enhancement of narrow-band terahertz radiation from photoconducting antennas by optical pulse shaping. *Opt. Lett.*, 21(21):1762–1764, 1996.

[70] A. S. Weling, B. B. Hu, N. M. Froberg, and D. H. Auston. Generation of tunable narrow-band thz radiation from large aperture photoconducting antennas. *Applied Physics Letters*, 64(2):137–139, 1994.

[71] A. Markelz. Pulsed terahertz spectroscopy of dna, bovine serum albumin and collagen between 0.1 and 2.0 thz. *Chemical Physics Letters*, 320(1-2):42–48, 2000.

[72] D. D. Arnone, C. M. Ciesla, A. Corchia, S. Egusa, M. Pepper, J. M. Chamberlain, C. Bezant, E. H. Linfield, R. Clothier, and N. Khammo. Applications of terahertz (thz) technology to medical imaging. In J. M. Chamberlain, editor, *Society of Photo-Optical Instrumentation Engineers (SPIE) Conference Series*, volume 3828 of *Presented at the Society of Photo-Optical Instrumentation Engineers (SPIE) Conference*, pages 209–219, 1999.

[73] S. A. Crooker. Fiber-coupled antennas for ultrafast coherent terahertz spectroscopy in low temperatures and high magnetic fields. *Review of Scientific Instruments*, 73(9):3258–3264, 2002.

[74] Craig W. Siders, Jennifer L. Siders, Antoinette J. Taylor, Sang-Gyu Park, and Andrew M. Weiner. Efficient high-energy pulse-train generation using a 2 n-pulse michelson interferometer. *Appl. Opt.*, 37(22):5302–5305, 1998.

[75] A. M. Weiner, J. P. Heritage, and E. M. Kirschner. High-resolution femtosecond pulse shaping. *J. Opt. Soc. Am. B*, 5(8):1563–1572, 1988.

[76] B. Dromey, M. Zepf, M. Landreman, K. O'Keeffe, T. Robinson, and S. M. Hooker. Generation of a train of ultrashort pulses from a compact birefringent crystal array. *Appl. Opt.*, 46(22):5142–5146, 2007.

[77] Ryuzi Yano and Hideki Gotoh. Tunable terahertz electromagnetic wave generation using birefringent crystal and grating pair. *Japanese Journal of Applied Physics*, 44(12):8470–8473, 2005.

[78] K. O'Keefe, T. Robinson, and S. M. Hooker. Generation and control of chirped, ultrafast pulsetrains. *Journal of Optics A: Pure and Applied Optics*, 12(015201):1, 2009.

[79] A. M. Weiner, D. E. Leaird, J. S. Patel, and Wullert. Programmable shaping of femtosecond optical pulses by use of 128-element liquid crystal phase modulator. *Quantum Electronics, IEEE Journal of*, 28(4):908–920, 1992.

[80] C. W. Hillegas, J. X. Tull, D. Goswami, D. Strickland, and W. S. Warren. Femtosecond laser pulse shaping by use of microsecond radio-frequency pulses. *Opt. Lett.*, 19(10):737–739, 1994.

[81] D. Yelin, D. Meshulach, and Y. Silberberg. Adaptive femtosecond pulse compression. *Opt. Lett.*, 22(23):1793–1795, 1997.

[82] P. Tournois. Acousto-optic programmable dispersive filter for adaptive compensation of group delay time dispersion in laser systems. *Optics Communications*, 140(4-6):245–249, 1997.

[83] F. Verluise, V. Laude, Z. Cheng, Ch Spielmann, and P. Tournois. Amplitude and phase control of ultrashort pulses by use of an acousto-optic programmable dispersive filter: pulse compression and shaping. *Opt. Lett.*, 25(8):575–577, 2000.

[84] A. M. Weiner, D. E. Leaird, J. S. Patel, and J. R. Wullert. Programmable femtosecond pulse shaping by use of a multielement liquid-crystal phase modulator. *Opt. Lett.*, 15(6):326–328, 1990.

[85] Yu Ralchenko, A. E. Kramida, J. Reader, and Nist A. S. D. Team. Nist atomic spectra database (version 3.1.5), 2008.

[86] Ariel J. Paul. *Coherent EUV Light from High-Order Harmonic Generation: Enhancement and Applications to Lensless Diffractive Imaging.* PhD thesis, 2007.

[87] David M. Gaudiosi, Brendan Reagan, Tenio Popmintchev, Michael Grisham, Mark Berrill, Oren Cohen, Barry C. Walker, Margaret M. Murnane, Henry C. Kapteyn, and Jorge J. Rocca. High-order harmonic generation from ions in a capillary discharge. *Physical Review Letters*, 96(20):203001, 2006.

[88] R. Bartels, S. Backus, E. Zeek, L. Misoguti, G. Vdovin, I. P. Christov, M. M. Murnane, and H. C. Kapteyn. Shaped-pulse optimization of coherent emission of high-harmonic soft x-rays. *Nature*, 406(6792):164–166, 2000.

[89] D. Yoshitomi, J. Nees, N. Miyamoto, T. Sekikawa, T. Kanai, G. Mourou, and S. Watanabe. Phase-matched enhancements of high-harmonic soft x-rays by adaptive wave-front control with a genetic algorithm. *Applied Physics B: Lasers and Optics*, 78(3):275–280, 2004.

[90] Alon Bahabad, Oren Cohen, Margaret M. Murnane, and Henry C. Kapteyn. Quasi-periodic and random quasi-phase matching of high harmonic generation. *Opt. Lett.*, 33(17):1936–1938, 2008.

[91] Ch Spielmann, N. H. Burnett, S. Sartania, R. Koppitsch, M. Schnurer, C. Kan, M. Lenzner, P. Wobrauschek, and F. Krausz. Generation of coherent x-rays in the water window using 5-femtosecond laser pulses. *Science*, 278(5338):661–664, 1997.

[92] O. Cohen, A. L. Lytle, X. Zhang, M. M. Murnane, and H. C. Kapteyn. Optimizing quasi-phase matching of high harmonic generation using counterpropagating pulse trains. *Optics letters*, 32(20):2975–2977, 2007.

[93] C. Courtois, A. Couairon, B. Cros, J. R. Marquès, and G. Matthieussent. Propagation of intense ultrashort laser pulses in a plasma filled capillary tube: Simulations and experiments. *Physics of Plasmas*, 8(7):3445–3456, 2001.